

UNIVERSIDADE FEDERAL DO ESPÍRITO SANTO
CENTRO TECNOLÓGICO
PROGRAMA DE PÓS-GRADUAÇÃO EM ENGENHARIA AMBIENTAL

VITOR FERREIRA LAVOR

**LARGE-EDDY SIMULATION OF POLLUTANT DISPERSION FROM
AN AREA SOURCE OVER RANDOM HEIGHT BUILDINGS ARRAYS**

VITÓRIA

2019

VITOR FERREIRA LAVOR

**LARGE-EDDY SIMULATION OF POLLUTANT DISPERSION FROM
AN AREA SOURCE OVER RANDOM HEIGHT BUILDINGS ARRAYS**

A dissertation submitted in partial fulfilment of the requirements for the degree of Master of Science in Environmental Engineering.

Area: Air Pollution

Supervisor: Prof. Neyval Costa Reis Jr., Ph.D.

Co-supervisors: Prof. Elisa Valentim Goulart, Ph.D.
and Prof. Zheng-Tong Xie, Ph.D.

VITÓRIA

2019

Ficha catalográfica disponibilizada pelo Sistema Integrado de Bibliotecas - SIBI/UFES e elaborada pelo autor

L4141 Labor, Vitor Ferreira, 1990-
Large-eddy simulation of pollutant dispersion from an area source over random height buildings arrays / Vitor Ferreira Labor. - 2019.
107 f. : il.

Orientador: Neyval Costa Reis Junior.
Coorientadores: Elisa Valentim Goulart, Zheng-Tong Xie.
Dissertação (Mestrado em Engenharia Ambiental) -
Universidade Federal do Espírito Santo, Centro Tecnológico.

1. Áreas urbanas. 2. Ar - Poluição. 3. Simulação das grandes escalas (LES). 4. Edifícios altos. 5. Massa - Transferência. 6. Fluxo de escalar. I. Reis Junior, Neyval Costa. II. Goulart, Elisa Valentim. III. Xie, Zheng-Tong. IV. Universidade Federal do Espírito Santo. Centro Tecnológico. V. Título.

CDU: 628

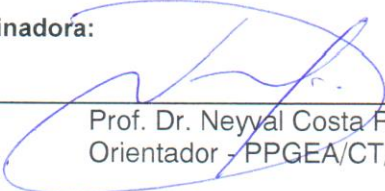


UNIVERSIDADE FEDERAL DO ESPÍRITO SANTO
CENTRO TECNOLÓGICO
PROGRAMA DE PÓS-GRADUAÇÃO EM ENGENHARIA AMBIENTAL

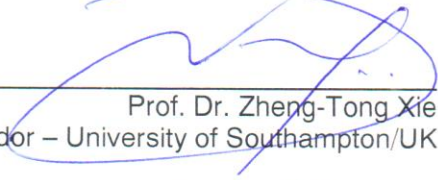
LARGE EDDY SIMULATION OF POLLUTANT DISPERSION FROM AN AREA SOURCE OVER RANDOM HEIGHT BUILDINGS ARRAYS

Vitor Ferreira Lavor

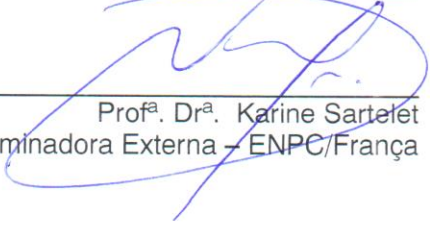
Banca Examinadora:


Prof. Dr. Neyval Costa Reis Jr.
Orientador - PPGEA/CT/UFES


Prof.ª Dr.ª Elisa Valentim Goulart
Coorientadora - PPGEA/CT/UFES


Prof. Dr. Zheng-Tong Xie
Coorientador - University of Southampton/UK


Prof. Dr. Bruno Furieri
Examinador Interno - PPGEA/CT/UFES


Prof.ª Dr.ª Karine Sartelet
Examinadora Externa - ENPC/França

Diogo Costa Buarque
Coordenador do Programa de Pós-Graduação em Engenharia Ambiental
UNIVERSIDADE FEDERAL DO ESPÍRITO SANTO

Vitória-ES, 11 de março de 2019.

To my parents, Vanderley and Mary Jane.

To my sisters, Ana Paula and Luiza.

ACKNOWLEDGMENTS

I would like to express my gratitude for my parents who have always believed in me and encouraged my studies. I will always be grateful for the education and the good examples. The support of my sisters Ana Paula and Luiza, and my girlfriend Brigitte was also fundamental to my success. Thank you!

I am grateful to my supervisor Neyval Costa Reis Jr., for all the trust he had on me. He gave me the opportunity to be part of his research group, which definitely changed my path inside the academy and in my life. Thank you for all the support, help and patience during these years.

I also wish to thank professor Zheng-Tong Xie, who strongly contributed to the development of my research. I can say that his expertise and academic performance in the area became a great inspiration for me to continue working hard to pursue further studies in academic area.

I would like to express my thanks to all professors of the Department of Environmental Engineering at UFES for sharing their knowledge. I would especially like to thank Elisa Valentim Goulart, who co-supervised me and always believed in my work and Jane Meri Santos, who inspired me since the first class of Atmospheric Dispersion of Contaminants.

Special thanks to my partners, Igor Richa Menegatti and Elson Silva Galvão. It was a great pleasure for me to work and grow day after day beside you.

I would like to thank my co-workers and colleagues at NQualiAr with whom I shared many moments in the laboratory during these years. Thanks to Ana Teresa, Ramon Martins, Alexandre Santiago, Victória Venturini, Jamily Faé, Luisa Peláez, Mayana Rigo, Yasmin Kaore, Karine Klippel, Felipe Maciel, Vitor Mateus, Adrielle de Melo, and Izabele Toniato.

I am grateful for the funding support provided by the National Council for Scientific and Technological Development (CNPq) and Espírito Santo Research Foundation (FAPES) in Brazil and by the Newton Research Collaboration Programme Award NRCP1617-6-140, administered by the U.K. Government's Newton Fund. Without this support, my dissertation would not have been possible.

“The mind that opens to a new idea never returns to its original sizes.”

Albert Einstein

ABSTRACT

Large-eddy simulation (LES) is used to study the turbulent flow and the pollutant dispersion over urban-like arrays, where an area source was placed on the ground. Three different geometries are considered: two staggered building arrays, one with uniform building height and another with non-uniform building heights, and an aligned array with random height buildings. The spatial and temporal average of the streamwise velocity and time-averaged concentration are compared with measurements from a wind tunnel experiment in order to assess the accuracy of the results (CHENG; CASTRO, 2002a; PASCHEKE; BARLOW; ROBINS, 2008). These comparisons indicate that LES is adequate to capture the turbulent flow and the pollutant dispersion over the assessed configurations. The results obtained in the present study show that the height variability of the buildings is an important parameter to study the flow and dispersion phenomena in urban areas. Besides the building height variability, local geometrical features proved to be relevant to determine the dispersion behaviour such as the presence of a taller building upwind the approaching flow. It is shown that the turbulent motions are responsible for the vertical turbulent flux of pollutant leaving/entering the urban canopy. The intensity of the turbulent structures seems to be related to the building height variation, since the higher the building height, the greater is the layer in which the flow has larger vertical velocity fluctuations. Results also show that the vertical scalar flux close to the area source can affect downwind clean zones. The vertical advective scalar flux was found to have an effect on dispersion in the vicinity of the building (a local effect), while the vertical turbulent fluxes are associated with pollutant transportation downwind above the smaller buildings (a non-local effect).

Keywords: Urban areas, Large-eddy simulation, Pollutant dispersion, Random building heights, Vertical scalar fluxes

RESUMO

A simulação das grandes escalas (LES) é utilizada para simular o fluxo turbulento e a dispersão de poluentes sobre configurações urbanas, onde uma fonte área foi inserida no chão. Três diferentes geometrias são consideradas: dois arranjos escalonados, um com prédios de alturas uniformes e um com prédios de alturas não-uniformes, e um arranjo alinhado com prédios de alturas aleatórias. A média espacial e temporal da velocidade média e a média temporal da concentração são comparadas com as medidas experimentais de um experimento em túnel de vento para avaliar a precisão dos resultados (CHENG; CASTRO, 2002a; PASCHEKE; BARLOW; ROBINS, 2008). As comparações indicam que LES é adequado para capturar o fluxo turbulento e a dispersão de poluentes nas configurações analisadas. Os resultados obtidos no presente estudo mostram que a variabilidade da altura dos prédios é um importante parâmetro para estudar os fenômenos do escoamento e a dispersão em áreas urbanas. Além da variabilidade da altura dos prédios, características locais da geometria provaram serem relevantes para determinar o comportamento da dispersão como, por exemplo, a presença de um prédio mais alto à montante do escoamento principal. É mostrado que os movimentos de ordem turbulenta são responsáveis pelo fluxo vertical turbulento de poluição entrando e saindo do dossel. A intensidade das estruturas turbulentas parece ter ligação com a variação da altura dos prédios, uma vez que quanto maior altura do prédio, maior será a camada na qual o escoamento terá maiores flutuações da velocidade vertical. Os resultados também mostram que o fluxo vertical de escalar próximo à fonte área pode afetar áreas limpas mais afastadas. O fluxo vertical advectivo de escalar possui um efeito sobre a dispersão nas proximidades do prédio (um efeito local), enquanto os fluxos verticais turbulentos estão associados com o transporte de poluentes na direção do escoamento principal acima dos edifícios menores (um efeito não-local).

Palavras-chave: Áreas urbanas, Simulação das grandes escalas, Dispersão de poluentes, Prédios com alturas aleatórias, Fluxos verticais de escalar

LIST OF ACRONYMS

CFD	Computational fluid dynamics
CV	Control volume
DIPOS	Dispersion of localised releases in a street network
DNS	Direct numerical simulation
FVM	Finite volume method
LES	Large-eddy simulation
MUSCL	Monotone upstream-centered schemes for conservation laws
NQualiAr	Núcleo de qualidade do ar
RANS	Reynolds averaged Navier-Stokes
RBAA	Random height buildings in an aligned array
RBSA	Random height buildings in a staggered array
SIMPLE	Semi-implicit method for pressure-linked equations
SGS	Subgrid-scale
UBSA	Uniform height buildings in a staggered array

LIST OF VARIABLES

Roman letters

$2D$	Two-dimensional [-]
$3D$	Three-dimensional [-]
A	Area [m^2]
c	Concentration of a chemical specie [kg/m^3]
c^*	Normalised concentration [-]
c_0	Constant concentration at the area source [kg/m^3]
C_d	Drag coefficient [-]
C_{ij}	Cross-stress tensor [Pa]
C_s	Smagorinsky constant [-]
$\langle \bar{c} \bar{u} \rangle$	Horizontal total flux [$kg/m^2.s$]
$\langle \bar{c} \rangle \langle \bar{u} \rangle$	Horizontal advective flux [$kg/m^2.s$]
$\langle \bar{c}' \bar{u}' \rangle$	Horizontal turbulent flux [$kg/m^2.s$]
$\langle \bar{c} \bar{w} \rangle$	Vertical total flux [$kg/m^2.s$]
$\langle \bar{c} \rangle \langle \bar{w} \rangle$	Vertical advective flux [$kg/m^2.s$]
$\langle \bar{c}' \bar{w}' \rangle$	Vertical turbulent flux [$kg/m^2.s$]
d	Displacement height [m]; Distance to the closest wall [m]
D_m	Molecular diffusivity of a chemical specie [$kg/m.s$]
D_s	SGS turbulent diffusivity [$kg/m.s$]
f	Any flow variable [-]
\bar{f}	Resolved scale of any flow variable [-]
f'	Subgrid-scale of any flow variable [-]
H	Building height [m]

H_m	Average building height [m]
k	Turbulent kinetic energy [m^2/s^2]; Wavenumber [1/m]
k_c	Cut-off wavenumber [1/m]
L	Lateral building length [m]
L_s	Smagorinsky length [m]
L_x	Length in the direction x [m]
L_y	Length in the direction y [m]
L_z	Length in the direction z [m]
N_{faces}	Number of faces [-]
\mathbf{n}	Normal vector [-]
p	Fluid static pressure [N/m^2]
\bar{p}	Resolved static pressure [N/m^2]
\bar{P}	Modified static pressure [N/m^2]
$\vec{\mathbf{r}}$	Displacement Vector [-]
R_{ij}	SGS Reynolds stress tensor [Pa]
Re_τ	Reynolds number based on total wall friction velocity [-]
S	Source rate of a chemical specie [$\text{kg}/\text{m}^3 \cdot \text{s}$]; Rate of strain [Pa]
Sc_m	Molecular Schmidt number [-]
Sc_s	Subgrid Schmidt number [-]
\bar{S}_{ij}	Filtered rate of strain [Pa]
S_ϕ	Source rate any variable [-]
t	Time [s]
T	Total averaging time [s]
T_c	Characteristic time-step [s]
T_s	Time-step [s]
u_i, u_j	Velocity component in the direction i and j [m/s]

\bar{u}_i, \bar{u}_j	Resolved part of velocity component i and j [m/s]
u'_i, u'_j	Subgrid part of velocity component i and j [m/s]
u^*	Normalised streamwise velocity [-]
u_τ	Total wall friction velocity [m/s]
V	Volume [m ³]
W	Street width [m]
w^*	Normalised vertical velocity [-]
w	Vertical velocity [m/s]
x, y, z	Cartesian coordinates [m]
x_i, x_j	Cartesian coordinate in the direction i and j [m]
z_o	Roughness length [m]

Greek letters

Γ	Characteristic diffusion coefficient [-]
Δ	Filter cut-off length [m]
$\Delta_{x_1}, \Delta_{x_2}, \Delta_{x_3}$	Cut-off length for uniform grids [m]
Δ_t	Time-step [s]
ε	Turbulence energy dissipation rate [m ² /s ²]
κ	Von Kármán constant [-]
λ_F	Frontal area density [-]
λ_P	Plan area density [-]
μ	Fluid dynamic viscosity [Pa.s]
μ_t	Turbulent viscosity [Pa.s]
ν	Kinematic viscosity [m ² /s]
ν_s	Subgrid kinematic viscosity [m ² /s]

ρ	Fluid density [kg/m ³]
τ_{ij}	Subgrid stress tensor [Pa]
τ_{kk}	Isotropic term of subgrid stress tensor [Pa]
ω	Specific dissipation rate [1/s]
ϕ	General variable of interest [-]

Operators

$\langle \rangle$	Spatial averaging process
$-$	Filtered variables; Temporal averaging process
∇	Gradient operator
G	Filter function
δ_{ij}	Delta of Kronecker

LIST OF FIGURES

Figure 1. Urban-type configurations commonly used in CFD studies: (a) group of buildings, (b) street canyon and (c) courtyard. Adapted from Toparlar et al. (2017).....	21
Figure 2. A view of (a) vertical and (b) horizontal plume dispersion in a staggered buildings array (BELCHER, 2005).....	22
Figure 3. Flow pattern around an isolated building (BLOCKEN et al., 2011).	25
Figure 4. Flow pattern inside an urban canyon (VARDOULAKIS et al., 2003)	27
Figure 5. Flow regimes under different aspect ratios (OKE, 1988)	28
Figure 6. Flow regime classifications and its specific threshold lines (OKE, 1988)	29
Figure 7. Contours of velocity at $z = 2\text{m}$ for various urban morphologies and wind directions: (a) 0° , (b) 15° , (c) 30° and (d) 45° . Adapted from Lin et al. (2014).....	33
Figure 8. Contours of normalised concentration at $z/H_m = 1.20$ for (a) uniform height buildings array and (b) random height buildings array, where h is the average height of the buildings (BOPPANA; XIE; CASTRO, 2010)	35
Figure 9. Plan view of different urban configurations: (a) staggered array with random buildings height (RBSA), (b) aligned array with random building height (RBAA) and (c) staggered array with uniform buildings height (UBSA).	39
Figure 10. Representation of the resolved and subgrid scales after a sharp cut-off in physical and Fourier space (SAGAUT, 2006).....	42
Figure 11. Three-dimensional sketch of RBSA case with the respective boundary conditions highlighted.....	47
Figure 12. Typical (a) three-dimensional, (b) (c) one-dimensional schematic view for control volume discretization. Adapted from Versteeg and Malalasekera (2007)	51
Figure 13. Cross section of the computational mesh showing three refinement levels for RBSA array. The inflation zone near the ground is also highlighted. The value of the vertical spacing, $\Delta_n = 1, 2, 3$ are mentioned in the text.....	52
Figure 14. Profiles of the spatial average of the mean streamwise velocity (a) for RBSA and (b) for UBSA. Square symbols represent Cheng and Castro (2002a) experimental data, broken lines represent LES results produced by Boppana, Xie and Castro (2010) and solid lines represent the present work	55
Figure 15. Plan view of RBSA configuration. Black dots indicate the locations of the vertical concentration profiles and dotted lines indicate the locations of the lateral profiles .	56

- Figure 16. Lateral concentration profiles (a) near and (c) away from the source for RBSA and (b) near and (d) away from the source for UBSA configuration calculated at $z/H_m = 0.6$. Lines represent the present results and symbols indicate wind tunnel data57
- Figure 17. Vertical concentration profiles (a) near and (c) away from the source for RBSA and (b) near and (d) away from the source for UBSA configuration. Lines represent the present results and symbols indicate wind tunnel data.....58
- Figure 18. Horizontal plan view of streamlines of time-averaged flow field at (a) $z/H_m = 0.28$ and (d) $z/H_m = 1.00$ for UBSA, (b) $z/H_m = 0.28$ and (e) $z/H_m = 1.00$ for RBSA, (c) $z/H_m = 0.28$ and (f) $z/H_m = 1.00$ for RBAA 60
- Figure 19. Time-averaged velocity vectors in the $x - z$ plane located at (a) $y/H_m = -1.5$ for UBSA. Instantaneous velocity vectors in the $x - z$ plane at $y/H_m = 0.5$ (b) above the area source and (c) further away from the area source for UBSA. Arrows indicate the direction of the flow and numbers indicate the building height in millimetres 62
- Figure 20. Plan view with indications for the group of buildings with (a) at least one building lower than the average height, (b) at least one building taller than the average height and (c) one building taller and one lower than the average height for RBSA 63
- Figure 21. Time-averaged velocity vectors in the $x - z$ plane located at (a) $y/H_m = -3.5$, (b) $y/H_m = -1.5$ and (c) $y/H_m = 0.5$ for RBSA. Arrows indicate the direction of the flow and numbers indicate the building height in millimetres 64
- Figure 22. Plan view with indications for the group of buildings with (a) at least one building lower than the average height, (b) at least one building taller than the array average height and (c) one building taller and one lower than the average height for RBAA 65
- Figure 23. Time-averaged velocity vectors in the $x - z$ plane located at (a) $y/H_m = -3.5$, (b) $y/H_m = -1.5$ and (c) $y/H_m = 0.5$ for RBAA. Arrows indicate the direction of the flow and numbers indicate the building height in millimetres 66
- Figure 24. Contours of normalised streamwise velocity in the $x - y$ plane located at (a) $z/H_m = 0.28$ and (d) $z/H_m = 1.00$ for UBSA, (b) $z/H_m = 0.28$ and (e) $z/H_m = 1.00$ for RBSA, (c) $z/H_m = 0.28$ and (f) at $z/H_m = 1.00$ for RBAA 68
- Figure 25. Contours of normalised vertical velocity in the $x - y$ plane located at (a) $z/H_m = 0.28$ and (d) $z/H_m = 1.00$ for UBSA, (b) $z/H_m = 0.28$ and (d) $z/H_m = 1.00$ for RBSA, (c) $z/H_m = 0.28$ and (f) $z/H_m = 1.00$ for RBAA 70
- Figure 26. Distribution of normalised vertical velocity and vertical velocity *rms* in the $x - z$ plane located at $y/H_m = -1.5$ for (a) (b) UBSA and (c) (d) RBSA and (e) (f) RBAA 71

- Figure 27. Contours of normalised concentration at (a) $z/H_m = 0.28$, (d) $z/H_m = 1.00$ and (g) $z/H_m = 1.72$ for UBSA, (b) $z/H_m = 0.28$, (e) $z/H_m = 1.00$ and (h) $z/H_m = 1.72$ for RBSA, (c) $z/H_m = 0.28$, (f) $z/H_m = 1.00$ and (i) $z/H_m = 1.72$ for RBAA. 74
- Figure 28. Mean normalised concentration iso-surfaces for (a) UBSA, (b) RBSA and (c) RBAA configurations 75
- Figure 29. Contours of normalised concentration in the $x - z$ plane at $y/H_m = 6.0$ for UBSA. The numbers indicate the building height in millimetres 77
- Figure 30. Plan view with indications for the group of buildings with (a) at least one building lower than the average height, (b) at least one building taller than the average height and (c) one building taller and one lower than the average height for RBSA 77
- Figure 31. Contours of normalised concentration in the $x - z$ plane located at (a) $y/H_m = -3.5$, (b) $y/H_m = -1.5$ and (c) $y/H_m = 0.5$ for RBSA. The numbers indicate the building height in millimetres..... 78
- Figure 32. Plan view with indications for the group of buildings with (a) at least one building lower than the average height, (b) at least one building taller than the array average height and (c) one building taller and one lower than the average height for RBAA 79
- Figure 33. Contours of normalised concentration in the $x - z$ plane located at (a) $y/H_m = -3.5$, (b) $y/H_m = -1.5$ and (c) $y/H_m = 0.5$ for RBAA. The numbers indicate the building height in millimetres..... 80
- Figure 34. Quantities of normalised (a) total, (b) turbulent and (c) advective vertical scalar fluxes for UBSA configuration. (d) Schematic representation and sampled locations. Symbols indicate the locations behind the building (\diamond), between buildings (\circ) and in front of the building (\square)..... 82
- Figure 35. Quantities of normalised (a) total, (b) turbulent and (c) advective vertical fluxes for the RBSA configuration. (d) Schematic representation and sampled locations. Symbols indicate the locations behind the building (\diamond), between buildings (\circ) and in front of the building (\square)..... 84
- Figure 36. Quantities of normalised (a) total, (b) turbulent and (c) advective vertical fluxes for RBSA configuration. (d) Schematic representation and sampled locations. Symbols indicate the locations behind the building (\diamond), between buildings (\circ) and in front of the building (\square)..... 85
- Figure 37. Quantities of normalised (a) total, (b) turbulent and (c) advective vertical fluxes for RBAA configuration. (d) Schematic representation and sampled locations. Symbols indicate the locations between buildings (\circ)..... 86

- Figure 38. Quantities of normalised (a) total, (b) turbulent and (c) advective vertical fluxes for RBAA configuration. (d) Schematic representation and sampled locations. Symbols indicate the locations between buildings (\circ)..... 87
- Figure 39. Quantities of normalised (a) total, (b) turbulent and (c) advective vertical fluxes with a plan view of (d) RBAA configuration. Symbols indicate the location between buildings (\circ) and intersections (\square)..... 88
- Figure 40. Non-dimensional vertical scalar fluxes (total, advective and turbulent) on a horizontal plane located at $z/H_m = 1.0$ for (a), (b) and (c) UBSA, (d), (e) and (f) RBSA and (g), (h) and (i) RBAA, respectively 90
- Figure 41. Plan view of the regions marked with the capital letters A, B and C denoting repeating units comprising sixteen blocks ($8H_m \times 8H_m$), where the light blue zone coincides with the area source, for RBSA..... 91
- Figure 42. Spatially averaged vertical profiles of non-dimensional vertical scalar flux for the UBSA (a, b, c), RSAA (d, e, f), and RBAA (g, h, i) configurations. Solid lines represent the total scalar flux, broken lines represent the turbulent scalar flux and dotted lines represent the advective scalar flux. Capital letters indicate the urban zones 93
- Figure 43. Spatially averaged vertical profile of horizontal scalar flux for UBSA (a, b, c) RBSA (d, e, f) and for RBAA (g, h, i) configurations. Solid lines represent the total scalar flux, broken lines represent the turbulent scalar flux and dotted lines represent the advective scalar flux. Capital letters indicate the urban zones..... 95
- Figure 44. Ratio between vertical and averaged horizontal fluxes leaving zone A, for (a) $z/H_m = 0.0$ to $z/H_m = 1.0$ and (b) $z/H_m = 1.0$ to $z/H_m = 1.72$ 96

CONTENT

1	INTRODUCTION	20
2	LITERATURE REVIEW	24
2.1	FLOW AND DISPERSION AROUND ISOLATED OBSTACLES	24
2.2	FLOW AND DISPERSION IN URBAN CANYONS	26
2.3	FLOW AND DISPERSION IN URBAN CANOPIES	31
3	METHODOLOGY	38
3.1	SIMULATED CASES	38
3.2	MATHEMATICAL MODELLING.....	40
3.2.1	Governing Equations	40
3.2.1.1	Large-Eddy Simulation Equations.....	41
3.2.1.1.1	Subgrid-Scale Modelling	45
3.2.2	Boundary Conditions	47
3.3	NUMERICAL METHODS.....	48
3.3.1	The Finite Volume Method	49
3.3.2	Mesh Parameters.....	52
3.4	STATISTICS AND COMPUTATIONAL FACILITY	53
4	RESULTS.....	54
4.1	COMPARISON WITH A WIND TUNNEL EXPERIMENT AND LES SIMULATION	54
4.2	FLOW FIELD	59
4.3	CONCENTRATION FIELD.....	72

4.4	POLLUTANT FLUXES	80
5	CONCLUSIONS.....	97
5.1	FUTURE WORK RECOMMENDATION.....	99
	REFERENCES	100

1 INTRODUCTION

Air pollution in urban areas is a current issue and every day becomes more relevant due to short and long-term effects on population health, mainly affecting people who live in high-density populated cities (YUAN; NG; NORFORD, 2014). Urban pollution such as vehicular exhausts, particles resuspension and industrial emissions are often toxic and odorous. These are responsible to cause discomfort and harm to humans and other living organisms (LATEB et al., 2016). Many studies have found important relationship between the increasing of pollutants concentration and human morbidity/mortality (HUANG et al., 2018; KAMPA; CASTANAS, 2007).

Rapid urbanization and the evident impact associated with atmospheric pollution encouraged several researchers around the world to study airflow and dispersion patterns in urban areas. This is affected not only by micro-scale meteorological phenomena but also by the presence of buildings and other urban elements. Field measurements in full and reduced scale, laboratory-scale physical experimental measurements (e.g. wind tunnel or water tank analyses) and computational fluid dynamics (CFD) approaches are tools commonly used in the study of pollution dispersion (LI et al., 2006).

The main advantage of CFD simulations is cost and the possibility of providing information throughout the entire computational domain, while observational techniques are more expensive and often provide information at limited discrete points in space (TOPARLAR et al., 2017). The growth in spatial and temporal resolution with ever-increasing computational power has guaranteed greater reliability for CFD-based models to provide more accurate information of transport phenomena. The most commonly utilized turbulence models are based on large-eddy simulation – LES and Reynolds averaged Navier-Stokes – RANS, since the use of direct numerical simulation – DNS is highly costly in terms of computational resources.

The use of large-eddy simulation to acquire data of turbulent flows and pollutant dispersion has become ever more relevant in environmental studies. The strategy is to solve explicitly only the large-scale structures of motion, and model the effects of the smaller and more universal scales. One of the main reasons for the growth in its use is the availability of required computational power in academic and industrial high-performance computing laboratories and the well-known recognition that RANS models are not able to adequately predict fundamental physical concepts, such as transient vortices, periodic fluctuations, reverse flow intensity behind obstacles and other refined details. (XIE; CASTRO, 2006).

Naturally turbulent, the atmospheric flow is strongly influenced by urban morphology, which comprises some characteristics such as size, shape and how arranged the buildings are in space. However, the vast majority of the studies still treat urban morphology in a generic and idealized way. Urban configurations are commonly represented by a single or a group of buildings (COCEAL et al., 2006, 2007; GOULART et al., 2016), street canyons (KUBILAY et al., 2017; NEOPHYTOU; MARKIDES; FOKAIDES, 2014) or, in more recent works, courtyards-type buildings, representing a set of street urban canyons (NOSEK et al., 2016, 2017, 2018), as demonstrated in Figure 1.

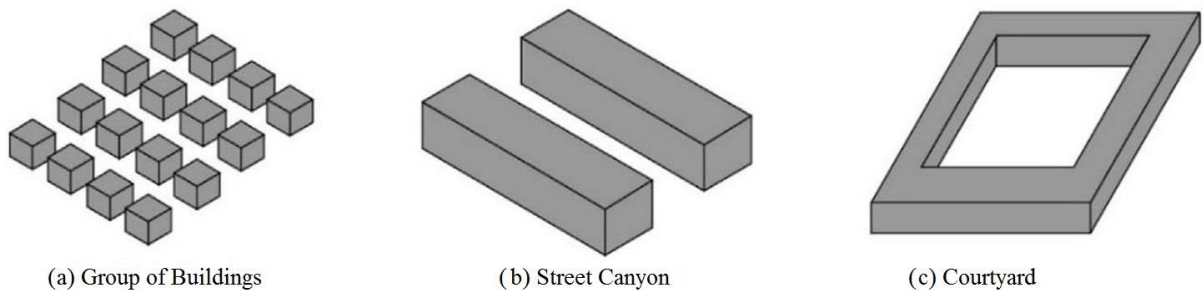


Figure 1. Urban-type configurations commonly used in CFD studies: (a) group of buildings, (b) street canyon and (c) courtyard. Adapted from Toparlak et al. (2017)

Nevertheless, some authors consider slightly more complex urban configurations in their studies, seeking to assess the influence of different building heights in the airflow and pollutant dispersion (BOPPANA; XIE; CASTRO, 2010; CHENG; CASTRO, 2002b; PHILIPS; ROSSI; IACCARINO, 2013). Other researchers have studied what they call “real urban areas” that cover a small portion of real sites in order to analyse the complexity of irregular urban configurations in a more detailed way (SANCHEZ et al., 2017; SANTIAGO et al., 2017; SHEN; CUI; ZHANG, 2017). However, an accurate comparison between experiments measurements and numerical data for those attempts becomes more intricate.

Regarding how pollutant spreads in urban areas, two main processes are responsible to determine the pollutant plume behaviour. Both are related to the interaction between the mean flows with the roughness elements that constitute the urban environment, which carries the pollutant away from any source emission. In a general way, the mean flow is responsible for the horizontal advection through the urban canopy and the buildings are responsible for promoting great turbulence levels. The increasing of turbulence enhances vertical exchanges with the clean air above it (PASCHEKE; BARLOW; ROBINS, 2008). In this way, the characteristics of the pollutants plume will be given by a balance between the turbulent and advective contributions as can be seen in Figure 2.

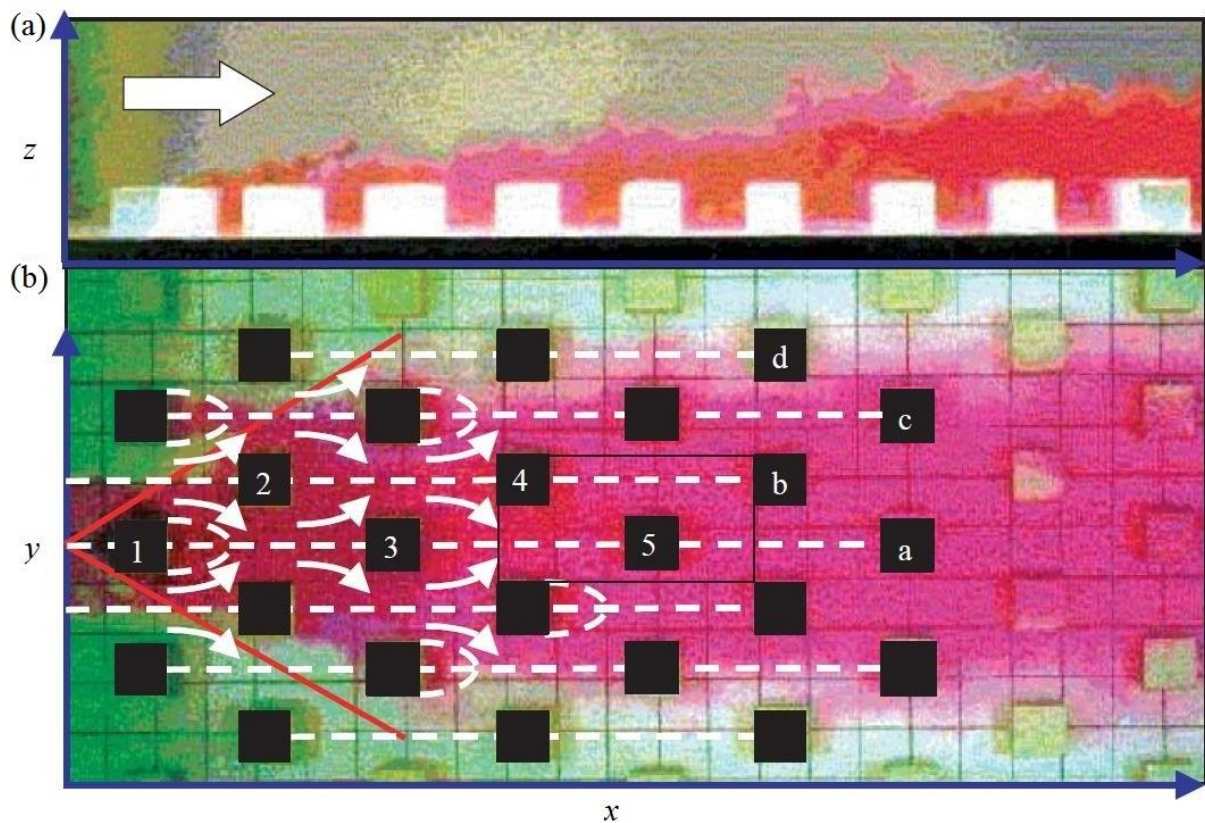


Figure 2. A view of (a) vertical and (b) horizontal plume dispersion in a staggered buildings array (BELCHER, 2005)

Recently, Goulart, Coceal and Belcher (2018) investigated the interaction of pollutant dispersion between the interior and exterior zones over an aligned urban canopy by means of DNS data and demonstrated that the vertical pollutant mass flux is dominated by the turbulent component at the building height. On the other hand, Carpentieri et al. (2018), in their wind tunnel experiment of two rectangular building arrays, were able to conclude that both advective and turbulent vertical scalar fluxes have a similar order of magnitude at the same height. In

addition, the advective component was found to have a leading role on horizontal scalar flux below the canopy, in both studies.

Carpentieri et al. (2018) results evidenced a significant effect over the vertical scalar transfer due to the presence of a taller and isolated building upwind of measurements. Similar characteristics were found by Fuka et al. (2018), which demonstrated that the presence of taller buildings alters significantly the flow field and it is responsible for the decrease or increase of the vertical scalar transfer depending on the location of the source relative to the tall building.

The present dissertation aims to investigate and understand the dispersion in urban configurations focusing on the effects of different building heights on pollutant mass transfer mechanisms by means of large-eddy simulation. Three urban-like configurations will be evaluated, two staggered arrays (uniform and random height buildings), consisting of the same geometric features studied by Cheng and Castro (2002) and one aligned array with random building heights, in which an area source is spatially distributed on part of the domain ground.

In order to achieve the main objective, specific objectives were determined and are listed below:

- Perform large-eddy simulation of flow and dispersion of a pollutant with continuous release from an area source within the urban canopy;
- Evaluate the accuracy of numerical simulation results based on direct comparison with experimental data obtained by Pascheke, Barlow and Robins (2008) and LES data obtained by Boppana, Xie and Castro (2010);
- Investigate the mechanisms that affect the pollutant mass transfer for uniform and random height buildings arrays;
- Determine local and non-local influences of different building heights over vertical and horizontal transport mechanisms.

This dissertation is divided into five chapters. After this brief introduction, Chapter 2 covers a literature review about the flow and dispersion within urban areas and the state of the art about the theme. Mathematical modelling, numerical methods and computational configurations are described in Chapter 3. Chapter 4 contains the results for the simulated test cases and a closing chapter with a proper conclusion is presented in Chapter 5.

2 LITERATURE REVIEW

In this chapter, some fundamental concepts of the wind flow and pollutant dispersion and state of the art of the most common representations of urban areas are presented. This chapter is divided into three sections. Section 2.1 characterizes the complex flow and, consequently, the dispersion pattern around a single and isolated obstacle. Section 2.2 covers another common urban morphology that are the urban canyons with its unique characteristics, while Section 2.3 describes the flow and dispersion over a group of buildings representing more actual urban configurations.

2.1 FLOW AND DISPERSION AROUND ISOLATED OBSTACLES

In the context of the urban boundary layer, a very important topic is the prediction of wind flow pattern around obstacles. Such comprehension is essential to provide the necessary support to a wide range of studies related to the dispersion of atmospheric pollution in urban environments. Firstly, it is mandatory to understand the phenomena around an isolated building in order to comprehend how it affects other obstacles in its proximity.

In a general way, the characteristic structures of the flow around a single obstacle can be observed in Figure 3. Despite the complexity, it is possible to identify some specific regions. The pressure distribution right in front of the obstacle is responsible to divide the flow near the upper part of the incident wall. The location where the velocity is zero is called stagnation region. From this zone, the fluid flows towards the ground and returns upwind the obstacle. This region presents a structured vortex and its characteristics are dependent on the obstacle dimensions.

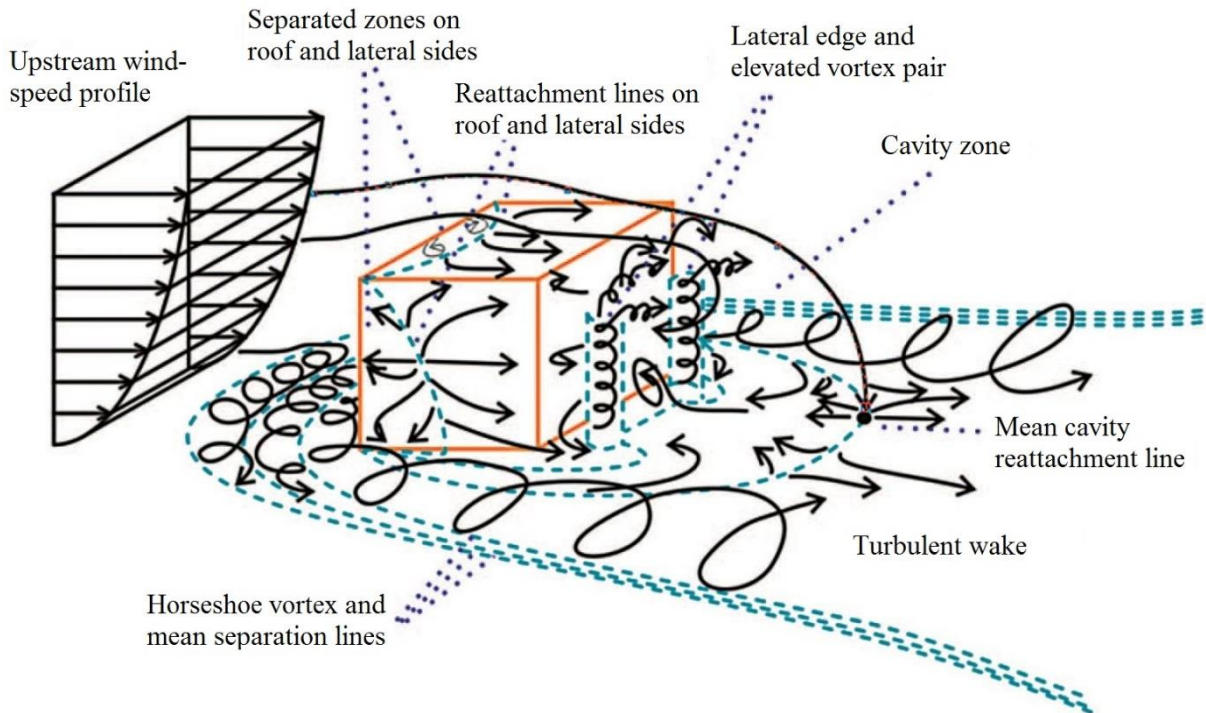


Figure 3. Flow pattern around an isolated building (BLOCKEN et al., 2011).

The generated vortex is developed towards the ground and spreads laterally around the obstacle surface due to convection effects, leading to the formation of the well-known *horseshoe vortex*. The flow is accelerated vertically and laterally and small recirculation zones and reverse flow are observed next to the top and lateral faces due to the local separation of the mean flow. The mean flow takes a while to regain the characteristics of the upstream wind-speed profile. This point is called *reattachment* line and occurs differently on roof and building sides. The flow is also separated behind the obstacle, where a region with intense circulatory motion, low velocities and high turbulence intensity is observed. This zone is named *cavity zone* and presents strong vertical motion. The entire region after the building, where still persists a minimum turbulent effect configures the *turbulent wake*.

There are several works in the literature focused on evaluating the flow and dispersion around a single obstacle using different approaches as wind tunnel and water tank experiments (MAVROIDIS; GRIFFITHS; HALL, 2003; ROBINS; CASTRO, 1977a), CFD-based numerical simulations using Reynolds averaged Navier-Stokes (MURAKAMI, 1993; SANTOS et al., 2009; VARDOULAKIS et al., 2011) and large-eddy simulation (AI; MAK, 2015).

Castro and Robins (1977) and Robins and Castro (1977) can be considered two of the first paper works investigating the dispersion over an isolated building. They used wind tunnel technique

to simulate an atmospheric boundary layer ten times bigger than the building height over a uniform and sheared turbulent flow. They observed an increase in the inflow turbulence results in smaller cavity zone. They also concluded that the cavity zone length is about $1.5H$ and the turbulent wake is almost completely distinguished within about $6.0H$, where H is the building height.

The study developed by Mavroidis, Griffiths and Hall (2003), using wind tunnel and field experiments investigated the air flow and the dispersion of a tracer emitted from a continuous point source located upstream an isolated obstacle. Different building shapes and wind directions have been evaluated. They observed that the dispersion due to the disturbed flow in the turbulent wake is closely influenced by the building height and shape. The source location relative to the building also influences the dispersion pattern. For example, lower concentrations are observed near the ground behind taller buildings due to the more intense recirculation in this zone. Moreover, good agreement was observed between both technique results, despite the fact that the plume was more dispersed in the field experiment due to uncontrolled atmospheric instability.

Numerical simulations were carried out by Tominaga and Stathopoulos (2010) in order to evaluate the accuracy of RANS and LES models to predict pollutant dispersion around a three-dimensional cubic building. According to the authors, the performance of LES was superior in predicting the concentration field since it is possible to obtain important information about turbulent transient fluctuations. Although the difference between LES and RANS is not strongly remarkable on mean velocity profiles, accurate information regarding the diffusion of concentration cannot be obtained by means of RANS formulation, since the important unsteady fluctuations are only modelled.

2.2 FLOW AND DISPERSION IN URBAN CANYONS

The term urban canyon represents an idealized urban configuration, where two buildings are aligned in parallel to each other and separated by a relatively narrow street, which is very common in high-density cities. In real cities, there are street widths and building heights variations that are responsible for creating unique flow and dispersion patterns within the canyons (LI et al., 2006; TOMINAGA; STATHOPOULOS, 2013). This motivated a large quantity of researches focused on this basic urbanized configuration.

The dimensions of urban canyons are usually expressed by its aspect ratio, which is the building height (H) divided by the respective street width (W) as can be seen in Figure 4. In case of perpendicular flow approaching the lined up pair of buildings, two different regions appear inside the canyon. The first region is the *windward side* with downdraft motion responsible for carrying clean air from above the building, and the second region is the *leeward side* characterized by updraft flow in the other side, which is responsible to transport polluted air from inside the canyon to the outer zone.

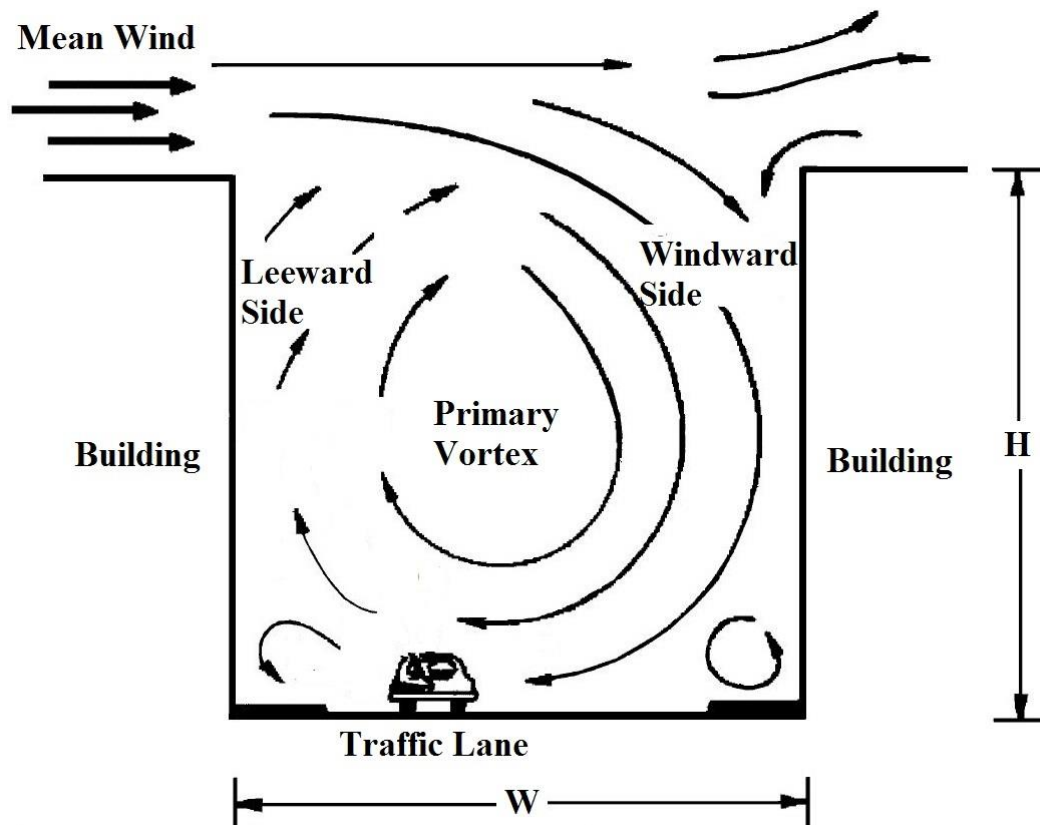


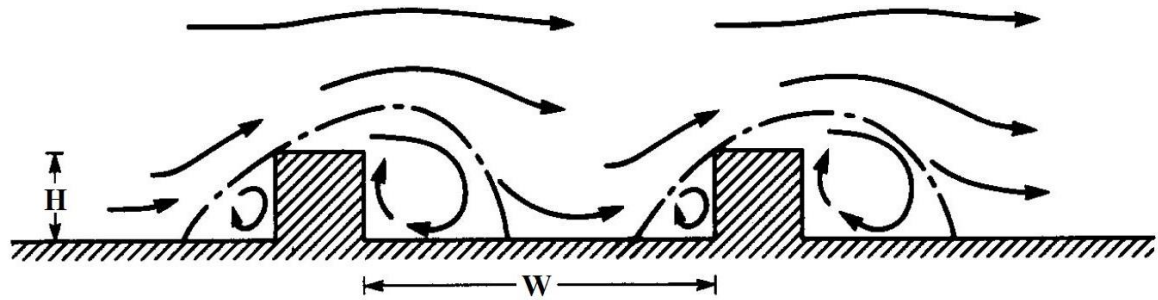
Figure 4. Flow pattern inside an urban canyon (VARDOULAKIS et al., 2003)

Based on wind tunnel experiments under isothermal conditions, Oke (1988) proposed a systematic classification of wind flow regime based on urban canyon aspect ratio. The vortex structure developed inside the canyon determines the regime of the flow. There are three flow regimes well characterized: isolated roughness flow, wake interference flow and skimming flow (Figure 5).

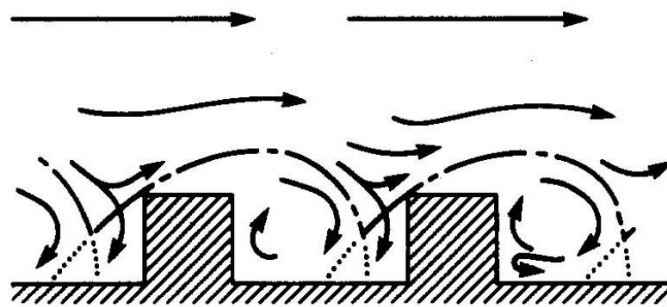
Aspect ratios smaller than 0.33 or, in other words, when the street width is about three times longer than the building height, there is practically no interaction between the turbulent wake with the subsequent building. Therefore, the flow regime is characterized as isolated roughness flow. The regime of wake interference flow occurs for aspect ratios between 0.33 and 0.70,

when the buildings are close enough and the turbulent wake of the previous building influences the next one. For aspect ratios greater than 0.70, the pair of buildings is so close that a stable vortex appears within the cavity, characterizing the skimming flow regime.

(a) Isolated Roughness Flow



(b) Wake Interference Flow



(c) Skimming Flow

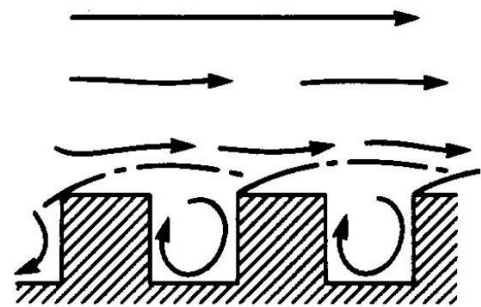


Figure 5. Flow regimes under different aspect ratios (OKE, 1988)

The lateral length of the building (L), normal to the mean flow, is also an important dimension. Another urban canyon parameter can be stated regarding that dimension called building aspect ratio, which determines the spatial organization of the buildings (VARDOULAKIS et al., 2003). The building aspect ratio is defined as L/H and there are three classifications based on it: short ($L/H \leq 3$), medium ($3 < L/H < 7$) and long urban canyon ($L/H \geq 7$). Thereby, when the lateral length is infinitely large, the flow inside the canyon tends to present only two-dimensional characteristics. Otherwise, three-dimensional features are observed due to the interaction between streets and intersections, as suggested by Carpentieri, Robins and Baldi (2009). In cases of short and medium urban canyons, two-dimensional geometries are no longer suitable for CFD-based numerical simulations, where a 3D geometry must be employed in the study. The flow regime classifications and the transition thresholds for both characteristic ratios are presented in Figure 6.

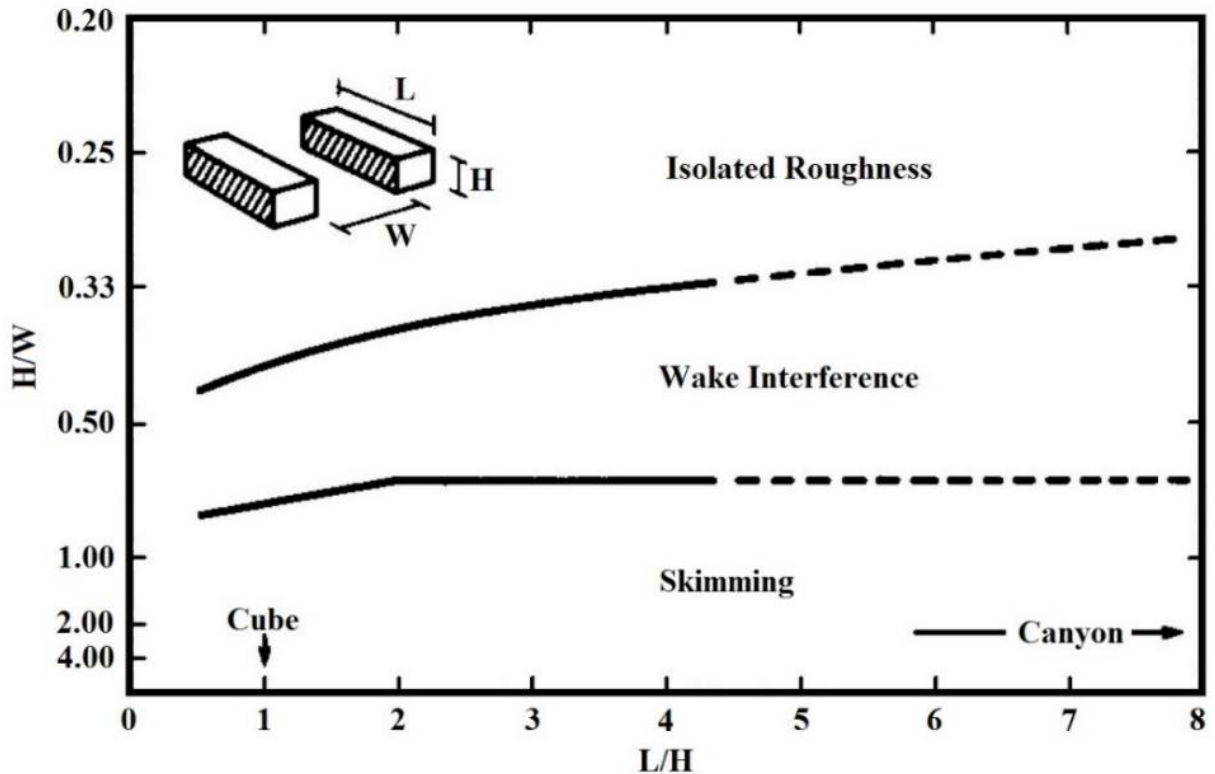


Figure 6. Flow regime classifications and its specific threshold lines (OKE, 1988)

In the context of pollutant dispersion in urban regions, a topic that has been studied is the interaction between the external and internal flow within the canyon. Liu, Leung and Barth (2005) investigated air ventilation and pollutant dispersion inside an urban canyon with three different aspect ratios (0.50, 1.00 and 1.50) using large-eddy simulation. The main objective was to predict the air rate entering the canyon and the pollutant rate that leaves the canyon. The Reynolds number and Schmidt number was equal to 12000 and 0.72, respectively. The authors concluded that urban canyons with large aspect ratios present lower turbulence intensity inside the canyon. This enhances the pollutant retention due to the poor ventilation and consequently, increases de concentration especially near the ground within the canyon. They also highlighted that the pollutant removal at the roof level is governed only by turbulent motions and occurs primarily at the leeward side.

Cai and Barlow and Belcher (2008) also studied the flow and concentration fields in urban canyons with different aspect ratios (0.33, 0.50, 0.66, 1.00, 1.50 and 2.00) by solving large-eddy simulation equations. A line source was placed in the middle of the canyon's ground and a scalar was emitted with a constant rate along the street. Their wind speed and turbulent kinetic profiles for the case with $H/W = 1.00$ had good agreement compared with wind tunnel experimental data, validating further investigation. Moreover, the mean scalar distribution

within the canyon was suitable with the flow regime classifications proposed by Oke (1988). They also remarked that LES predictions might be influenced by domain size.

In wind tunnel experiment studies, Salizzoni, Soulhac and Mejean (2009) sought to estimate the contribution of turbulent effects on pollutant mass transport between two-dimensional urban canyons. They analysed the influence of the external turbulent flow above it. The necessary time for all tracer released within the canyon reach and completely leave the cavity was used as parameter of analysis to calculate the pollutant mass transfer velocity. They concluded that turbulent fluctuations within the canyon are strongly influenced by the turbulent intensity of the outside flow. Therefore, high external turbulence increases the pollutant mass transfer velocity and consequently reduces the tracer residence time inside the canyon.

Michioka, Takimoto and Sato (2014) performed numerical simulations using large-eddy simulation in order to investigate and determine the responsible mechanisms of pollutant mass transport over a set of urban canyons. Five urban-type configurations with building aspect ratios of 1, 2, 4, 8 and ∞ were analysed. The pollutant was released from a line source located on the ground level of a target canyon. The Reynolds number, based on a reference velocity (at the top of the domain), and Schmidt number were equal to 8000 and 1, respectively. Stronger lateral dispersion was observed for smaller building aspect ratio, decreasing the local pollutant mean concentration. In addition, the main vortex is developed with stronger updraft motions at leeward side as the aspect ratio become larger. For all simulated cases, the advective vertical flux was larger at windward side, as expected. However, they indicated that the advective flux is responsible for further re-entrainment of pollutant within the urban canyon. They also concluded that the turbulent motions are mainly responsible for pollutant removal, presenting positive values in practically all regions of all studied cases.

Nosek et al. (2016, 2017) carried out an investigation in order to identify the influence of non-uniformities at rooftops along with both sides of the buildings using wind tunnel and LES. The focus was on pollutant mass transport processes and the determination of the mechanisms responsible for that transport. They considered three different urban canyons, formed by courtyard-type buildings, under perpendicular and oblique wind direction related to buildings length, with a constant ground level line source emission. The results demonstrated that non-uniformities of rooftops are crucial for coherent structure development inside the canyons, becoming an important factor to deteriorate or improve local air quality. Moreover, they have shown that vertical motions are dominated by turbulent flux and fairly dependent on the

geometry feature, while the wind direction did not considerably affect the transport mechanism contributions.

In a recent study, Kubilay et al. (2017) investigated the importance of pollutant exchange velocity in urban canyons, which is considered one of the main parameters associated with the air quality. They evaluated an urban canyon with aspect ratio equal to the unit for different source locations: near the ground in the middle of the street, near the windward and leeward sides in the middle of the buildings, at the centre of the canyon and uniformly distributed within the cavity. Their unsteady numerical simulation data showed that spatial concentration distribution is closely influenced by the source location. Naturally, concentration decreases as the flow moves away from the source, and a clear high concentration plume extends toward the mean flow. In the case of centre-located source, right in the middle of the canyon a low wind speed region occurs, and a little pollutant spread is observed due to the structure of the main vortex inside the canyon. They also emphasized that pollutant exchange velocity is dominated by the turbulent component of the flux, up to three times the advective flux in some cases. Nevertheless, both advective and turbulent processes play important roles on removal pollutant capacity.

2.3 FLOW AND DISPERSION IN URBAN CANOPIES

Several studies were carried out to evaluate and predict the airflow and the pollutant dispersion over groups of buildings in order to understand the interaction of each isolated element within and above the canopy. Some authors based their studies on observational experiments by using wind tunnel simulations and field measurement campaigns (CARPENTIERI; HAYDEN; ROBINS, 2012; CHENG; CASTRO, 2002c; DAVIDSON et al., 1996). Other authors based their investigations on numerical simulations approaches using Reynolds averaged Navier-Stokes, large-eddy simulation and direct numerical simulation (CHENG; PORTÉ-AGEL, 2016; COCEAL et al., 2006; LIN et al., 2014).

Davidson et al. (1995, 1996) lead an experimental investigation based on wind tunnel and field scale measurements of a plume dispersion from a point source located upstream a group of cubic obstacles. They analysed the airflow and the gas dispersion through two obstacle arrangements: aligned and staggered. During the experiments, they observed a few important effects based on flow visualization and gas concentration measurements, such as high lateral

mixing due to the formation of horseshoe vortex, flow channeling throughout the obstacles under the influence of certain wind directions and vertical diffusion. Frontal collision causing updraft flow and building turbulent wakes were indicated to be responsible for vertical diffusion. Such effects demonstrate a high three-dimensionality of the flow due to the presence of rough elements (CHENG; CASTRO, 2002b).

A very important aspect to be highlighted is related to specific characteristics of near-field and far-field of pollutant dispersion in the presence of a group of buildings. Macdonald, Griffiths and Hall (1998) suggested that Gaussian plumes models are able to describe the spatial distribution of pollutant concentration with good agreement with experimental measurements for regions sufficiently far from the source. Nevertheless, the concentration field near the source is strongly dependent on the shape and arrangement of the buildings. Therefore, Gaussian plume models are not able to predict correctly the concentration near the source (COCEAL et al., 2014).

Mavroidis and Griffiths (2001) performed several experiments in a wind tunnel to assess the influence of different aspect ratios in the flow and dispersion of pollutants within an array of obstacles. They demonstrated that the aspect ratio of the obstacles directly influence the flow pattern and consequently the plume of contaminants in this region.

The wind direction is another influencing factor to alter the flow and dispersion patterns. Branford et al. (2011) performed a direct numerical simulation in order to evaluate the influence of three different wind directions (0° , 30° and 45°) on the dispersion of a passive scalar released from a point source located within a regular array of cubic buildings. The authors stressed the importance of street intersections on ventilation and pollutant dispersion over urban areas. They also concluded that the lateral plume width becomes larger for oblique wind direction, which agrees with the study of Garbero, Salizzoni and Soulhac (2010). Moreover, few relevant aspects were mentioned as channeling flow down the streets for the flow aligned with the streets, topological dispersion and secondary sources, when the flow becomes oblique presenting streamlines meandering the cubes.

Lin et al. (2014) investigated the turbulent airflow over various urban arrangements and building shapes with the same building area density. They conducted a detailed numerical study using RANS in order to demonstrate how wind direction influences the turbulent flow over a group of aligned and staggered uniform buildings. The analyses were carried out for seven different wind directions: 0° , 15° , 30° , 45° , 60° , 75° and 90° . As expected, smaller angles of the

wind direction provide better ventilation within both urban-type configurations. Moreover, the squared buildings array experienced more low wind zones compared to rectangular buildings arrays under most wind directions. The contours of the velocity under different wind directions and building arrangements can be seen in Figure 7.

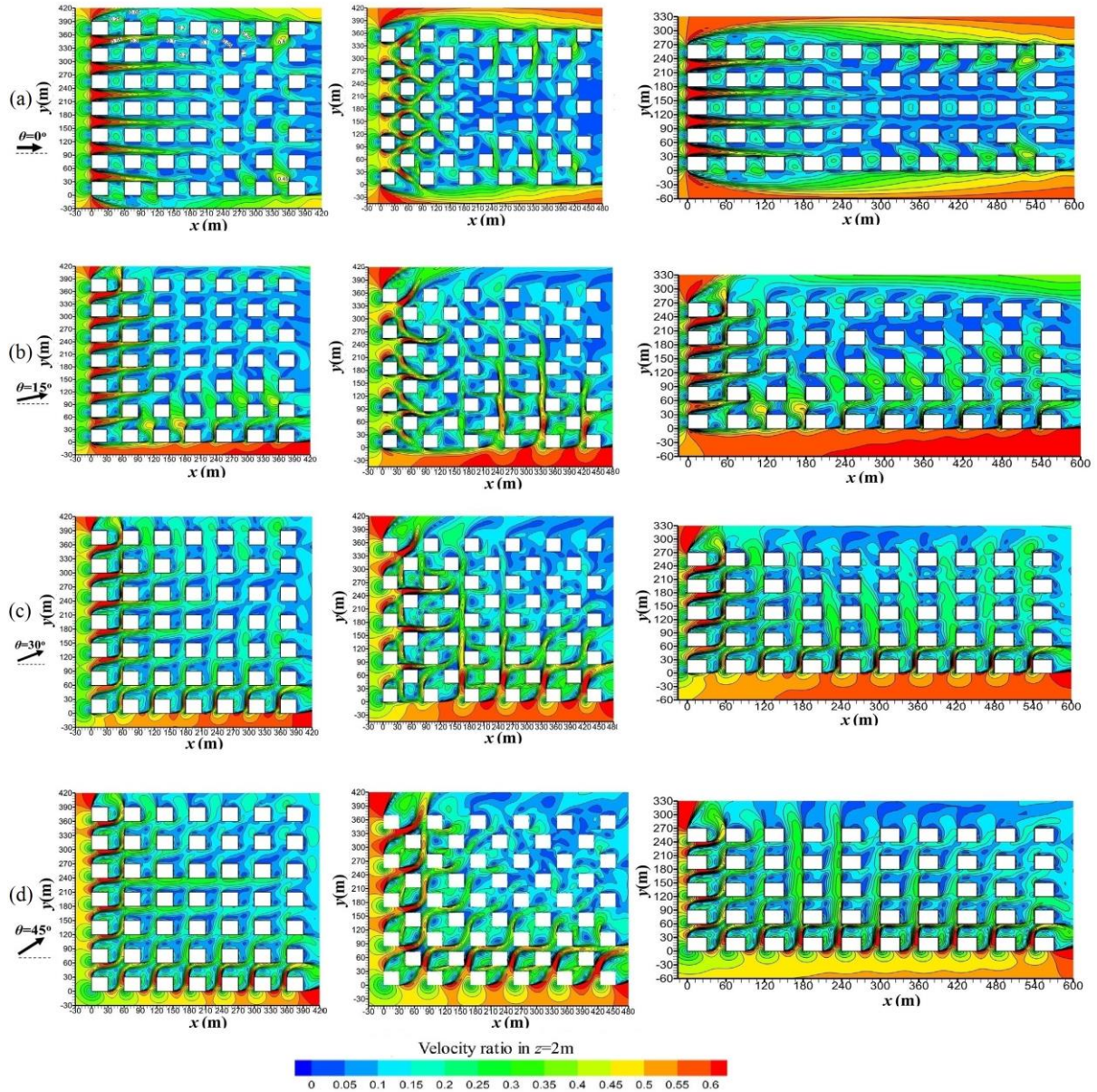


Figure 7. Contours of velocity at $z = 2m$ for various urban morphologies and wind directions: (a) 0° , (b) 15° , (c) 30° and (d) 45° . Adapted from Lin et al. (2014)

Goulart, Coceal and Belcher (2018) investigated the interaction between within and above the urban canopy, regarding scalar transport mechanisms using the same set of DNS data of Branford et al. (2011). The total scalar flux was partitioned into advective and turbulent components and was clear that the advective part of the horizontal pollutant mass flux plays the major role within the urban canopies. On the other hand, the vertical scalar flux at rooftop level

and above is predominantly turbulent and plays an important role on how the pollutant spreads around the buildings. The turbulent flux enhances the detrainment close to the source and promotes re-entrainment further away from the source.

As part of a large study on pollutant dispersion called DIPLOS project, Castro et al. (2017) presented experimental and computational results of turbulent flow over an aligned array of rectangular-shaped buildings. They evaluated three wind directions (0° , 45° and 90°). LES and DNS models were solved and compared with wind tunnel measurements. Numerical simulation data showed a vertical velocity profile expected for urban areas, presenting good agreement with the experimental work for all wind directions. The obstacles within the canopy present one longer dimension compared to conventional studies of cubic buildings arrays, and for that reason, it was possible to observe greater flow channeling for the direction aligned with the longer dimension. In addition, they concluded that LES could reproduce the flow field with excellent accordance compared to experimental and DNS data.

Mei et al. (2017) evaluated the effect of different frontal area densities (λ_F , the ratio of the frontal area (normal to the incident flow) to the lot area occupied by an individual obstacle) over a group of aligned buildings. They varied the λ_F by adding extra buildings and reducing the building height, always using the same domain size. Their RANS data were compared with experimental data and presented similar velocity profiles. They stated that the flow is strongly influenced by frontal area density, since different vortex structures is observed, varying the density, and suggested that lower values of λ_F promote better ventilation within the canopy.

Several works have focused on understanding the flow and dispersion patterns over uniform arrays with regular obstacles but other researchers are aiming at more complex and realistic urban sites in their studies. Therefore, different building heights, shapes and arrangements were considered in order to treat urban areas in a more realistic way. It is important to notice that even the slightest variation in buildings shapes promotes large variations on airflow and pollutant dispersion.

Xie, Coceal and Castro (2008) studied the flow over a staggered array of random heights buildings, aiming to extend the knowledge in respect of the randomness in the canopy topology. They used LES and their data were compared to Cheng and Castro (2002a) wind tunnel experimental data presenting good agreement, particularly near the ground surface. They also compared their data with LES and DNS data of flow over a staggered array of uniform cubes in order to investigate the effects of the random heights in maximum detail. As expected, the

authors highlighted the greater complexity of the flow compared to the uniform array. In addition, they suggested that the mean flow and turbulent kinetic energy are very peculiar around blocks with different heights and discussed the possibility of generalizing such approach.

Boppana, Xie and Castro (2010) investigated the transport mechanisms of a passive scalar emitted from an area source located on the ground. Two different sets of staggered buildings were evaluated, the first with uniform height buildings and the second with five different building heights distributed uniformly in repeating units. They used large-eddy simulation and their numerical data were compared with wind tunnel experiment (PASCHEKE; BARLOW; ROBINS, 2008). They observed that the concentration distribution is dependent on building heights arrangement and an evident variation of the plume pattern is observed for the two studied arrangements (Figure 8). The uniform array presents a roughly Gaussian plume approximation, especially in regions further from the area source, while the random arrangement does not portray similar behaviour. In addition, both configurations presented similar features like higher concentration zone behind the buildings and lower concentration zone in front of them. The results indicate higher turbulent intensity behind taller buildings, where greater recirculation zone is developed enhancing the vertical scalar flux in such regions.

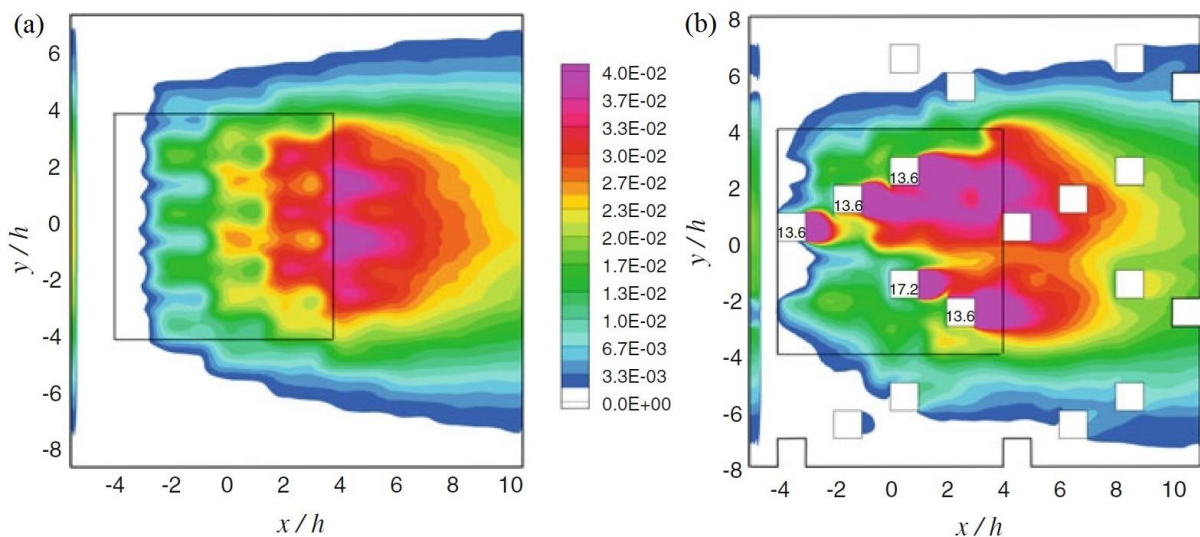


Figure 8. Contours of normalised concentration at $z/H_m = 1.20$ for (a) uniform height buildings array and (b) random height buildings array, where h is the average height of the buildings (BOPANA; XIE; CASTRO, 2010)

Zaki et al. (2011) performed wind tunnel experiments of two different urban canopies comprising buildings with random heights in a staggered composition. Their focus was to describe the flow characteristics based on the measured drag coefficient (C_d) and aerodynamic

parameters such as roughness length (z_o) and displacement height (d). They suggested that the skimming flow regime is not present within canopies with random buildings staggered distributed, due to the large gap between them. They also showed that the drag coefficient was dependent on the plan area density. In addition, they pointed out that the evaluation of aerodynamic parameters are relevant to better understand the airflow in urban areas.

Wind tunnel experiments and numerical simulation were carried out by Chen et al. (2017) in order to analyse the effects of building height variability on wind flow over an idealized urban arrangement. They used two RANS models to validate both uniform and random heights arrangements and presented fair vertical wind profile, especially within the canopy. The vertical turbulent exchange was proved to be enhanced in the regions next to taller buildings and to decrease in magnitude around smaller ones, when compared to uniform height case. Moreover, they concluded that compact urban layouts contribute to deteriorate city breathability, while lower density configurations have stronger vertical flux enhancing the ventilation.

Fuka et al. (2018) studied the same aligned rectangular buildings array used by Castro et al. (2017), but with an additional single centre-located tall building (three times taller). They conducted wind tunnel experiment and large-eddy simulation aiming to identify the influence of the discrepant element on airflow and pollutant dispersion emitted from a point source in the ground level. The vertical scalar flux was partitioned into the advective and turbulent component. It was found that close to taller building the advective motions are dominant, while the turbulent component plays the major role on the entire array of uniform height buildings. Moreover, the authors demonstrated that the presence of a taller building alters significantly the scalar flux over all studied domain, enhancing or reducing the vertical scalar transfer depending on the relative source position to the taller building.

Yoshida, Takemi and Horiguchi (2018) also used LES to investigate the effects of building height variability on turbulent flow over the actual city of Kyoto in Japan. The city was reproduced from a digital surface dataset. The numerical results were compared to LES results from Nakayama, Takemi and Nagai (2011). They also simulated the same urban site with a uniform height, taken as the average value of the real building heights, in order to analyse the effects of height randomness. It was very clear that tall buildings randomly distributed in the urban area strongly affect the flow above the canopy and are responsible for generating turbulent zones further from that element. Different values of λ_P from different real cities were

also evaluated and they concluded that $\lambda_P = 0.3$ can be considered a threshold in which the effects of building height variability become evident.

Carpentieri et al. (2018) measured the advective and turbulent flux over two building arrays using an experimental technique to measure both concentration and wind velocity in a wind tunnel experiment. The first array consisted of uniform building heights and the second with the presence of different building heights distributed along the arrangement. They concluded that the advective component of horizontal flux is dominant within the canopy for both oblique and perpendicular incident wind. Moreover, the advective and turbulent components have the same magnitude order in the building height. Another important finding is that the presence of smaller buildings slightly affects the vertical pollutant mass transport while the presence of a single taller building located at upstream flow alters that transport.

In this chapter, many aspects of the flow and dispersion over urban areas were covered. Several urban compositions were the focus of numbered investigations. However, certain issues still need to be further investigated as the building height variability on pollutant mass transfer mechanisms (advective and turbulent), which is still not completely explored.

3 METHODOLOGY

This chapter presents the tested case geometries in Section 3.1, sequenced by Section 3.2 that presents the conservation equations of the transport phenomena and turbulence treatment. Section 3.3 shows a brief description of numerical schemes used in this work, while Sections 3.4 presents the simulation statistics used in the simulations and the computation facility.

3.1 SIMULATED CASES

Three different building configurations were simulated. The first one is a staggered array with random height buildings – RBSA, the second is a staggered array with uniform height buildings – UBSA and the last one is an aligned array with random height buildings – RBAA. All simulated cases are presented in Figure 9.

The staggered configurations follows the same setup of the wind tunnel experiment performed by Pascheke, Barlow and Robins (2008). For the random building arrays, the building height distribution approximately follows a Gaussian distribution ranging from 2.8mm to 17.2mm, with five different heights in total. The mean height of the buildings is $H_m = 10\text{mm}$, the same height used for the buildings in the uniform case. For all geometries, the plan area density (λ_P , the ratio of the lot area occupied by the buildings per total domain area) is equal to 0.25 and the light blue zone coincide with the area source on ground level.

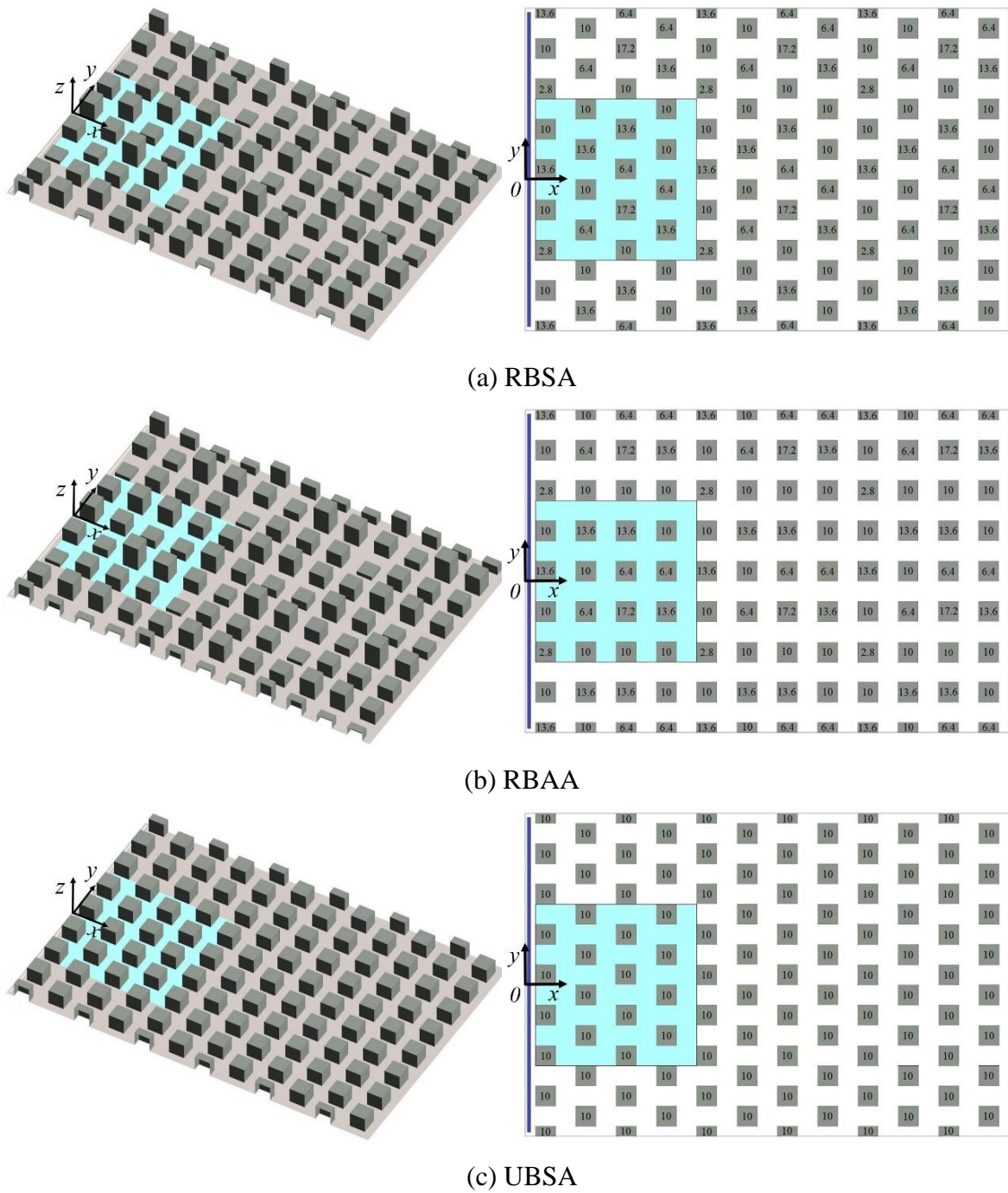


Figure 9. Plan view of different urban configurations: (a) staggered array with random buildings height (RBSA), (b) aligned array with random building height (RBAA) and (c) staggered array with uniform buildings height (UBSA).

The computational domain is of size $L_x \times L_y \times L_z = 24H_m \times 16H_m \times 10H_m$ for RBSA and RBAA configurations and $L_x \times L_y \times L_z = 24H_m \times 16H_m \times 6H_m$ for UBSA. According to Coceal et al. (2006), the dispersion will not be influenced by the top region of the domain for heights six times the building height and, for that reason, $6H_m$ was chosen for uniform cases and $10H_m$ for random cases, since the tallest element has 17.2mm in height.

3.2 MATHEMATICAL MODELLING

3.2.1 Governing Equations

The flow and pollutant dispersion on a neutrally stratified atmosphere are governed by the conservation equation of mass, *momentum* and chemical species. Considering fluid incompressibility condition, a Newtonian fluid can be described by the following equations:

$$\frac{\partial \rho}{\partial t} + \rho \frac{\partial u_i}{\partial x_i} = 0 \quad (1)$$

$$\rho \frac{\partial u_j}{\partial t} + \rho \frac{\partial u_i u_j}{\partial x_i} = -\frac{\partial p}{\partial x_j} + \frac{\partial}{\partial x_i} \left[\mu \left(\frac{\partial u_j}{\partial x_i} + \frac{\partial u_i}{\partial x_j} \right) \right] \quad (2)$$

$$\rho \frac{\partial c}{\partial t} + \rho \frac{\partial u_i c}{\partial x_i} = \rho \frac{\partial}{\partial x_i} \left(D_m \frac{\partial c}{\partial x_i} \right) + S \quad (3)$$

Where:

- ρ is the fluid density [kg/m³];
- t is the time [s];
- u_i is the velocity component in the direction i [m/s]
- x_i is the Cartesian coordinate in the direction i [m];
- p is the fluid static pressure [N/m²];
- μ is the fluid dynamic viscosity [Pa.s];
- D_m is the molecular diffusivity [m²/s];
- S is the source rate of the chemical specie [kg/m³.s];
- c is the chemical species concentration [kg/m³].

Although these equations are valid for laminar and turbulent flows, the presence of turbulence requires the use of very fine discretization grids (Δ_x , Δ_y and Δ_z) and time-steps (Δ_t) to capture all scales of the turbulent structures, due to the presence of a wide range of velocity fluctuations frequencies and the spatial complexity of such fluctuations. This approach is called Direct Numerical Simulation or DNS.

In this sense, DNS requires a very fine temporal and spatial discretization, from Kolmogorov microscales to larger motion scales according to the domain of interest. The approach is conceptually simple, but such discretization generates huge computational efforts, and the

computational power increases with Reynolds number. Therefore, its use is still limited to simplified geometries and flows with low Reynolds number.

Reynolds average Navier-Stokes (RANS) models are, in fact, turbulence models that use a statistical approach proposed by Reynolds (1985) to model the effects of turbulence unsteadiness on mean flow properties. The approach defines that all properties of the flow are decomposed by its mean value and the instantaneous fluctuation, so an extra term appears in the flow equations. These extra terms can be modelled with various turbulence models such as $k-\varepsilon$ or $k-\omega$. Therefore, RANS-based approaches greatly reduce the required computational effort and resources and such models has been widely adopted in practical engineering applications.

The third modelling approach is the Large-Eddy Simulation (LES) that is an intermediate approach between DNS and RANS. The approach is based on the self-similarity theory of Kolmogorov, which the large scales of the flow are more complex and mainly dependent on geometric characteristics, while small motion scales are self-similar and possess a universal aspect. Therefore, this approach calculates only the larger motion scales and do not resolves the small scales of turbulent flows. The small scales effects are modelled by using subgrid-scale (SGS) models. In other words, LES solves a filtered equation with an additional subgrid stress component, which accounts for the effect of smaller turbulent scales. In this dissertation, large-eddy simulations were performed using Smagorinsky-Lilly SGS model. Next, the LES theory and the final transport equation form are demonstrated.

3.2.1.1 Large-Eddy Simulation Equations

As briefly discussed previously, LES approach is based on the energy cascade and the Kolmogorov hypotheses, where the turbulence is introduced on the mean flow due to the production of kinetic energy from the larger scales of motion, while the smallest scales are isotropic, universal and less energetic named as Kolmogorov scales. Therefore, the equations that govern the fluid motions are obtained through a spatial filter that separates any flow variable into the sum of the resolved larger scales and the contribution of smaller scales, or subgrid-scales, that are modelled:

$$f(x_i, t) = \bar{f}(x_i, t) + f'(x_i, t), \text{ where } i = 1, 2, 3 \quad (4)$$

Where

- f is any flow variable
- \bar{f} is the resolved scale of any flow variable
- f' is the subgrid scale of any flow variable

The spatial filtering process is used to spatially limit the scales to be solved. The process can be mathematically represented in physical or Fourier space and its result is schematically demonstrated in Figure 10, where Δ is the cut-off length in physical space, k is the wavenumber and k_c is the cut-off wavenumber in Fourier space

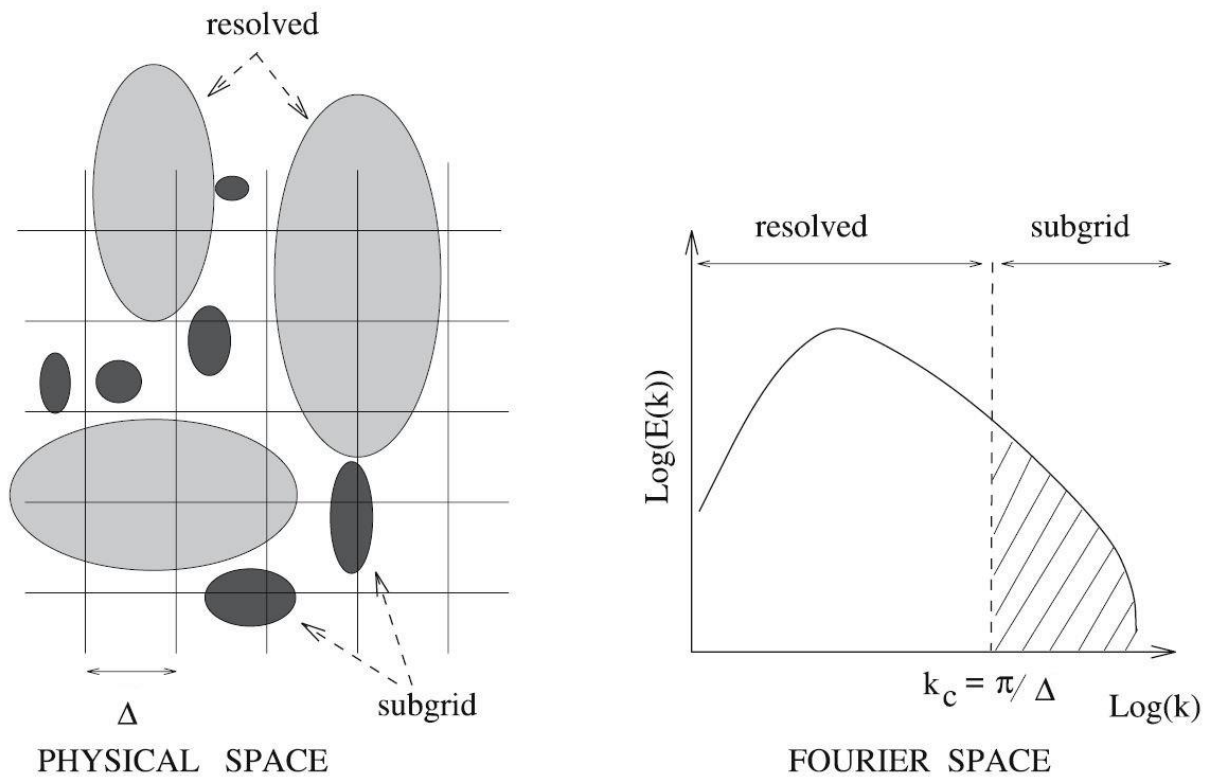


Figure 10. Representation of the resolved and subgrid scales after a sharp cut-off in physical and Fourier space (SAGAUT, 2006)

The representation of mathematical modelling of the filtering process in physical space is defined by a filter function (G) represented by the relation

$$\bar{f}(x_i, t) = \iiint_{-\infty}^{+\infty} G(x_i, x'_i, \Delta) f(x_i, t) dx_i \quad (5)$$

Note that the integration takes into account the three-dimensional space over the volume and indicates spatial averaging, not the time-averaging. Therefore, the overbar represents spatial

filtered variables and not time-averaged variables as imposed in RANS formulation. Three convolution filters are usually used for scale separation in LES: *box* or *top-hat* filter, *Gaussian* filter and *sharp cut-off* filter. In this dissertation, the *top-hat* filter is implicitly used since the commercial code Fluent employs the finite volume method. The *top-hat* filter function is defined in Equation 6. For further information about another spatial filter, the readers may consider reading Sagaut (2006).

$$G(x_i) = \begin{cases} \frac{1}{\Delta^3} & \text{if } |x_i| \leq \frac{\Delta}{2} \\ 0 & \text{otherwise} \end{cases} \quad (6)$$

where Δ is the filter cut-off length for each volume within the domain size. In theory, the cut-off length can be defined as any size, but in CFD computation each variable is contained within each grid cell and it is related to the grid size, so details from smaller sizes are lost. Therefore, the cut-off length for uniform grids ($\Delta_{x_1} = \Delta_{x_2} = \Delta_{x_3}$) is the grid size itself (defined in Equation 7).

$$\Delta = (\Delta_{x_1} \Delta_{x_2} \Delta_{x_3})^{1/3} \quad (7)$$

Thus, applying the *top-hat* filter, the filtered variable is reduced into a finite integration in a finite space:

$$\bar{f}(x_i, t) = \frac{1}{\Delta^3} \iiint_{-\Delta/2}^{\Delta/2} f(x_i, t) dx_i \quad (8)$$

After the filtering operation, the filtered equations of momentum may be rewritten as

$$\rho \frac{\partial \bar{u}_j}{\partial t} + \rho \frac{\partial \bar{u}_i \bar{u}_j}{\partial x_i} = - \frac{\partial \bar{p}}{\partial x_j} + \frac{\partial}{\partial x_i} \left[\mu \left(\frac{\partial \bar{u}_j}{\partial x_i} + \frac{\partial \bar{u}_i}{\partial x_j} \right) \right] \quad (9)$$

$$\rho \frac{\partial \bar{c}}{\partial t} + \rho \frac{\partial \bar{u}_i \bar{c}}{\partial x_i} = \rho \frac{\partial}{\partial x_i} \left[(\overline{D_m} + \overline{D_s}) \frac{\partial \bar{c}}{\partial x_i} \right] + \bar{S} \quad (10)$$

The filtered *momentum* equation presents a non-linear term in the form of a filtered product and the closure problem arises. In order to deal with the problem, some mathematical assumptions and manipulations (LEONARD, 1975) are carried out in order to rewrite the non-linear term, where $u_i = \bar{u}_i + u'_i$.

$$\overline{u_i u_j} = \overline{\overline{u_i} \overline{u_j}} + \overline{\overline{u_i} u_j'} + \overline{u_i' \overline{u_j}} + \overline{u_i' u_j'} \quad (11)$$

Unlikely the *momentum* transport equation, the filtered product $\overline{u_i u_j}$ is different from the product of filtered velocities $\overline{u_i} \overline{u_j}$. The difference between these products is commonly defined as *subgrid-scale (SGS) stress tensor* (SAGAUT, 2006) defined as

$$\tau_{ij} = \overline{u_i u_j} - \overline{u_i} \overline{u_j} \quad (12)$$

or

$$\tau_{ij} = \overline{\overline{u_i} \overline{u_j}} + \overline{\overline{u_i} u_j'} + \overline{u_i' \overline{u_j}} + \overline{u_i' u_j'} - \overline{u_i} \overline{u_j} \quad (13)$$

or

$$\tau_{ij} = L_{ij} + C_{ij} + R_{ij} = \overline{u_i u_j} - \overline{u_i} \overline{u_j} \quad (14)$$

where

$$L_{ij} = \overline{\overline{u_i} \overline{u_j}} - \overline{u_i} \overline{u_j} \quad (15)$$

$$C_{ij} = \overline{\overline{u_i} u_j'} + \overline{u_i' \overline{u_j}} \quad (16)$$

$$R_{ij} = \overline{u_i' u_j'} \quad (17)$$

The above-mentioned decomposition is called Leonard or triple decomposition since the *SGS stress tensor* contains three contribution groups. L_{ij} is the Leonard stress and represents the interaction among the resolved scales due to the filtering operation. The *cross-stress tensor* C_{ij} is related to the interaction between the resolved and subgrid scales and R_{ij} is the *SGS Reynolds stress tensor*, which reflects the effects of the subgrid eddies. Using the decomposition illustrated by Equation 12, we can rewrite the final filtered *momentum* and scalar transport equation as

$$\rho \frac{\partial \overline{u_j}}{\partial t} + \rho \frac{\partial \overline{u_i} \overline{u_j}}{\partial x_i} = - \frac{\partial \overline{p}}{\partial x_j} + \frac{\partial}{\partial x_i} \left[\mu \left(\frac{\partial \overline{u_j}}{\partial x_i} + \frac{\partial \overline{u_i}}{\partial x_j} \right) \right] + \frac{\partial}{\partial x_i} (\tau_{ij}) \quad (18)$$

$$\rho \frac{\partial \overline{c}}{\partial t} + \rho \frac{\partial \overline{u_i} \overline{c}}{\partial x_i} = \rho \frac{\partial}{\partial x_i} \left[(\overline{D_m} + \overline{D_s}) \frac{\partial \overline{c}}{\partial x_i} \right] + \overline{S} \quad (19)$$

where τ_{ij} is the *SGS stress tensor* and D_s is the *SGS turbulent diffusivity* defined as v_s/Sc_s , where v_s is the subgrid viscosity and Sc_s is the subgrid Schmidt number. The scalar equation does not present non-linear terms. Therefore, further decomposition becomes unnecessary.

3.2.1.1.1 Subgrid-Scale Modelling

In order to achieve the closure for *momentum* equation, a model for calculate the effects of smaller eddies in the form of *SGS stress tensor* is necessary. The most widely used SGS models are based on the concept of turbulent viscosity, which links the SGS stress with resolved-flow strain rates, according to Boussinesq assumption (POPE, 2000). Applying this analogy for incompressible flows, the *SGS stress tensor* becomes

$$\tau_{ij} = -2\mu_t \bar{S}_{ij} + \frac{1}{3} \delta_{ij} \tau_{kk} \quad (20)$$

$$\bar{S}_{ij} = \frac{1}{2} \left(\frac{\partial \bar{u}_j}{\partial x_i} + \frac{\partial \bar{u}_i}{\partial x_j} \right) \quad (21)$$

where μ_t is the turbulent viscosity that will be modelled and \bar{S}_{ij} is the local rate of strain of the resolved flow. The isotropic term τ_{kk} can be added to the filtered static pressure term or simply be neglected. In this work, such term is added to the filtered static pressure as a modified pressure \bar{P} and the momentum equation become as illustrated by Equation 23.

$$\bar{P} = \bar{p} - \frac{1}{3} \delta_{ij} \tau_{kk} \quad (22)$$

$$\rho \frac{\partial \bar{u}_i}{\partial t} + \rho \frac{\partial \bar{u}_i \bar{u}_j}{\partial x_j} = - \frac{\partial \bar{p}}{\partial x_i} + 2 \frac{\partial}{\partial x_i} [(\mu + \mu_t) \bar{S}_{ij}] \quad (23)$$

Therefore, the turbulent viscosity must be modelled in order to close the filtered equations, where the simplest model was proposed by Smagorinsky (1963), which are based on the local balance of energy production and dissipation of the small scales, with the following assumptions

$$\mu_t = \rho(C_s \Delta)^2 S$$

$$S = (2\bar{S}_{ij}\bar{S}_{ij})^{\frac{1}{2}} \quad (24)$$

$$\Delta = (\Delta_{x_1}\Delta_{x_2}\Delta_{x_3})^{1/3}$$

where C_s is the Smagorinsky constant, which varies according to the flow characteristics. For example, Zhiyin (2015) suggested that the value of 0.18 is suitable for homogeneous isotropic turbulence, while the value of 0.1 is more appropriated for flows in near-wall regions.

In this work, the Smagorinsky-Lilly SGS model is used. Differently from the original Smagorinsky SGS model, in the Smagorinsky-Lilly SGS model, the turbulent viscosity is modelled by

$$\mu_t = \rho(L_s)^2 S \quad (25)$$

where

$$L_s = \min(\kappa d, C_s \Delta) \quad (26)$$

where

- κ is the Von Kármán constant
- d is the distance to the closest wall
- L_s is the Smagorinsky length analogous to the Prandtl's mixing length associated with subgrid-scales

Note that this SGS model is a damping function (proposed by Lilly) that ensures a reduction of the turbulent viscosity to capture well the energy contained within the viscosity-affected layer in the near wall regions. In addition, the turbulent viscosity is always a positive value, demonstrating that the energy is always transferred from the filtered portions of motion until the residual portions of the flow (POPE, 2000).

The Smagorinsky constant, as already pointed out is dependent on the type of the flow, and consequently, a number of studies suggest distinct general optimal values. For example, the range of 0.17-0.21 suggested by Lilly (1966, 1967) and 0.19-0.24 suggested by Rogallo and Moin (1984). Nevertheless, numerical studies performed by Deardorff (1970) demonstrated that high values of C_s promote excessive damping near solid walls. In this work, the value of

C_s was 0.1, which is commonly used to simulate this type of flow (XIE; COCEAL; CASTRO, 2008).

3.2.2 Boundary Conditions

All CFD problems are based on solving differential equations, and for that reason, boundary conditions are essential for the solution. The three simulated cases have the same schematic domain as represented in Figure 11 for RBSA case, where the main boundaries are named as follows: inlet, outlet, two lateral sides, area source, bottom and buildings. The information that supplies the condition for each of these boundaries is commented in the following.

Stationary wall with no-slip and specified shear condition was considered. The no-slip condition is the appropriate condition for interfaces between moving fluids and stationary solid walls, where all velocity components are null, so that condition was imposed to bottom, area source and building faces. On the other hand, free shear condition was employed at the top, specifying zero shear stress for all components.

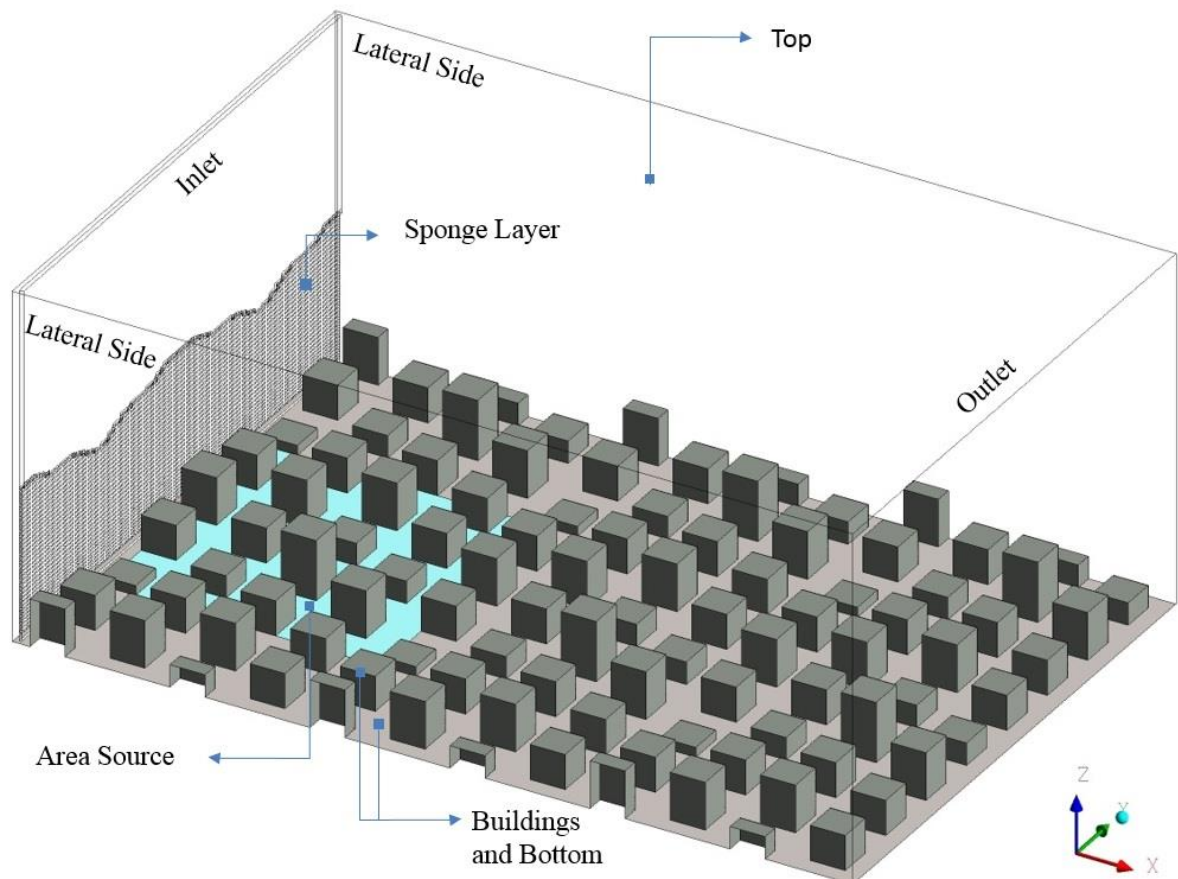


Figure 11. Three-dimensional sketch of RBSA case with the respective boundary conditions highlighted

It is important to notice that for translational periodicity, which is the case, is necessary to specify a driving force, which can be a constant pressure gradient or a net mass flow rate imposed on each cell of the domain (ANSYS, 2011). Therefore, in this work the flow is driven by a constant pressure gradient in the x -axis direction in all cases obtained from the relation

$$\frac{\partial \bar{p}}{\partial x_i} = \frac{-\rho u_\tau^2}{L_Z} \quad (27)$$

Where u_τ is the total wall friction velocity by definition and L_Z is the domain height. The friction velocity was based on the roughness Reynolds number Re_τ , defined in Table 1, according to Xie and Castro (2006) that performed LES simulations with the same random staggered domain.

Table 1. Characteristic parameters

Configuration	$Re_\tau = u_\tau H_m / \nu$	Friction velocity (u_τ)
RBSA	391	0.571
UBSA	304	0.442
RBAA	391	0.571

Regarding the concentration conditions, the area source was specified with a constant concentration equal to the saturation naphthalene concentration observed by Pascheke, Barlow and Robins (2008). On the other boundaries, the normal gradient of the concentration was set zero. Moreover, molecular diffusivity (D_m) is defined as ν / Sc_m , where Sc_m is the Schmidt number is set equal to 2.284, which is the same value used in the experimental simulation. Unlike of the flow field, it is not expected a periodic pattern for the concentration field and for that reason a region with zero concentration was specified near the inlet surface, here named sponge layer.

3.3 NUMERICAL METHODS

The numerical simulations were performed using the commercial software Ansys Fluent version 17.2, which employs the finite volume method (FVM) to discretize the conservation equations. The method consists of dividing the computational domain into finite control volumes (structured or unstructured) and integrating the conservation equations presented in Section 3.2.1 in every control volume.

3.3.1 The Finite Volume Method

The finite volume method was preceded by the finite element methods, assuming an important role in computational fluid dynamic applications. The method consists in integrate the governing equations over a finite volume.

Considering the unsteady convection-diffusion for a general variable of interest ϕ (velocity for *momentum* equation and concentration for scalar equation, for example), all transport equations can be written by the following general equation (MOUKALLED; MANGANI; DARWISH, 2016).

$$\underbrace{\frac{\partial(\rho\phi)}{\partial t}}_{\text{Transient Term}} + \underbrace{\frac{\partial(\rho u\phi)}{\partial x}}_{\text{Advective Term}} = \underbrace{\frac{\partial(\Gamma\nabla\phi)}{\partial x}}_{\text{Diffusion Term}} + \underbrace{S_\phi}_{\text{Source Term}} \quad (28)$$

Where

- ∇ is the gradient operator
- Γ is the characteristic diffusion coefficient

After the integration within a control volume, Equation 37 is transformed to Equation 38.

$$\int_{CV} \frac{\partial(\rho\phi)}{\partial t} dV + \int_{CV} \frac{\partial(\rho u\phi)}{\partial x} dV = \int_{CV} \frac{\partial(\Gamma\nabla\phi)}{\partial x} dV + \int_{CV} S_\phi dV \quad (29)$$

Where

- CV represents the control volume
- dV is the infinitesimal volume of the element

Gauss's divergence theorem is now used and, as a result, the volume integral is transformed into surface integrals over the bounding surfaces of the control volumes. So, applying such theorem, the volume integral of convection and diffusion terms are replaced by a surface integral and the Equation 38 may be written as

$$\int_{CV} \frac{\partial(\rho\phi)}{\partial t} dV + \int_A (\rho u\phi) \cdot \mathbf{n} dA = \int_A (\Gamma\nabla\phi) \cdot \mathbf{n} dA + \int_{CV} S_\phi dV \quad (30)$$

where

- A represents the surface area

- dA is the infinitesimal area of the element surface
- \mathbf{n} is the vector normal to surface element dA

In order to solve this integral, it is necessary to discretize the computation domain or, in other words, divide the domain into control volumes. The divided domain leads to a system of linear algebraic equations for each control volume

$$\frac{\partial(\rho\phi)}{\partial t} V + \sum_f^{N_{faces}} (\rho u \phi) A = \sum_f^{N_{faces}} (\Gamma \nabla \phi) A + S_\phi V \quad (31)$$

where

- N_{faces} is the number of faces enclosing the control volume
- $\frac{\partial(\rho\phi)}{\partial t} V$ is the transient term

Figure 12 shows a typical control volume, where the central grid point is denoted by the capital letter P and its neighbors as the capital letters W, E, D, B, N and S, as can be seen in Figure 12a. The scalar variables correspond to values at the nodal points, while vectors are defined at the surrounding surfaces.

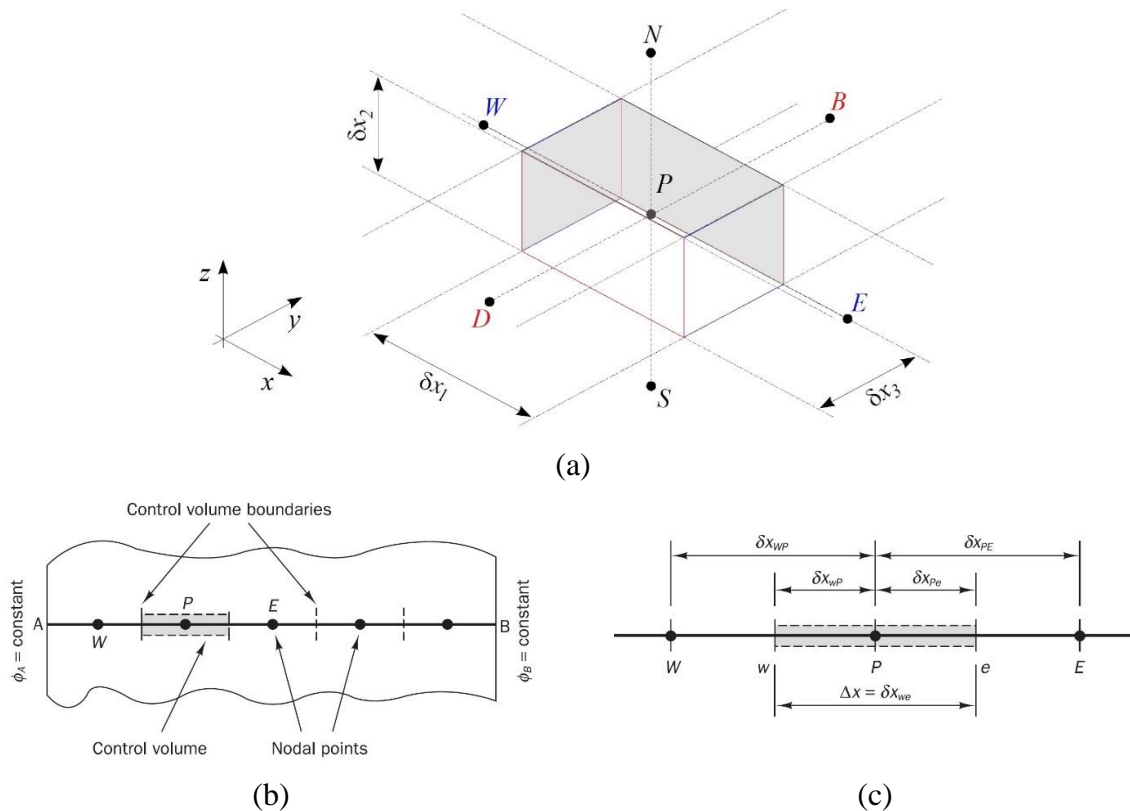


Figure 12. Typical (a) three-dimensional, (b) (c) one-dimensional schematic view for control volume discretization. Adapted from Versteeg and Malalasekera (2007)

For instance, we may consider the transport of the variable ϕ over a one-dimensional domain (x -axis) as presented in Figure 12b and c, where the value of ϕ are known at boundaries A and B. Therefore, after applying the Equation 40 to the control volume around the nodal point P, the discretized equation (excluding the transient term) becomes

$$(\rho u \phi A)_e - (\rho u \phi A)_w = (\Gamma \nabla \phi A)_e - (\Gamma \nabla \phi A)_w + S_\phi V \quad (32)$$

where

- e and w are the faces where the variable are evaluated
- $(\rho u \phi A)_e - (\rho u \phi A)_w$ is the advective term
- $(\Gamma \nabla \phi A)_e - (\Gamma \nabla \phi A)_w$ is the diffusion term

Assuming constant density (ρ) and surface area (A), is still necessary to determine the values of u , ϕ and $\nabla \phi$ for each surface. In order to solve the linear equation, an interpolation scheme is necessary to evaluate such variable variation over the control volume.

The set of linear equations generated by the discretization was solving by using least squares cell-based scheme for gradients, while the standard method was employed for pressure. The second-order implicit scheme was chosen to discretize the temporal term; the central differencing was used for *momentum* equation, while the third-order MUSCL was the choice for the scalar. Moreover, the SIMPLE algorithm was used to handle the pressure-velocity coupling. Table 2 presents each term with the respective scheme chosen in this work.

Table 2. Discretization methods used in the simulations

Term	Scheme
Gradient	Least squares cell-based
Pressure	Standard
Momentum	Central differencing
Scalar	Third-order MUSCL
Transient	Second-order implicit
Pressure-Velocity coupling	SIMPLE

3.3.2 Mesh Parameters

Xie and Castro (2006) indicated that a mesh containing 16 cells over each cube dimension was adequate to simulate the flow past a staggered cube array, while Boppana, Xie and Castro (2010) suggested that accurate computation of the scalar fluxes close to the surface requires a much finer grid resolution. Based on grid checks, these authors indicated that a vertical cell size of $H_m/64$ close to the surface was required. Therefore, a structured hexahedral mesh with eight million grid points were constructed with three mesh refinement regions as can be seen in Figure 13.

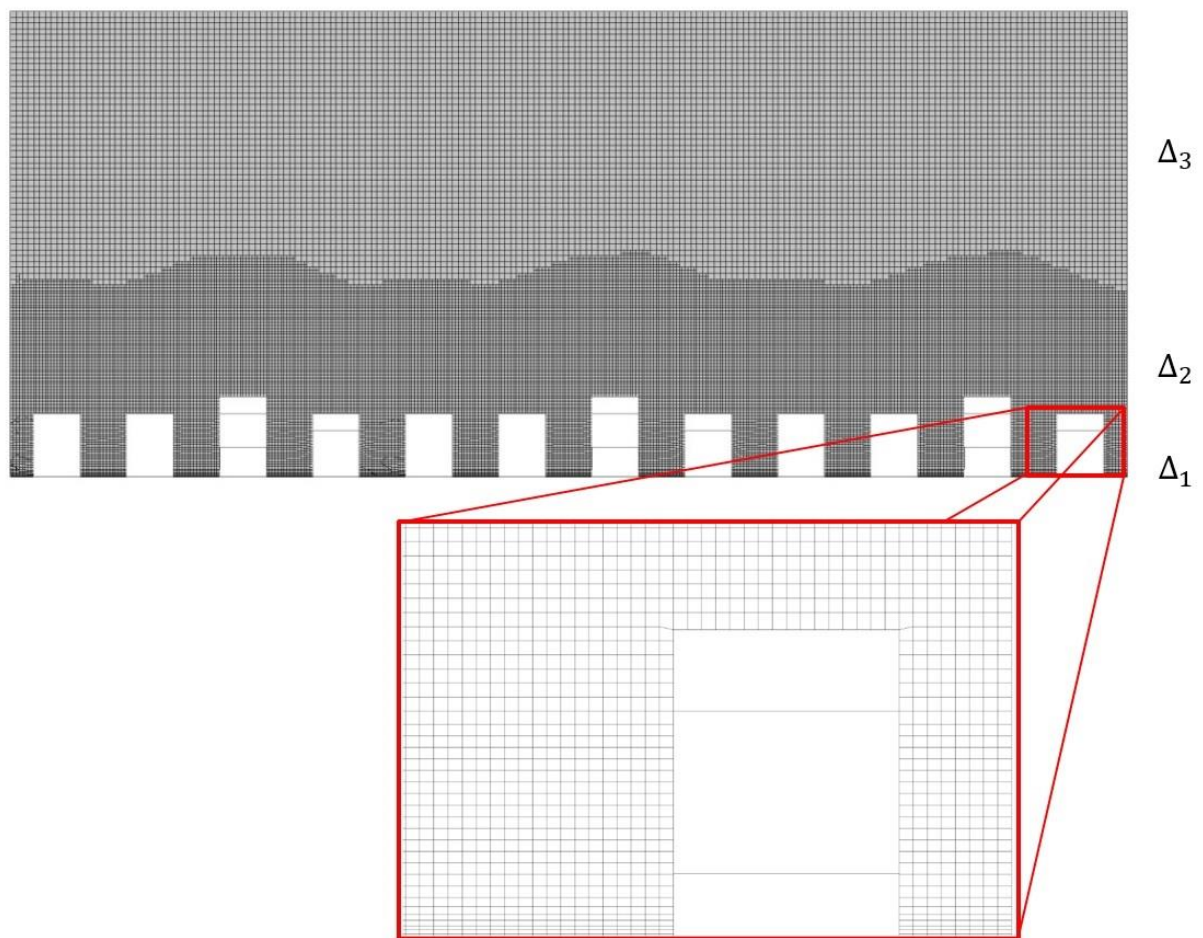


Figure 13. Cross section of the computational mesh showing three refinement levels for RBSA array. The inflation zone near the ground is also highlighted. The value of the vertical spacing, $\Delta_n = 1, 2, 3$ are mentioned in the text

In the first region Δ_1 , a vertical cell size of $H_m/75$ resolution close to the surface was used, gradually expanding to the second region Δ_2 , which reaches $z/H_m < 5$, with a constant grid size of $H_m/16$ in both x, y and z directions. In the third region, there was a step jump in mesh size, above $z/H_m = 5$, a uniform $\Delta_3 = H_m/8$ was used for all directions. The discontinuity in mesh size was not thought to be significant and was constructed in order to reduce computational cost

since the main interest of this work is the prediction of the transport mechanism inside the building canopy.

3.4 STATISTICS AND COMPUTATIONAL FACILITY

The simulations with the pressure driven turbulent inflow started from a statistically steady solution generated with a steady converged data. A constant time-step $\Delta_t = 0.002T_c$ was used, where $T_c = H_m/u_\tau$ is an eddy turnover time. All the simulations were run for at least $200T_c$ before statistics were computed, which was sufficient to assure the development of the flow. Then, the statistics were collected and averaged for a duration of $200T_c$ at each time-step resulting in converged results.

All simulations have been performed by a Linux powered cluster system named VULCANO-2 owned by the *Air Quality Research Center* (NQualiAr) of Federal University of Espírito Santo. Each computing node is equipped with Intel Core i7-4790K processor 4.0 GHz, 16GB memory, 4 cores and 8MB cache. Each run used 18 computing nodes requiring about six weeks to obtain satisfactory time-averaged results.

4 RESULTS

The focus of the present dissertation is the attempt to best describe the effects of different building heights and arrangements on pollutant fluxes within and above the urban canopy. Therefore, the results are divided into four parts. Section 4.1 presents a comparison with experimental data obtained from wind tunnel and LES simulation, in order to validate the employed model. Section 4.2 describes the characteristics of the flow field, while Section 4.3 describes the characteristics of the concentration field. Section 4.4 aims to analyse the pollutant mass transport and determine how urban topology (urban height and arrangements) affects horizontal and vertical turbulent fluxes inside the canopy.

The data presented throughout the entire chapter is the temporal average of the variables, according with the following equations.

$$\bar{u} = \frac{1}{T} \int_T u dt$$

$$\bar{w} = \frac{1}{T} \int_T w dt$$

$$\bar{c} = \frac{1}{T} \int_T c dt$$

Where T is the total averaging time of the simulation, \bar{u} is the time-averaged streamwise velocity, \bar{w} is the time-averaged vertical velocity and \bar{c} is the time-averaged concentration.

4.1 COMPARISON WITH A WIND TUNNEL EXPERIMENT AND LES SIMULATION

Numerical simulations are extensively used to investigate the complex airflow through a group of obstacles. In spite of many advantages, the accuracy and reliability of the turbulence models

are not always guaranteed, since numerical models are sensitive to the input data. The same need is expected for large-eddy simulation. Thereby, a validation investigation comparing numerical data with experimental measurements is essential (CHEN; SREBRIC, 2002).

Figure 14 presents the spatial average¹ of the mean streamwise velocity ($u^* = \langle \bar{u} \rangle / u_\tau$) profiles for RBSA and UBSA configuration. This figure shows a comparison between the results obtained in the present work, wind tunnel data acquired by Cheng and Castro (2002a) and other salient LES results obtained by Boppana and Xie and Castro (2010). Note that there are no experimental data for the comparison of these variables in the UBSA array. The data are normalised by the respective friction velocity (u_τ) presented in Table 1.

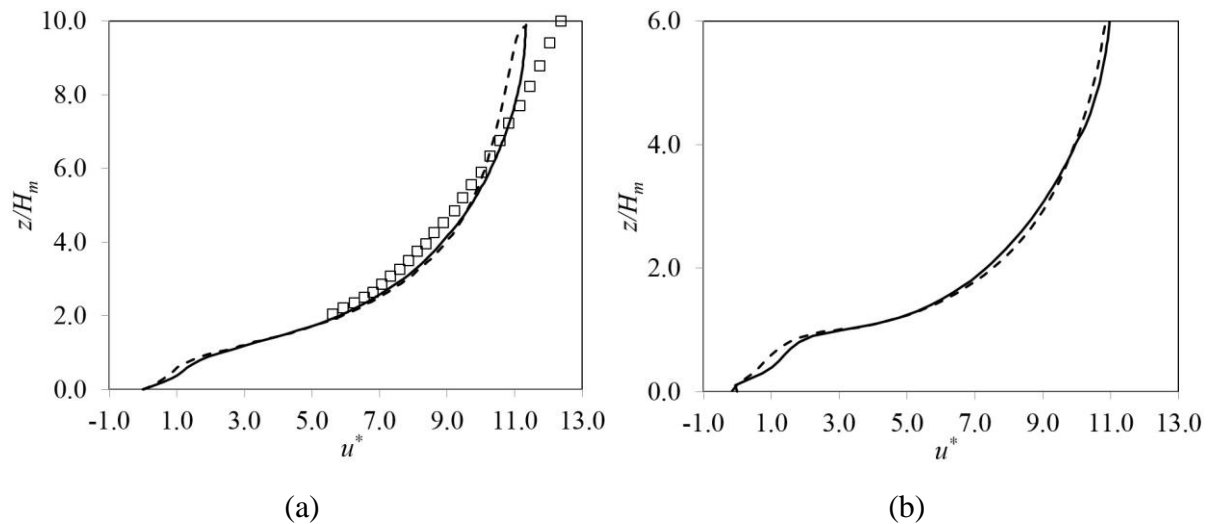


Figure 14. Profiles of the spatial average of the mean streamwise velocity (a) for RBSA and (b) for UBSA. Square symbols represent Cheng and Castro (2002a) experimental data, broken lines represent LES results produced by Boppana, Xie and Castro (2010) and solid lines represent the present work

Both LES results presented similar streamwise velocity profiles for RBSA and UBSA configurations. Nonetheless, the simulation underestimated velocities above $z/H_m = 7.0$ when compared with experimental data for the RBSA configuration (Figure 14a). The same result was found by Xie, Coceal and Castro (2008). However, this is not essentially significant for the flow at the roughness sublayer, since the flow is poorly dependent on the domain height, in this layer (COCEAL et al. 2006).

The lateral and vertical concentration profiles are presented for RBSA and UBSA configurations in Figure 16 and Figure 17, respectively. The concentration is presented in the dimensionless form to enable comparison with the experimental data by Pascheke, Barlow and

¹ The averaging process was done with 256 profiles within the domain.

Robins (2008) as $c^* = \bar{c}/c_0$, where c_0 is the constant concentration imposed at the area source. The locations of the measured profiles are evidenced in Figure 15, where dotted lines represent the lateral profiles and black dots represent the vertical ones.

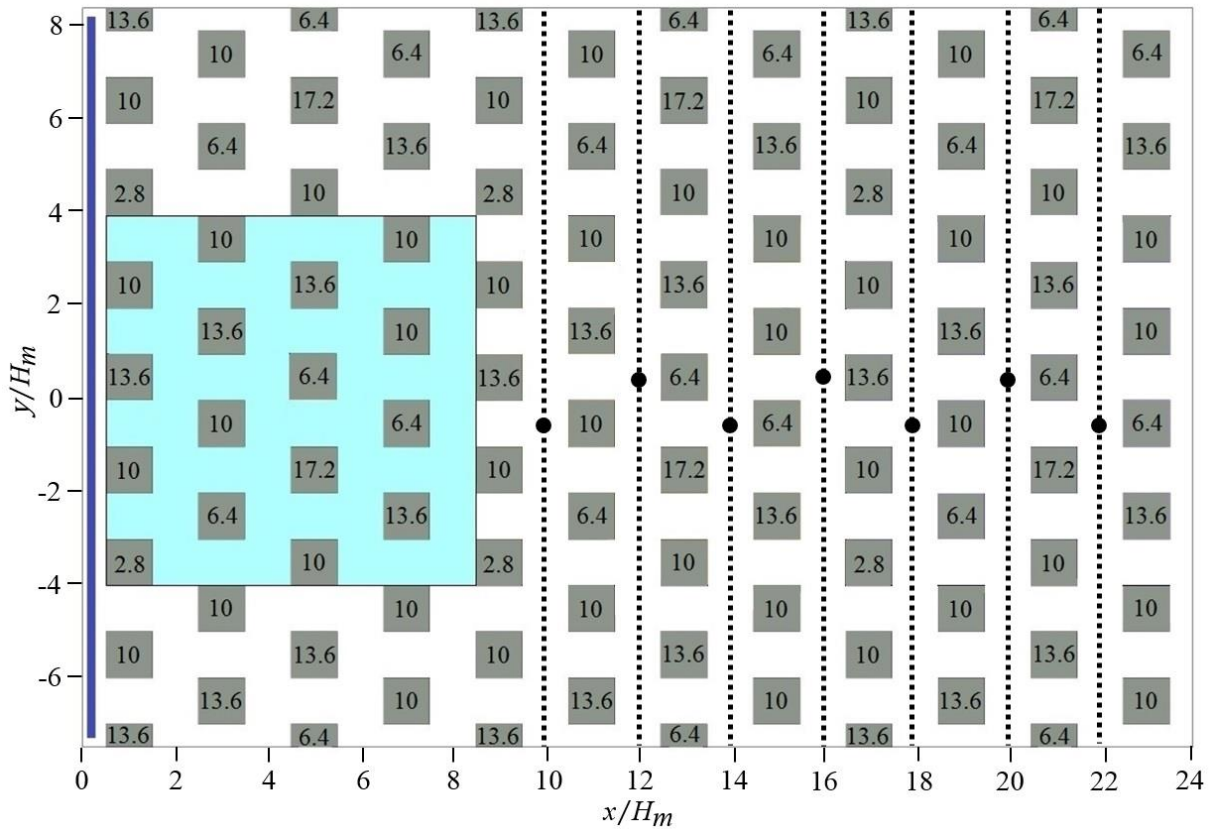


Figure 15. Plan view of RBSA configuration. Black dots indicate the locations of the vertical concentration profiles and dotted lines indicate the locations of the lateral profiles

Lateral concentration profiles are plotted in Figure 16 at $z/H_m = 0.6$. Figure 16a and Figure 16b show lateral concentration profiles in the regions near the area source, and Figure 16c and Figure 16d illustrate profiles further away from the area source. For both configurations, the concentration decreases with distance from the source, as expected. However, the RBSA configuration presents smaller concentration peaks, demonstrating larger vertical dispersion when compared with UBSA configuration. Therefore, the concentration decreases more rapidly with distance for the random array probably due to the presence of taller buildings within the domain.

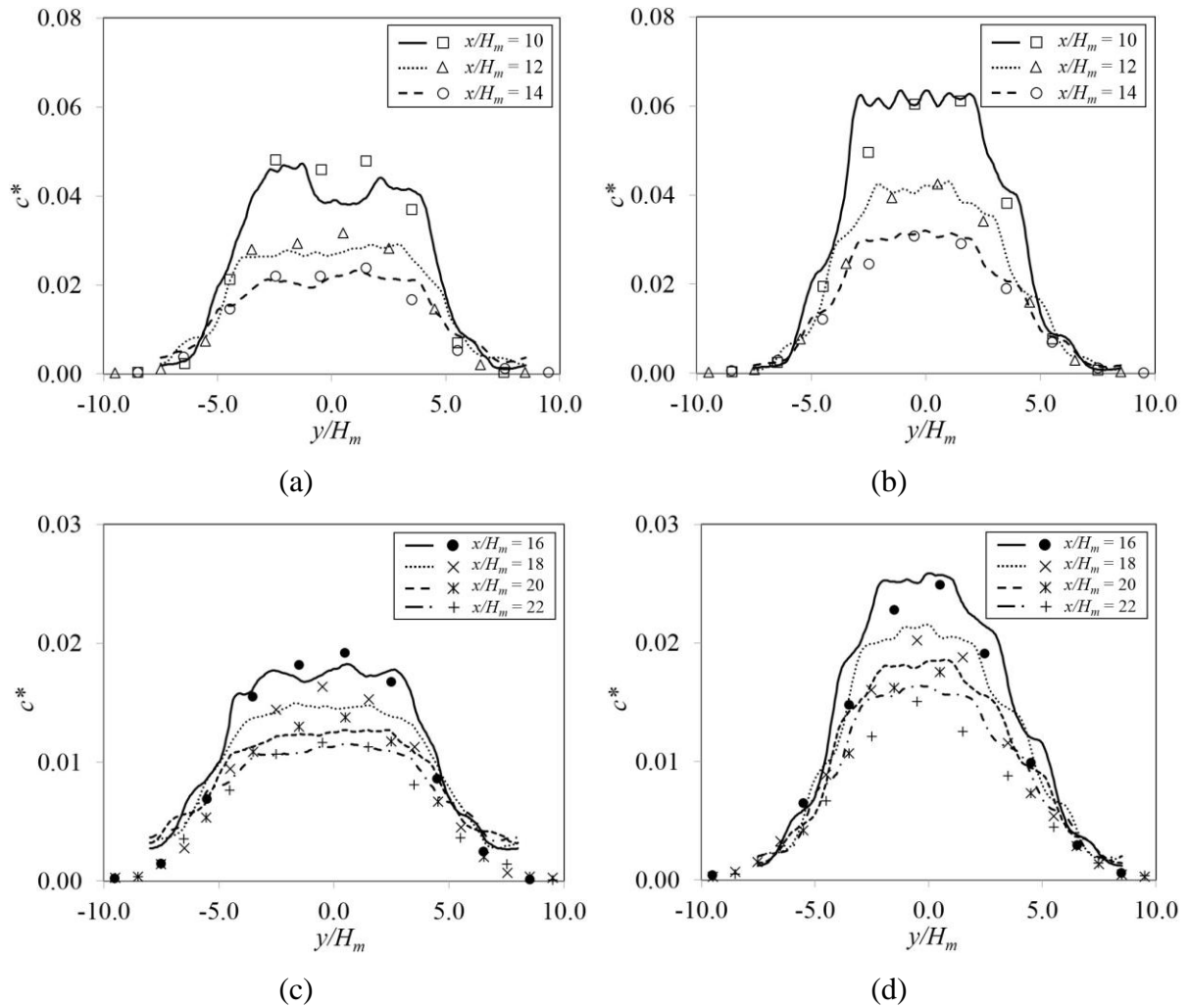


Figure 16. Lateral concentration profiles (a) near and (c) away from the source for RBSA and (b) near and (d) away from the source for UBSA configuration calculated at $z/H_m = 0.6$. Lines represent the present results and symbols indicate wind tunnel data

Near the source, the effect of taller buildings is more evident, modifying the lateral concentration profiles. For the RBSA configuration, the lateral profile demonstrated in Figure 16a resembles a double-peak Gaussian profile. The first peak is just above the building with $1.36H_m$ in height at $y/H_m = 1.5$ in the second row of buildings, while the second peak appears above the building with $1.72H_m$ at $y/H_m = -1.5$ in the third row (Figure 16a). This suggest stronger vertical motions behind taller buildings, since the uniform height array does not present the double-peak aspect (Figure 16b). In addition, Figure 16c and Figure 16d demonstrate that the concentration profiled becomes more uniformly distributed with distance from the source for both configurations, as also observed by Macdonald, Griffiths and Hall (1998).

Figure 17 shows the vertical concentration profiles near the area source and further away from the area source for RBSA and UBSA. The vertical concentration gradient is steeper closer to

the area source for all configurations. However, for the UBSA this gradient is even steeper than for the RBSA configuration (Figure 17a and Figure 17b). The profiles support the evidence of more efficient vertical dispersion due to the presence of taller buildings, since smaller concentration is observed within the urban canopy for RBSA configuration away the area source (Figure 17a). Branford et al. (2011) performed direct numerical simulation of the flow and dispersion and found little vertical pollutant exchange for cases in which wind direction is parallel to a uniform staggered array. Therefore, tall buildings enhance the vertical scalar exchange. This is also supported by Fuka et al. (2018). Note also that the differences in domain heights for UBSA and RBSA configurations does not significantly affect the concentration comparisons because the scalar does not reach $z = 6H_m$ (Figure 17a and Figure 17b).

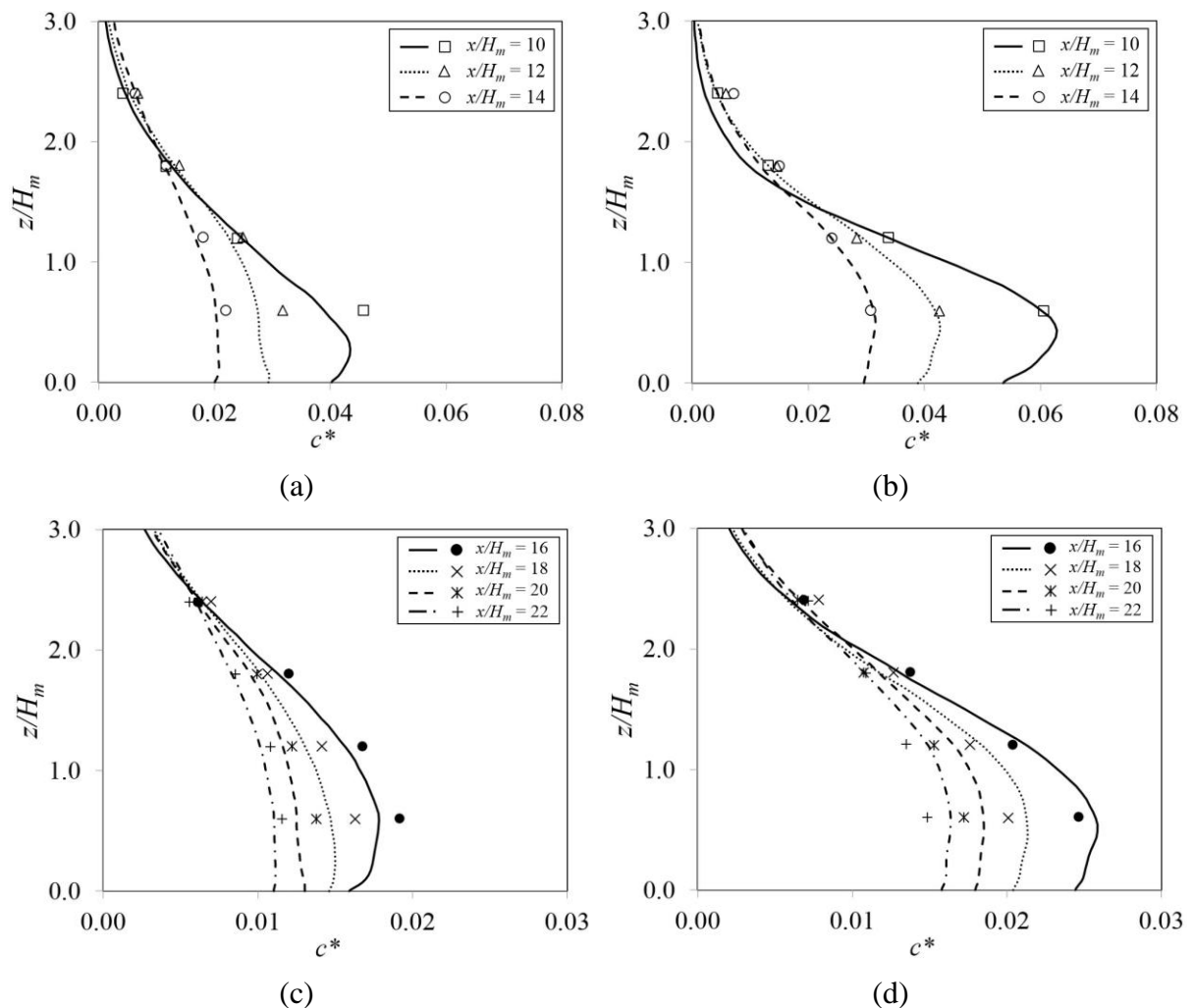


Figure 17. Vertical concentration profiles (a) near and (c) away from the source for RBSA and (b) near and (d) away from the source for UBSA configuration. Lines represent the present results and symbols indicate wind tunnel data

4.2 FLOW FIELD

This section describes the characteristics of the flow field for the urban configurations presented in Section 3.1. The analyses are made at different heights in an attempt to better describe the effects on flow pattern due to the presence of buildings with different heights and arrangements.

Figure 18 presents the streamlines of time-averaged velocity for UBSA, RBSA and RBAA configurations at $z/H_m = 0.28$ and $z/H_m = 1.00$. The complexity of the flow field is definitely clear for the array with random height buildings, while the UBSA configuration presents more uniform features. For the uniform array, approximately the same behaviour is observed around all the buildings. For example, the flow is divided in front of the building and it is channelled between two buildings at $z/H_m = 0.28$ (Figure 18a). In addition, recirculation regions are evident behind the buildings for both configurations at the same height (Figure 18b), but the pattern differs significantly.

The flow dynamics for RBSA configuration is much more complex than for UBSA, but some features are clearly noticeable. For example, Figure 18b shows that no evident recirculation appears behind the shorter buildings with $z = 0.28H_m$ and $z = 0.64H_m$, while it appears to be more intensified behind taller buildings. It is also observed recirculation in the region between specific buildings, for example the region between the building with $z/H_m = 0.28$ and $z/H_m = 1.00$. In addition, the perturbations are weakened with height and recirculation regions are observed locally behind taller buildings at $z/H_m = 1.00$ for the RBSA configurations (Figure 18e). This demonstrates weak interference of shorter buildings on the mean flow. At the same height, the mean flow is slightly disturbed due to the presence of the buildings for UBSA configuration (Figure 18d).

It is important to note that the recirculation pattern behind the buildings depends not only on the building height, but also on the building vicinity. For example, a 13.6mm building presents different recirculation pattern if it is close to a 17.2mm or a 10.0mm building.

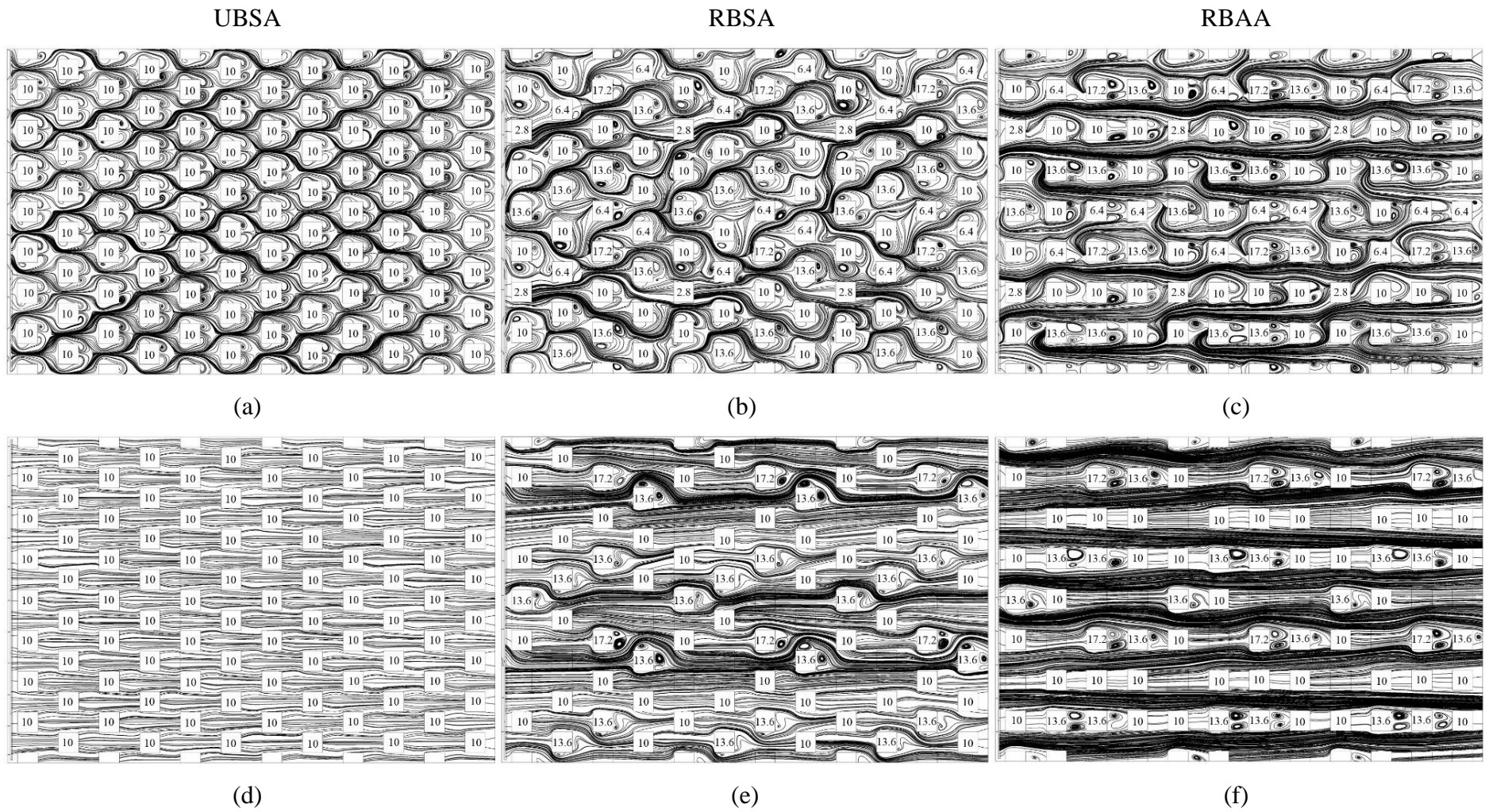


Figure 18. Horizontal plan view of streamlines of time-averaged flow field at (a) $z/H_m = 0.28$ and (d) $z/H_m = 1.00$ for UBSA, (b) $z/H_m = 0.28$ and (e) $z/H_m = 1.00$ for RBSA, (c) $z/H_m = 0.28$ and (f) $z/H_m = 1.00$ for RBAA

For RBAA configuration, the flow is primarily channeled along the main streets, as expected, while recirculation zones appear behind the buildings (Figure 18c and Figure 18f). Lin et al. (2014) studied the flow over several aligned arrays with regular buildings and presented similar characteristics. However, they observed that the recirculation zone behind the buildings is uniform, since the buildings have the same height. Figure 18f also demonstrates that the perturbations are weakened with height and recirculation appears locally behind taller buildings ($1.36H_m$ and $1.72H_m$), supporting the idea of weak interference of shorter buildings on the mean flow. It can be noted that even at z/H_m above the smaller buildings, the channelling effect still persists, as taller buildings still affect the flow.

Figure 19a shows the time-averaged velocity vectors of the flow field in the vertical $x - z$ plane for UBSA configuration. The flow regime over the uniform array has some similarities with the flow structure described by Oke (1988) as an isolated roughness flow. Some characteristic features are observed as an updraft motion in the back face and a strong downdraft flow in the frontal face of the building developing a recirculation zone next to the ground.

In fact, the presence of the downwind building still disturbs the wake region of the upwind building. Additionally, the presence of the upwind building disturbs the flow in the windward face of the downwind building. This fact can be clearly observed by the presence of always-negative streamwise velocity component close to the surface between buildings. The flow around an isolated building the recirculation is around $2H_m$.

It is interesting to note the updrafts and downdrafts in the instantaneous velocity vector between buildings (Figure 19b and Figure 19c). These vertical turbulent motions are responsible for the vertical turbulent flux of pollutants leaving/entering the urban.

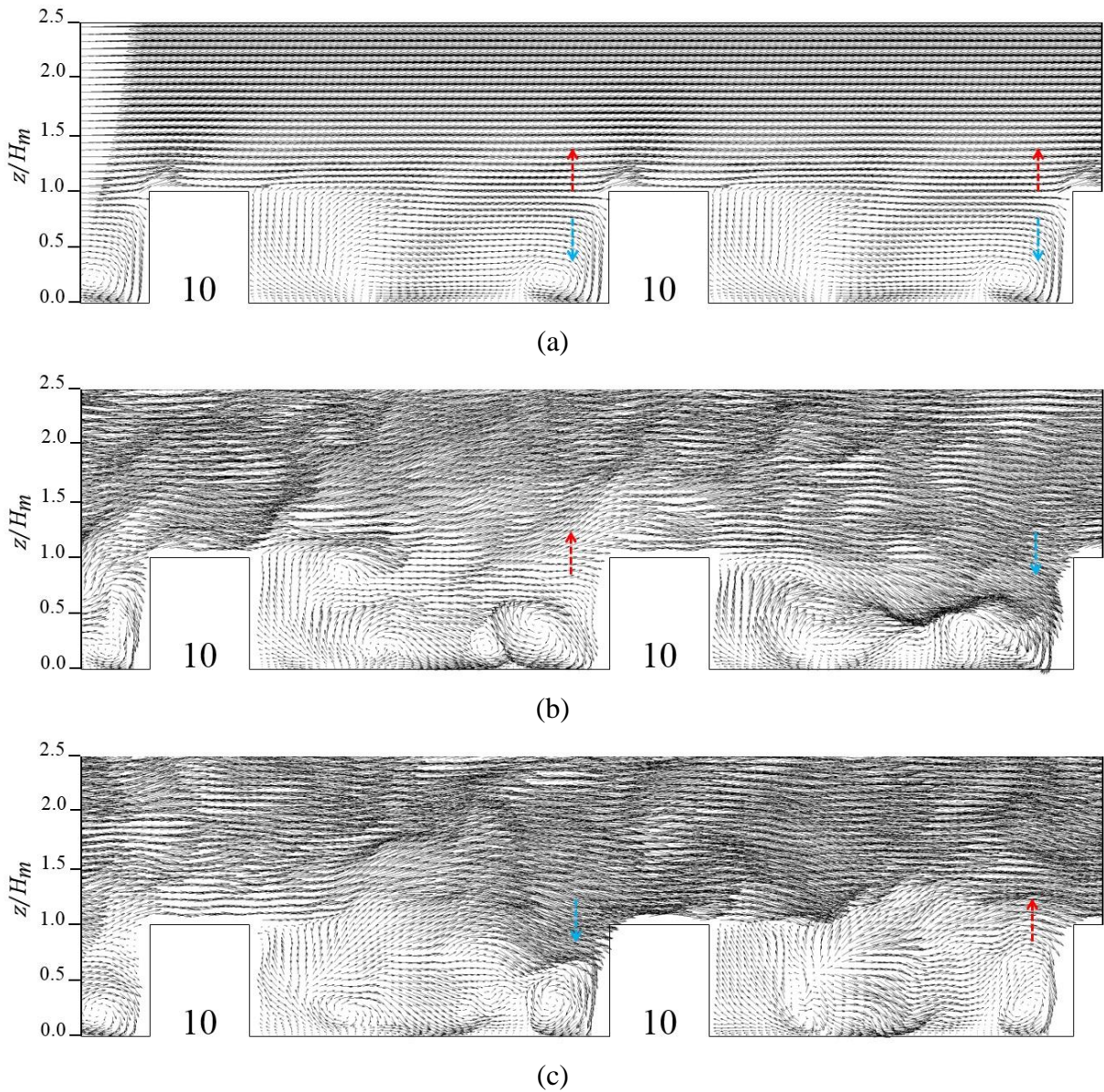


Figure 19. Time-averaged velocity vectors in the $x-z$ plane located at (a) $y/H_m = -1.5$ for UBSA. Instantaneous velocity vectors in the $x-z$ plane at $y/H_m = 0.5$ (b) above the area source and (c) further away from the area source for UBSA. Arrows indicate the direction of the flow and numbers indicate the building height in millimetres

In order to analyse the effect of different building heights, it is possible to divide the pattern of mean velocity field in three different groups. The groups have (a) at least one building lower than the average height, (b) at least one building taller than the average height and (c) one building taller and one lower than the average height. Figure 20 demonstrates the groups of buildings for RBSA configuration.

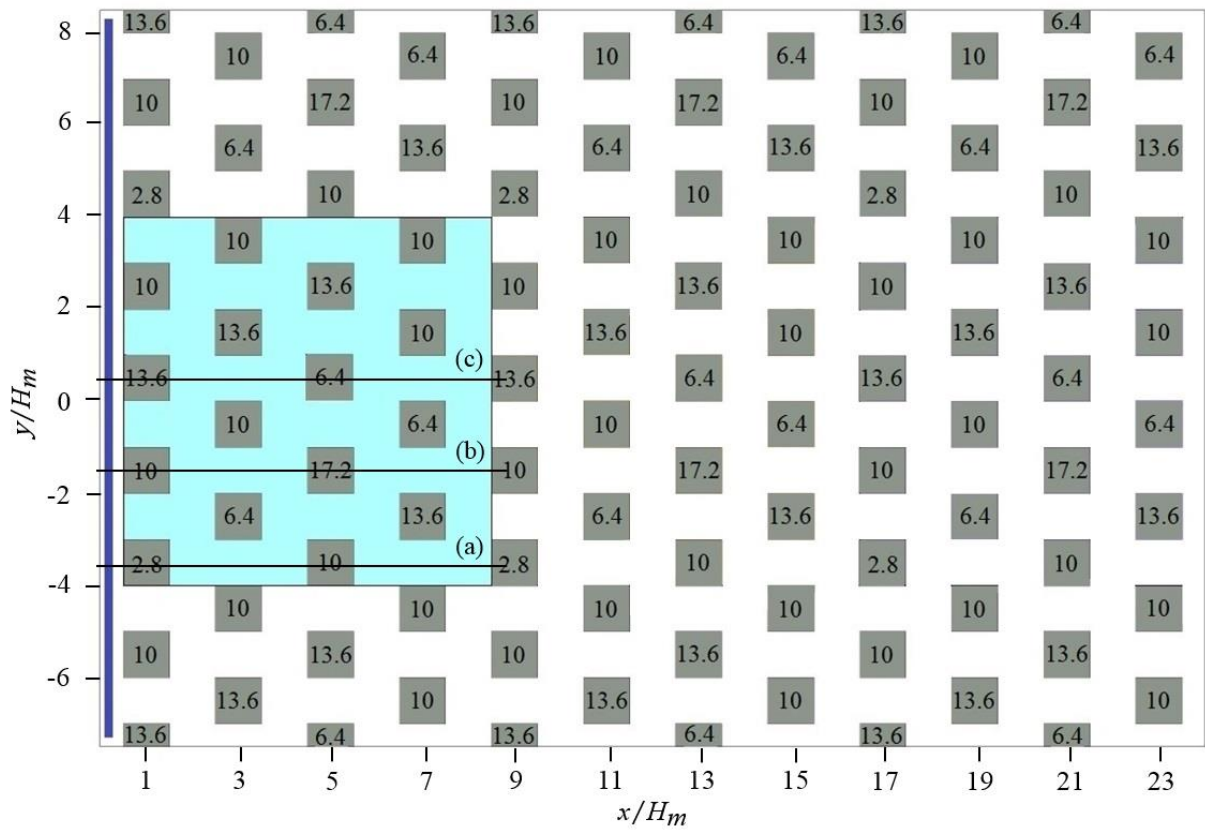


Figure 20. Plan view with indications for the group of buildings with (a) at least one building lower than the average height, (b) at least one building taller than the average height and (c) one building taller and one lower than the average height for RBSA

Figure 21 shows the time-averaged velocity vectors in the vertical $x - z$ plane for RBSA. Considering the average height of the buildings, the aspect ratio is the same as the uniform array (0.33) and Oke's classification suggests isolated roughness flow for the random buildings configuration. The flow indeed presents such characteristics but some features presents slight modifications due to the different building heights.

If the incoming flow passes over a smaller building (Figure 21a – case a), the updraft motion that appear at the back face is limited by its height ($z/H_m = 0.28$), while the recirculation region in front of the average building ($1H_m$) is diminished, since the flow passes freely above the smaller building. Moreover, a small vortex is also observed in front of the building with $0.28H_m$ high.

Figure 21b demonstrates the case (b), where the incoming flow passes over an average and a taller building. It is noticeable that the recirculation zone is enhanced in front of the taller building due to the stronger downdrafts. The separation zone at the upper half in front of the building becomes more evident and the flow reattachment at the rooftop occurs close to the

downwind edge. Figure 21c presents the case (c), where the flow passes over buildings that are taller and smaller than the average height (case c). The analysis of this figure with the Figure 19 demonstrate a clear pattern around smaller and taller buildings (compared to the average building height). Tall buildings produce downward flow in front of them, while small buildings generate upward flow in the same region. In this sense, the former is responsible for the entrainment of “cleaner” air into the canopy, while the latter cause the detrainment of polluted air from the canopy.

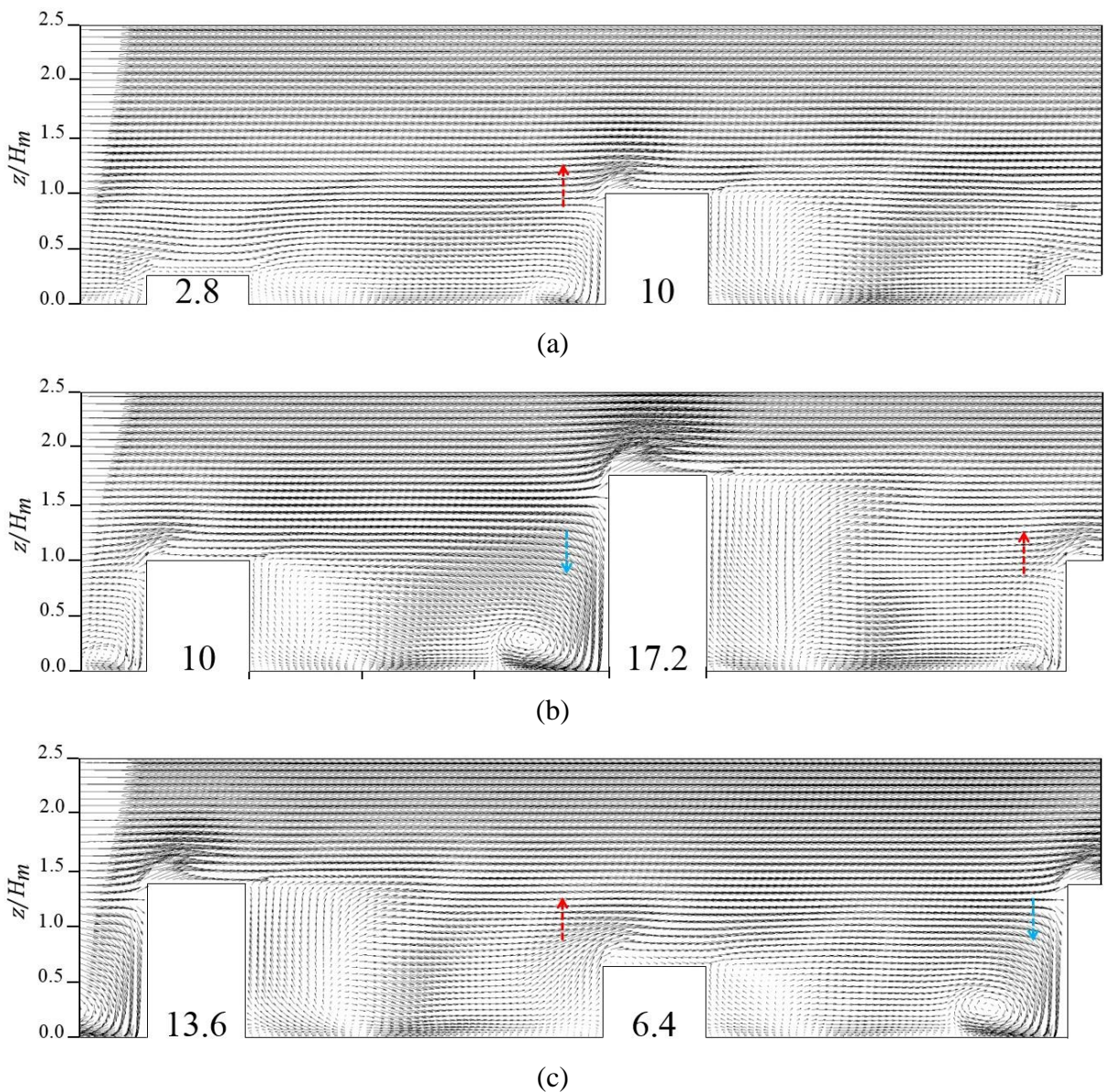


Figure 21. Time-averaged velocity vectors in the $x-z$ plane located at (a) $y/H_m = -3.5$, (b) $y/H_m = -1.5$ and (c) $y/H_m = 0.5$ for RBSA. Arrows indicate the direction of the flow and numbers indicate the building height in millimetres

The same groups of buildings presented for RBSA array are demonstrated in Figure 22 for the aligned configuration. Unlike observed in the RBSA, the aligned configuration has the same

flow structure as that described by Oke (1988) as skimming flow, since the aspect ratio is equal to the unit (considering the average height). Therefore, a stable vortex is expected in the space between the buildings if an array with uniform building height were considered (AI; MAK, 2017; DI BERNARDINO et al., 2018). However, the building height variability presented in the RBAA configuration considerably changes the flow pattern, depending on the sequence of buildings. Figure 22 demonstrates the groups of buildings for RBAA configuration.

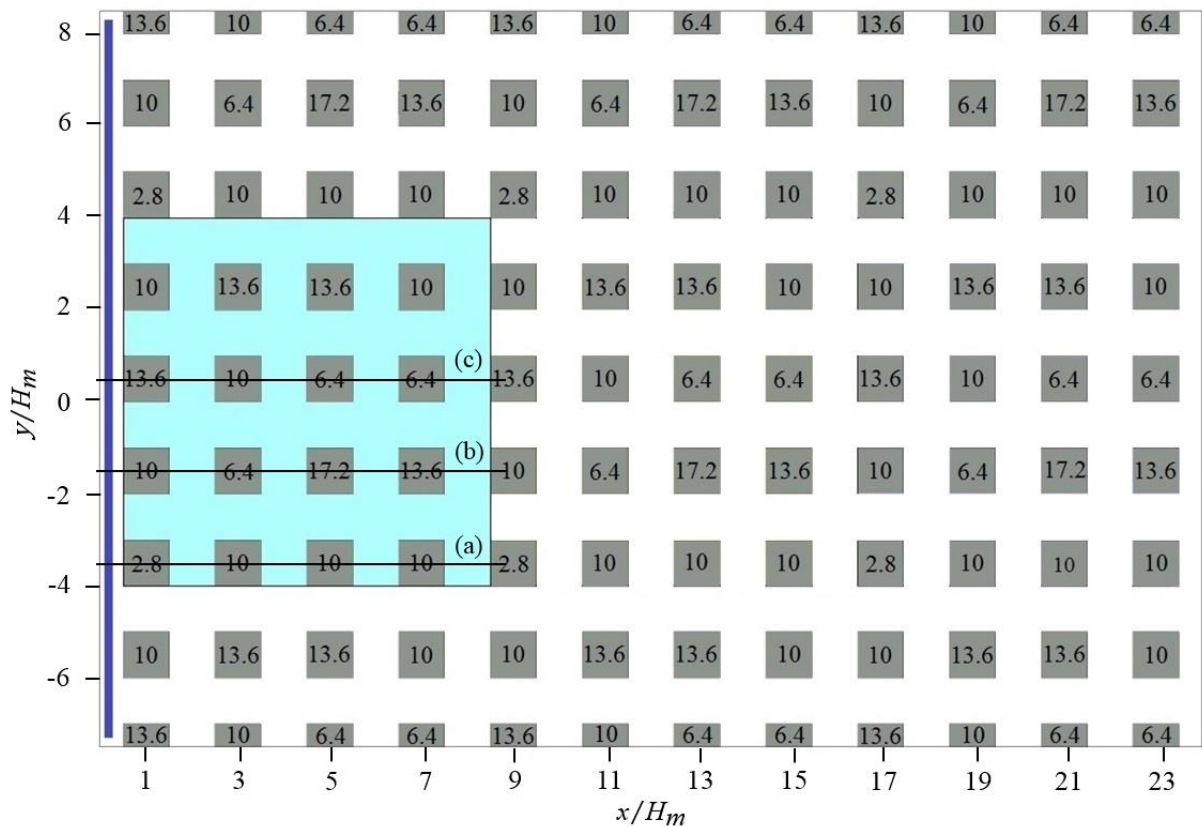


Figure 22. Plan view with indications for the group of buildings with (a) at least one building lower than the average height, (b) at least one building taller than the array average height and (c) one building taller and one lower than the average height for RBAA

Figure 23 demonstrates that the flow structure inside the canyon between successive buildings are different from the staggered array. The structure is presented as stable vortex, where different building heights provides slightly distinct features. For example, Figure 23a illustrates that between two buildings with 10mm a stable recirculation appears with similar updrafts (leeward side) and downdrafts (windward side), while between a building with 17.2mm and 6.4mm greater velocity magnitudes is observed due to strong downdraft in from of the taller building (Figure 23b). Interesting to note in Figure 23b that in front a tall building (13.6mm) is observed upward motion, due to the presence of a taller upwind building (17.2mm). This fact

announces that the height of the upwind building is important to determine the flow around buildings.

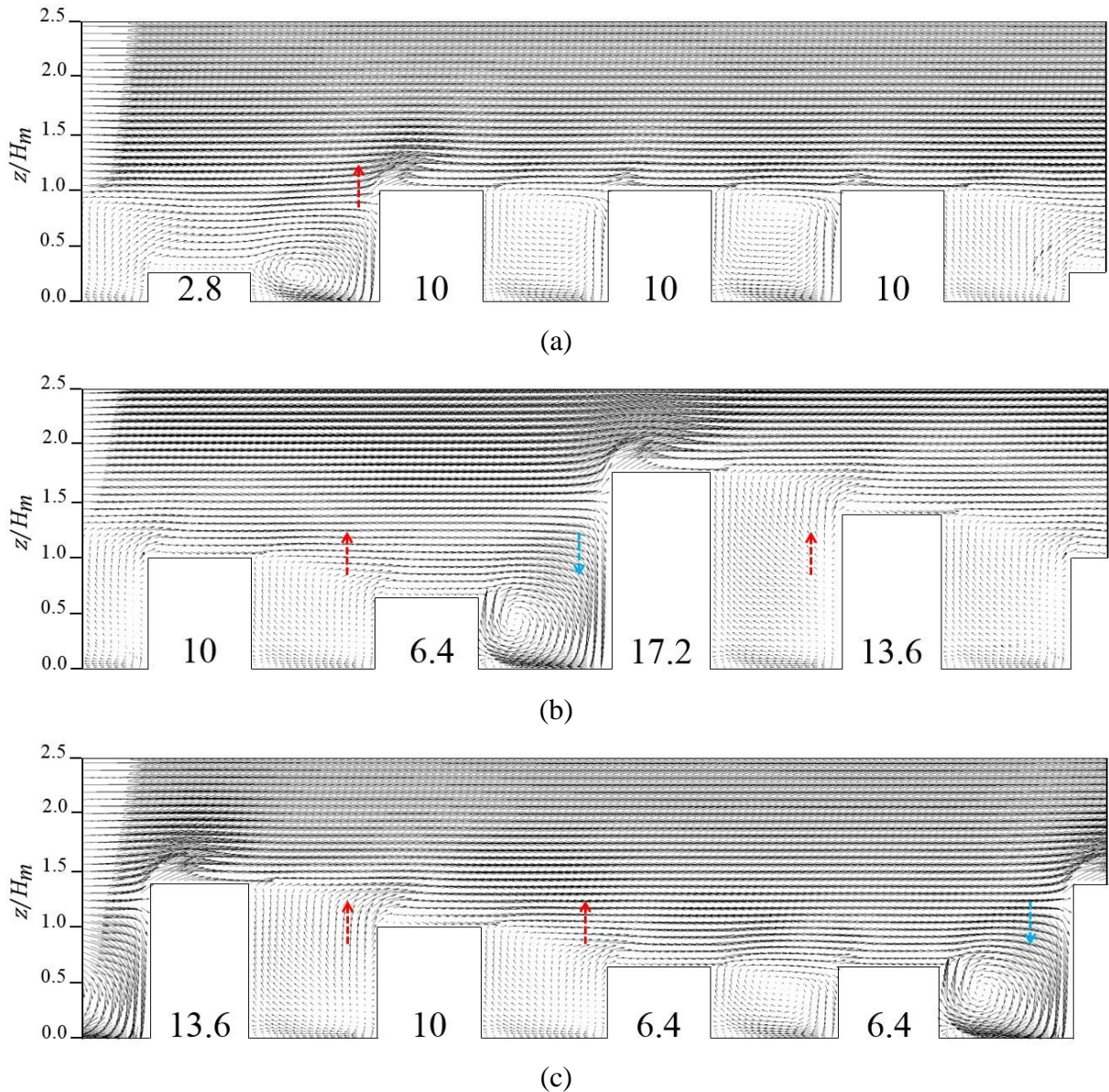


Figure 23. Time-averaged velocity vectors in the $x-z$ plane located at (a) $y/H_m = -3.5$, (b) $y/H_m = -1.5$ and (c) $y/H_m = 0.5$ for RBAA. Arrows indicate the direction of the flow and numbers indicate the building height in millimetres

Figure 24 shows the contours of normalised streamwise velocity ($u^* = \bar{u}/u_\tau$) for the staggered arrays $z/H_m = 0.28$ and $z/H_m = 1.00$. For the UBSA, the flow is quasi-symmetric and presents similar features around the buildings throughout the domain for a specific height. On the other hand, the RBSA configuration present a non-symmetric flow due to the influence of different building heights.

Near the ground for UBSA (Figure 24a), there are two characteristic regions between two successive buildings, the first is a low-speed region just behind the upwind building with

negative velocities comprising the extension of approximately $1.00H_m$ in extension behind the building. The second region (after $1.00H_m$ downwind the building) counts with higher speeds that gradually diminishes until colliding with the next building surface. Figure 24b demonstrates that at the same height ($z/H_m = 0.28$), RBSA presents a considerable faster regions and an intensified reverse flow region in magnitude, but not in extension, behind the taller buildings.

Figure 24d and Figure 24e show the velocity contours at the average height (10mm). For RBSA configuration, strong velocities are still observed at both sides of taller buildings and an evident reverse region appears at the side of the next building behind the tallest building, supporting the features of the flow field streamline presented in Figure 18. Figure 24c and Figure 24f illustrate the contours of streamwise velocity at $z/H_m = 0.28$ and $z/H_m = 1.00$ for RBAA configuration. Figure 24c demonstrates that a recirculation zone is evident behind the buildings near the ground consisting of a region with reverse flow and low speeds. Moreover, these regions are weakened with increasing height as the streamwise velocity rises in magnitude (Figure 24f).

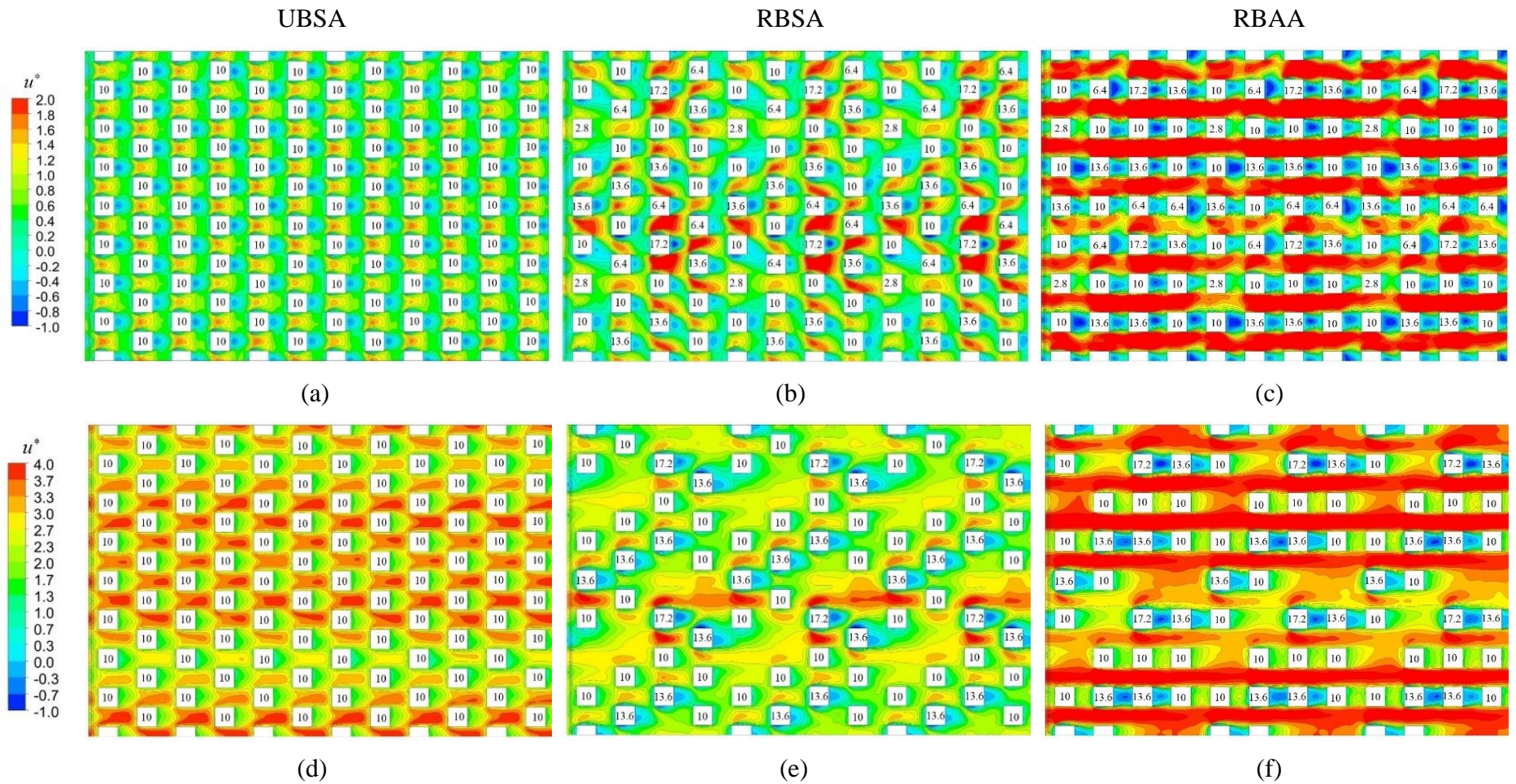


Figure 24. Contours of normalised streamwise velocity in the $x - y$ plane located at (a) $z/H_m = 0.28$ and (d) $z/H_m = 1.00$ for UBSA, (b) $z/H_m = 0.28$ and (e) $z/H_m = 1.00$ for RBSA, (c) $z/H_m = 0.28$ and (f) at $z/H_m = 1.00$ for RBAA

Figure 25 shows the contours of normalised vertical velocity ($w^* = \bar{w}/u_\tau$) for the staggered arrays $z/H_m = 0.28$ and $z/H_m = 1.00$. Figure 25a shows that the flow presents symmetric features through the entire domain near the ground for UBSA array. At this level, downdraft motions are observed in front of the buildings extending to lateral sides of the building, while updraft movements appear just behind the building. In addition, there is a clear vertical velocity gradient in the region between two successive buildings in the streamwise direction. Similar overall pattern was found for RBSA configuration (Figure 25b). However, the downdraft motions are enhanced in front of taller buildings and the downdraft movements are weakened behind the buildings, compared with the regular array.

The influence of taller buildings over the vertical velocity distribution is quite clear when Figure 25d and Figure 25e are analysed. Strong updraft motions raised by the separation zone appears just in front of the buildings on RBSA array, while behind the buildings the velocity is definitely low close to zero. Despite similar pattern around the buildings in the regular array at $z/H_m = 1.00$ (Figure 25d), the tall buildings with $z/H_m = 1.36$ and $z/H_m = 1.72$ present stronger upward motion in front of them and stronger downward behind the buildings (Figure 25e).

Figure 25c and Figure 25f illustrate the contours of normalised vertical velocity for RBAA at $z/H_m = 0.28$ and $z/H_m = 1.00$. Different from the pattern observed in the random staggered array, Figure 25c shows that there is downdraft in front of buildings that are preceded by a smaller building. A similar pattern is demonstrated in Figure 25f, in which taller buildings shelters the following buildings, presenting strong downdraft motion in front of the building and upward flow behind the building.

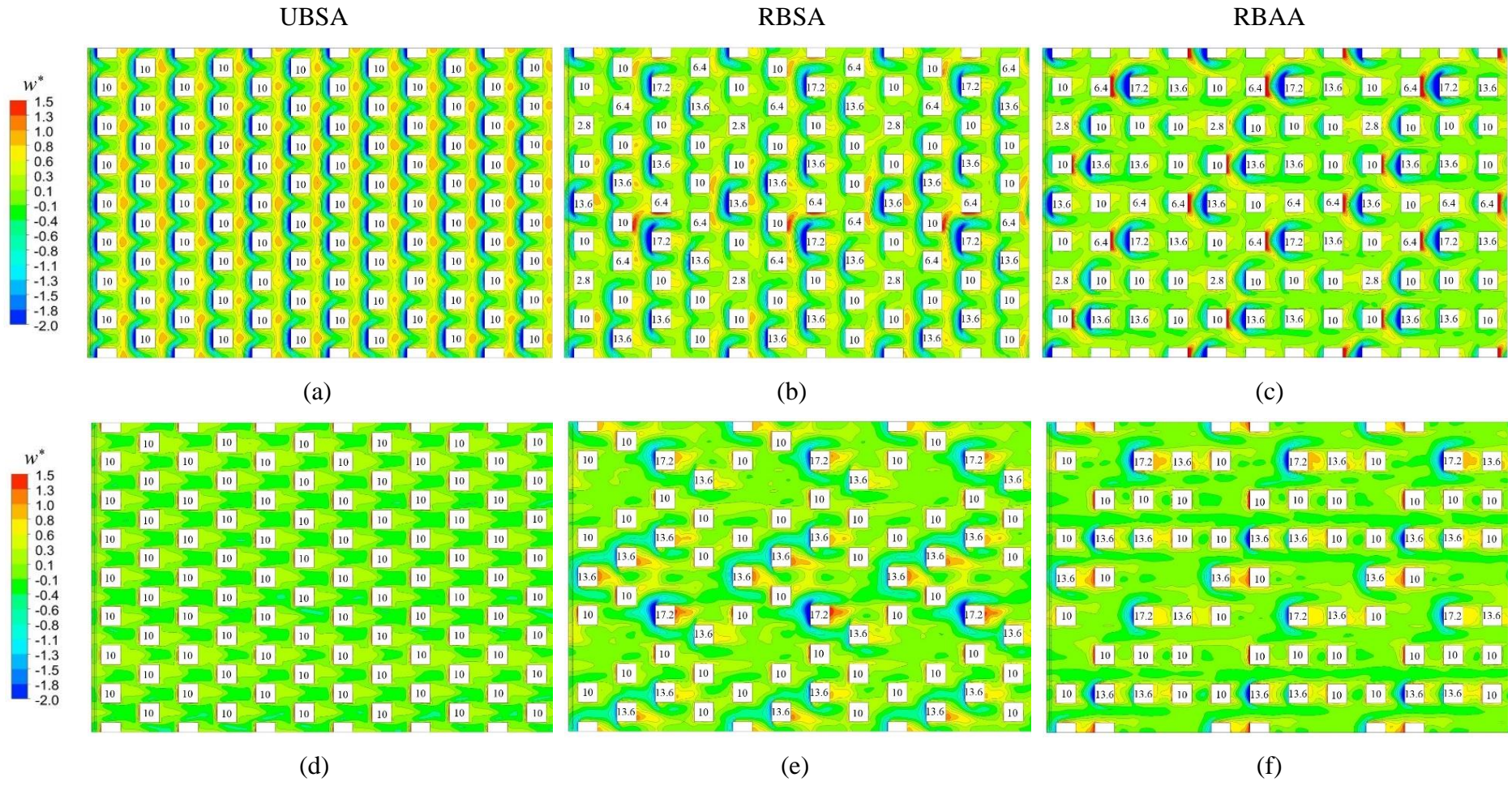


Figure 25. Contours of normalised vertical velocity in the $x - y$ plane located at (a) $z/H_m = 0.28$ and (d) $z/H_m = 1.00$ for UBSA, (b) $z/H_m = 0.28$ and (d) $z/H_m = 1.00$ for RBSA, (c) $z/H_m = 0.28$ and (f) $z/H_m = 1.00$ for RBAA

Distribution of the normalised vertical velocity and the vertical velocity root mean squared ($rms w^* = \overline{rms w}/u_\tau$), in vertical planes along the array are presented in Figure 26 for all configurations. The main general structures that can be noticed are the stronger down and updrafts in front of and behind the tall buildings for random heights configurations.

Note also that the tall buildings promote an increase in the turbulent fluctuations of the vertical velocity above the smaller buildings. While the effects related to the mean flow are closer to the tall building, the effects related to the vertical velocity fluctuations, and consequentially the turbulent vertical fluxes, seem more largely spread downwind above the smaller buildings, demonstrating a non-local effect. In fact, it is clear that the increase in the turbulent fluctuations of the vertical velocity due to the presence of a tall building can be observed above smaller building as far as $7H_m$ downwind (Figure 26d and Figure 26f).

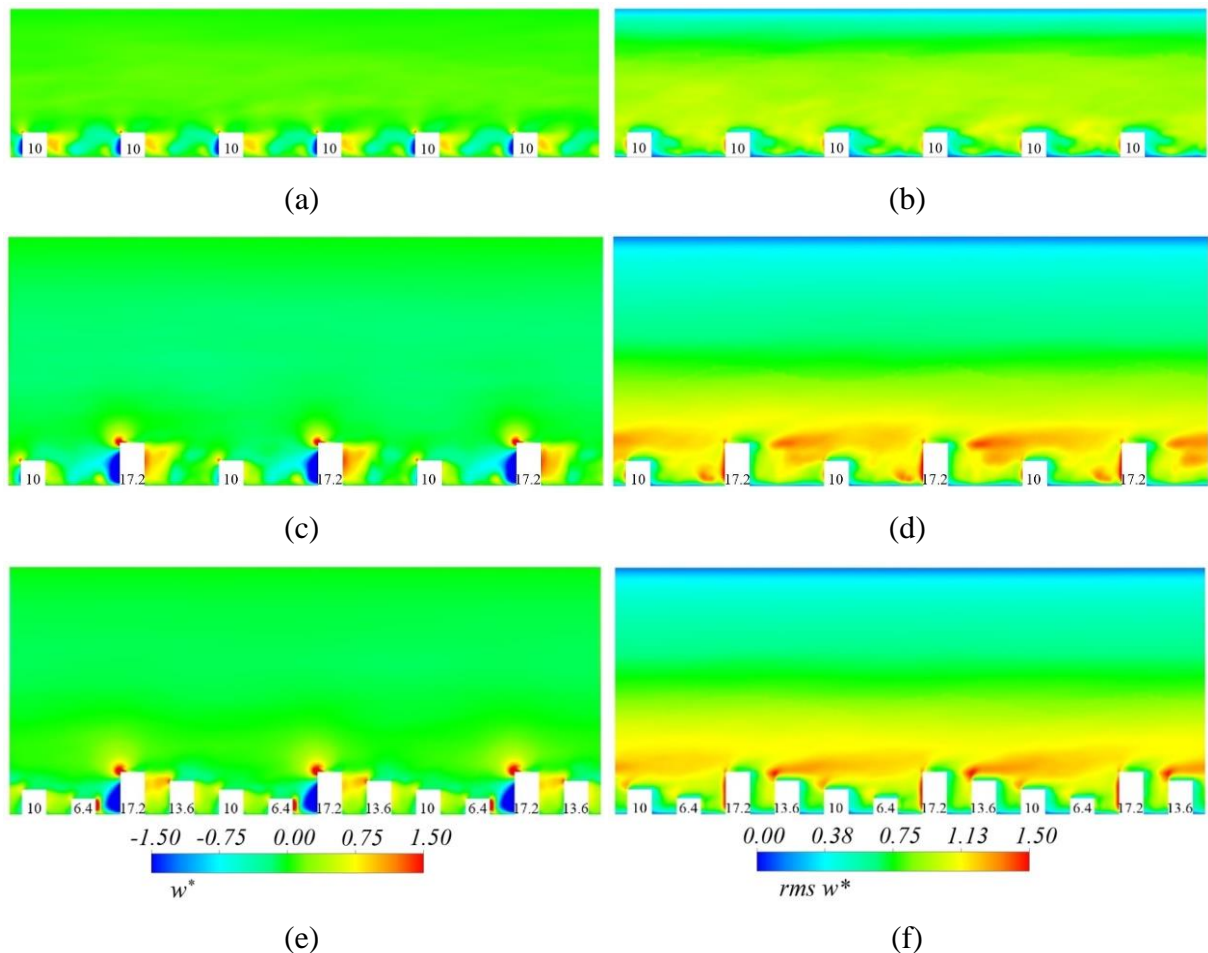


Figure 26. Distribution of normalised vertical velocity and vertical velocity rms in the $x - z$ plane located at $y/H_m = -1.5$ for (a) (b) UBSA and (c) (d) RBSA and (e) (f) RBAA

It seems that random height buildings enhance turbulence intensity and therefore, the turbulent fluxes. The intensity of the effects of the turbulent structures seems to be related to the buildings

height variation. The higher the building height, the higher is the layer at which the flow has larger vertical velocity fluctuations.

4.3 CONCENTRATION FIELD

This section describes the characteristics of the concentration field for the urban configurations presented in section 3.1. The analyses are made at different heights in an attempt to better describe the effects on dispersion pattern due to the presence of buildings with different heights and arrangements.

Figure 27 shows the contours of normalised concentration ($c^* = c/c_0$, where c_0 is the constant concentration imposed at the area source) in the vertical $x - y$ plane for all configurations. The randomness in the height of the buildings is responsible for the high irregularity on dispersion field for RBSA configuration above the area source Figure 27b and Figure 27e. In addition, a regular dispersion pattern is observed for uniform array consisting of high concentration zones behind the buildings and low concentration zones in front of them as can be seen in Figure 27a Figure 27d.

The influence of tall buildings is quite clear. For example, the stable vortex that occurs in front of the buildings with $z/H_m = 1.36$ and $z/H_m = 1.72$ act “cleaning” the air inside the canopy due to strong downdrafts. Figure 27d and Figure 27e demonstrate that the lateral dispersion for RBSA is higher than UBSA after the distance of $8.0H_m$ downwind the area source, while the latter presents almost constant spanwise dispersion with distance. In fact, Boppana, Xie and Castro (2010) simulated a computational domain with $y/H_m = 16$ (2/3 of the present simulation) and could not observe the dispersion effects further downwind. In addition, the concentration inside the canopy is larger for the uniform configuration, which indicates that tall buildings enhance the vertical dispersion.

Figure 27g and Figure 27h show similar features of the high concentration regions almost at the same location, perhaps not expected for UBSA. This pattern can be explained by the position of the tall building in the RBSA configuration, which promotes strong vertical dispersion behind them. The high concentration regions are just above the tall building, although such buildings are evidently absent in the regular array.

By observing the concentration distributions for plans located at $z/H_m = 1.00$ and $z/H_m = 1.72$, it is possible to note that the tall buildings act just like chimneys, transporting pollutants vertically to upper levels, due to strong updrafts behind the buildings.

Figure 27c and Figure 27f demonstrate that the concentration field in RBAA configuration at $z/H_m = 0.28$ and $z/H_m = 1.00$ are similar to the dispersion pattern presented for RBSA array. Nonetheless, Figure 27i portrays only one longer high concentration zone located downstream the tall building. In addition, the range of the dispersion in the streamwise direction is approximately the same as demonstrated for UBSA, illustrating that despite the flow channeling in the aligned array, tall buildings also strongly contribute enhancing the vertical dispersion.

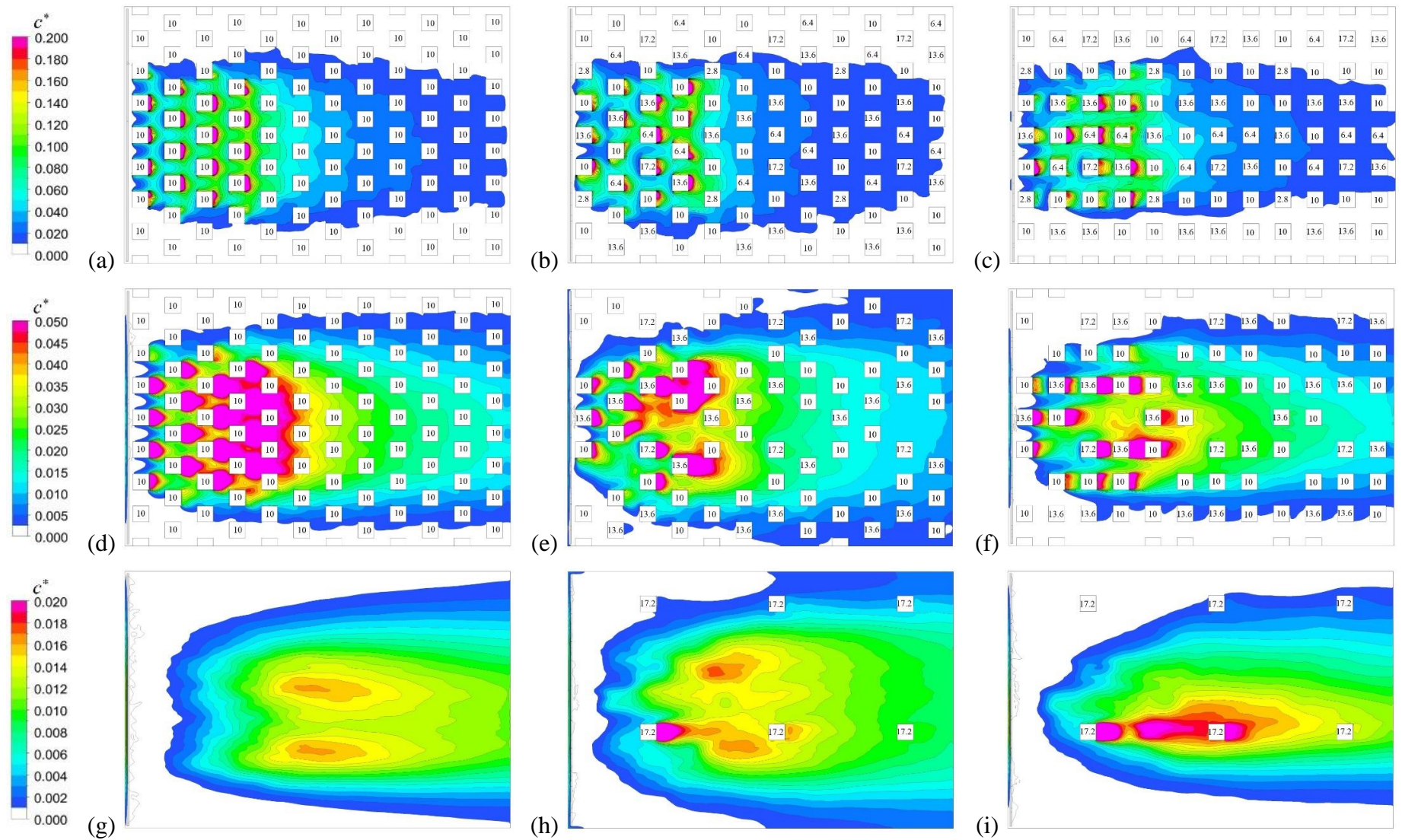


Figure 27. Contours of normalised concentration at (a) $z/H_m = 0.28$, (d) $z/H_m = 1.00$ and (g) $z/H_m = 1.72$ for UBSA, (b) $z/H_m = 0.28$, (e) $z/H_m = 1.00$ and (h) $z/H_m = 1.72$ for RBSA, (c) $z/H_m = 0.28$, (f) $z/H_m = 1.00$ and (i) $z/H_m = 1.72$ for RBAA.

Figure 28 presents the concentration iso-surfaces in a three-dimensional view of the simulated cases, which is perhaps a most effective visual representation of the pollutant dispersion. The effect of taller buildings is clearly illustrated with two pollutant concentration regions. The low concentration zone is illustrated in blue colour ($c^* = 0.02$), while the high concentration zone is illustrated in red colour ($c^* = 0.10$).

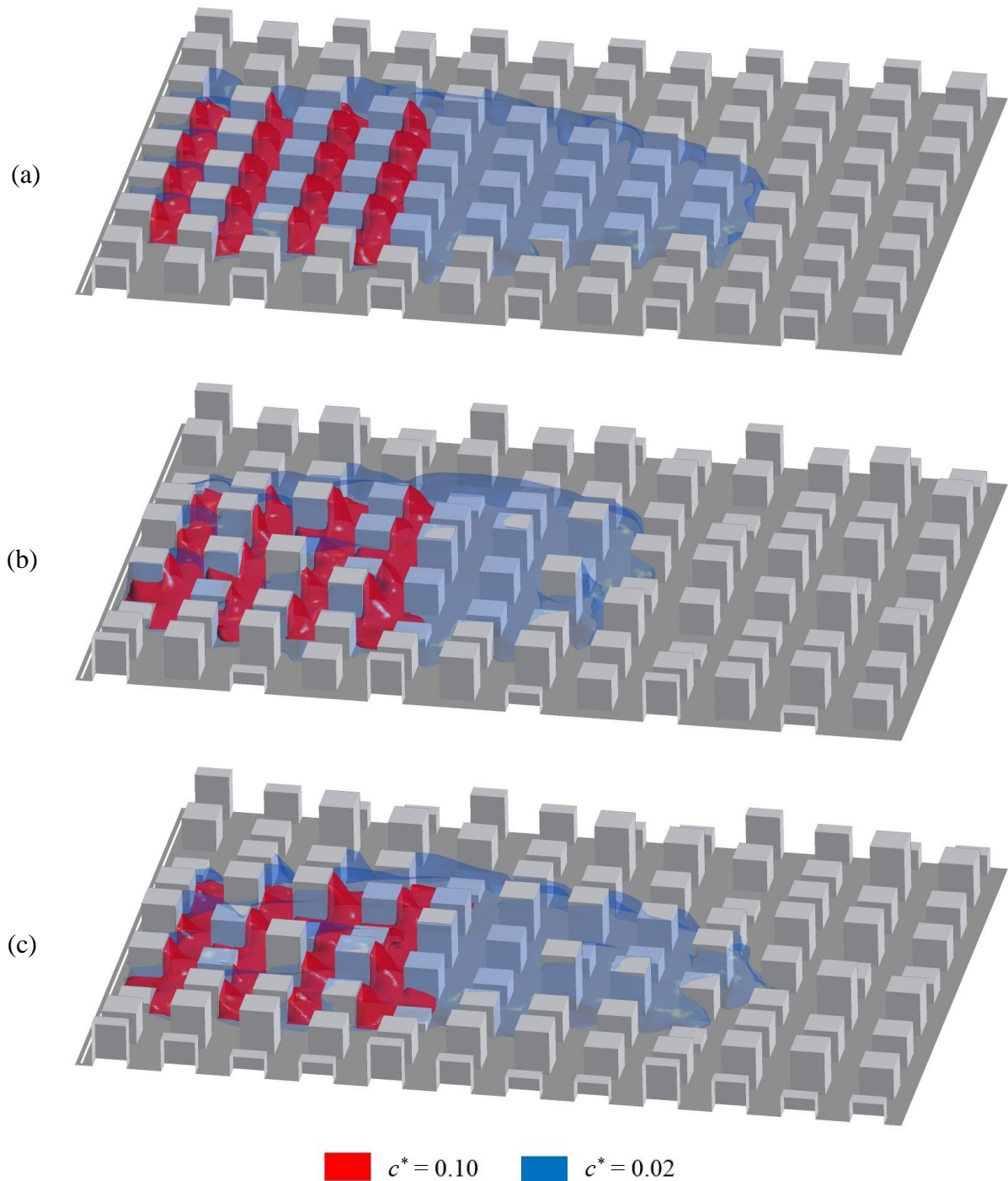


Figure 28. Mean normalised concentration iso-surfaces for (a) UBSA, (b) RBSA and (c) RBAA configurations

Figure 28a demonstrates a regular concentration pattern above the area source in the UBSA configuration, where the high concentration zone reaches the rooftop level behind the buildings and is minimized in front and in the lateral sides. On the other hand, the random height arrays demonstrate an irregular pattern, with high concentration zones reaching greater vertical distances from the ground, supporting that the stronger upward motions behind tall buildings are responsible for removing the pollutant from within the canopy.

The pollutant plume within the RBSA configurations reaches shorter streamwise distance compared to the uniform array. Aristodemou et al. (2018) illustrated the same pattern regarding the influence of taller buildings on the spread of the pollutant plumes downwind the array. At the same time, the tall buildings also contribute to enhance both lateral and vertical dispersion. However, Figure 28c demonstrates that the aligned configuration does present smaller lateral and vertical dispersion in comparison with the staggered arrangement (RBSA), leading to a longer plume downwind the buildings. While the advection contribution in the RBAA array is responsible to carry the pollutant further away from the source, the tall buildings with the strong vertical motions balances the plume spread.

Figure 29 shows contours of normalised concentration in the vertical $x - z$ plane for UBSA configuration at $y/H_m = 6.0$. The characteristics of the mean velocity vectors presented in Figure 19 determines the dispersion pattern between successive buildings in the uniform array. Therefore, the concentration distribution is presented with following such a pattern. However, high concentration zones appear between the first three buildings because they are just above the area source.

The downdraft flow in front of the buildings is responsible for “cleaning” the air in that region, while high concentration zones are observed due the recirculation behind them. This pattern repeats between successive buildings further from the source but it is not quite clear, since the concentration rapidly decreases after the source. In the middle of the canyon, at approximately $x/H_m = 1.0H_m$ downwind, is observed a specific form due the separation zone that exists in that region, where a reverse flow is observed between that line and the leeward side building, while forward flow is observed between that line and the windward side building. In addition, the high concentration zone is more intensified behind the second building above the area source, since more pollutant reaches its recirculation zone.

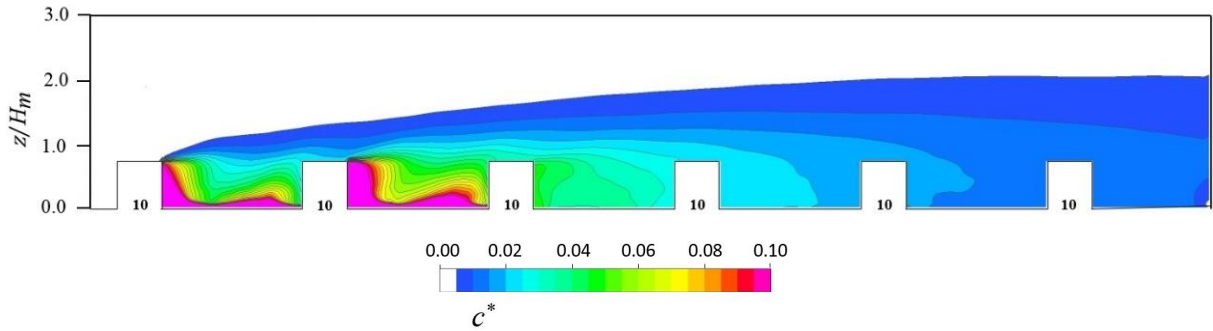


Figure 29. Contours of normalised concentration in the $x - z$ plane at $y/H_m = 6.0$ for UBSA. The numbers indicate the building height in millimetres

A similar pattern of concentration distribution is observed for RBSA configuration. Although, some discrepancies due to the presence of different building height is notable in RBSA configuration (Figure 31). Figure 30 demonstrates the groups of buildings (cases a, b and c) for RBSA configuration.

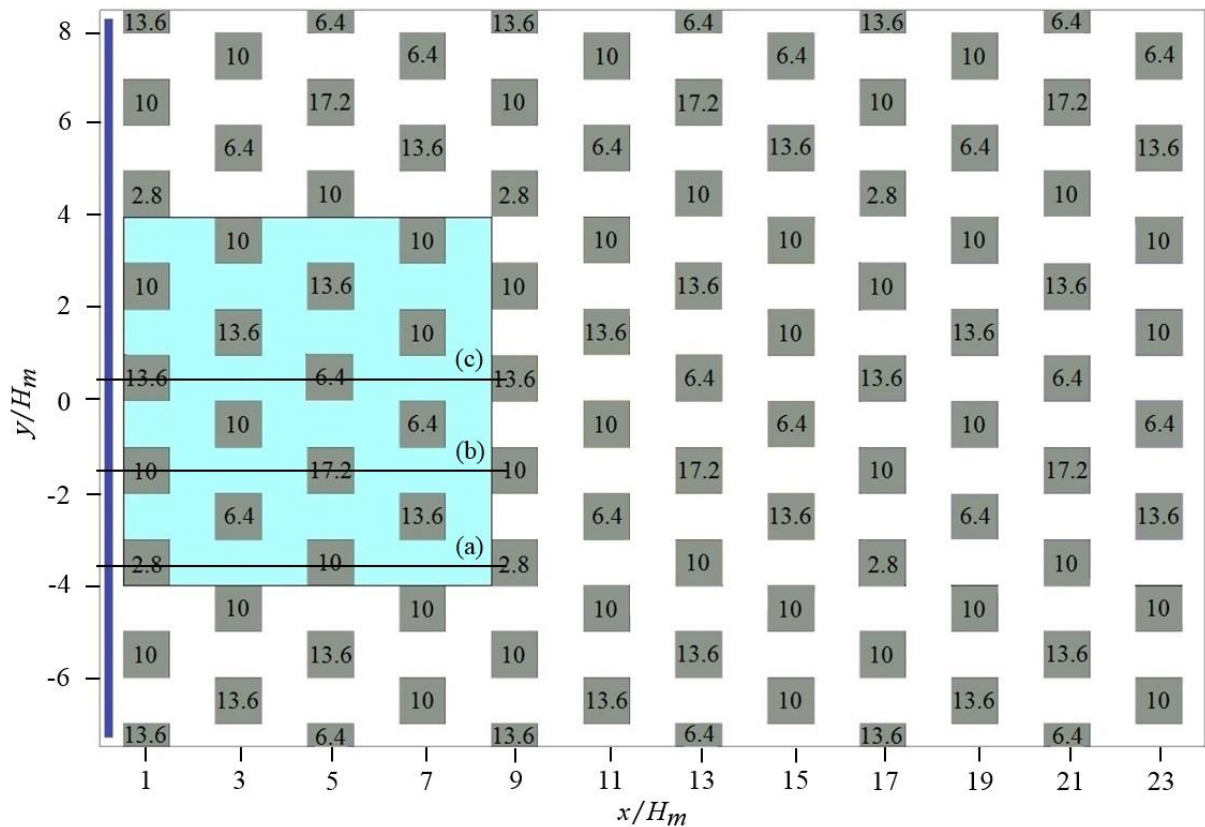


Figure 30. Plan view with indications for the group of buildings with (a) at least one building lower than the average height, (b) at least one building taller than the average height and (c) one building taller and one lower than the average height for RBSA

Figure 31a illustrates that the shorter building ($z/H_m = 0.28$) does not present downdraft motions strong enough for cleaning the air in front of it, probably due to the sheltering process that

occurs behind the upwind taller building. Figure 31b and Figure 31c demonstrate that the strong downward motion is responsible to remove away the pollution in front of a building taller than the average height.

Another aspect that worth to mention is about the reach of the high concentration zone behind the buildings. This zone reaches the height of approximately $1.0H_m$ in UBSA configuration, while the same zone reaches almost all vertical extension of the buildings in the random arrays. Therefore, the pollutant seems to be transported more efficiently upwards, due to the presence of taller buildings. Figure 31c demonstrates that even behind the building with $z = 0.64H_m$ the high concentration zone reaches larger vertical extension than the building height itself, demonstrating the influence of surrounding taller buildings.

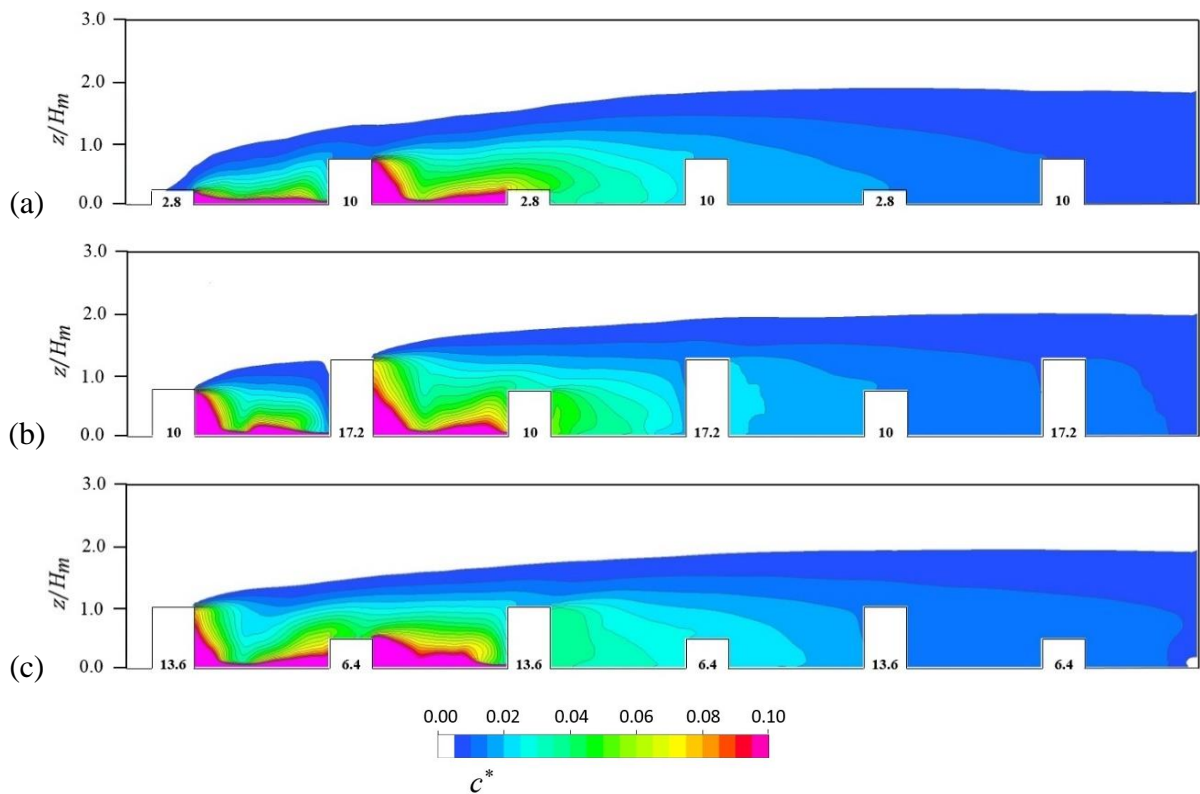


Figure 31. Contours of normalised concentration in the $x - z$ plane located at (a) $y/H_m = -3.5$, (b) $y/H_m = -1.5$ and (c) $y/H_m = 0.5$ for RBSA. The numbers indicate the building height in millimetres

Figure 32 demonstrates the groups of buildings (cases a, b and c) for RBAA configuration. Figure 33 shows contours of normalised concentration in the vertical $x - z$ plane for RBAA configuration at the same locations as for RBSA.

According to the mean velocity vectors presented in Figure 23, the aligned configuration has the same flow structure as that described by Oke (1988) as skimming flow. Consequently, the

type of the flow structure and the morphology of two successive buildings determine the concentration distribution. For example, when the 17.2m building is at the windward side and a small is in the leeward side the spatial concentration distribution extends in the direction of the mean flow inside the canopy, where strong updraft is observed in front of the taller building and a greater ‘clean’ zone is observed (Figure 33b). Kubilay et al. (2017) demonstrate the same aspect of scalar dispersion from a point source released near the ground level inside a regular canyon of aspect ratio equals to the unit.

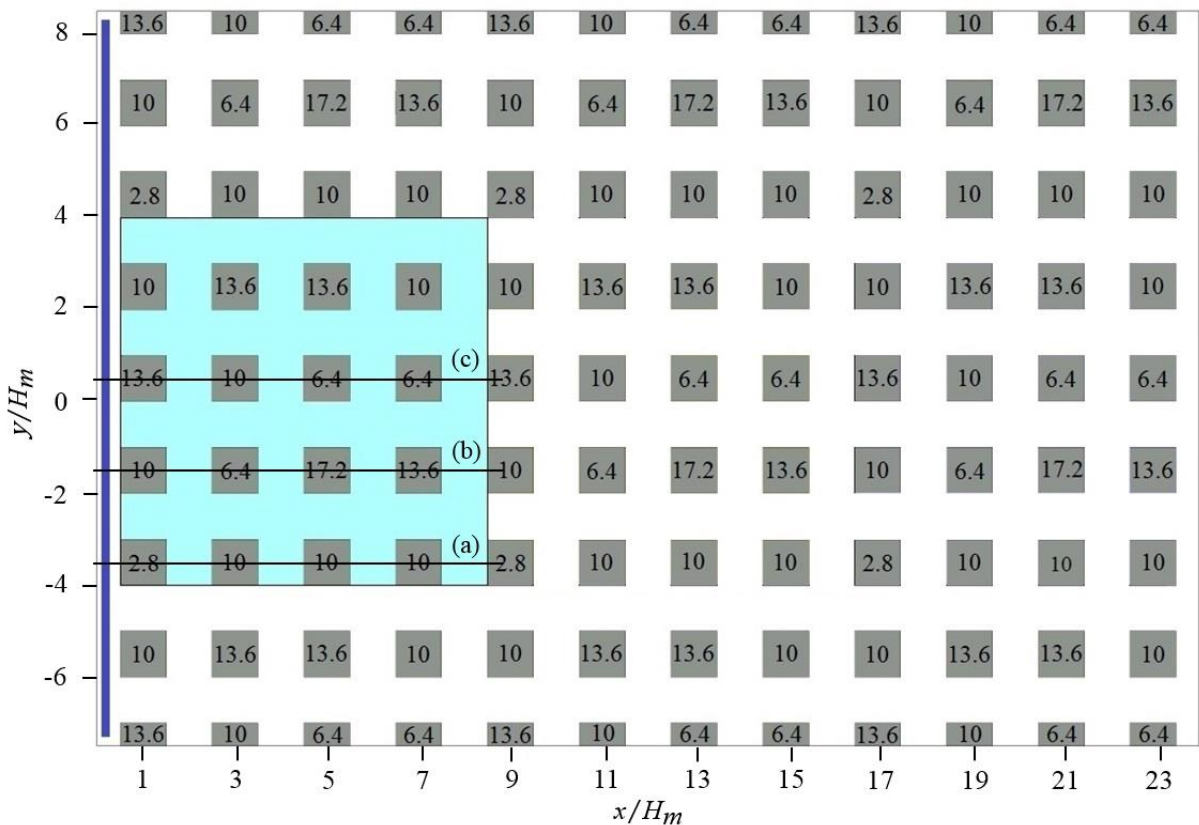


Figure 32. Plan view with indications for the group of buildings with (a) at least one building lower than the average height, (b) at least one building taller than the array average height and (c) one building taller and one lower than the average height for RBAA

On the contrary, a different feature is observed when a smaller building is in front of a tall one, or in the same height, building. The spatial concentration distribution presents a region with high concentration above the area, which extends from the rooftop level of the upwind building to the ground level of the downwind building (Figure 33a).

Nonetheless, a different feature is observed in the region between two successive tall buildings. For example, Figure 33c demonstrates that the pollutant is trapped near the ground due to weak vertical dispersion inside the canyon between the two buildings with $z/H_m = 1.36$. For that

reason, the high concentration regions reach the mean height of the building at the leeward side. Figure 33b illustrates the same dispersion pattern inside the canyon between the two buildings with $z/H_m = 1.72$ and $z/H_m = 1.36$.

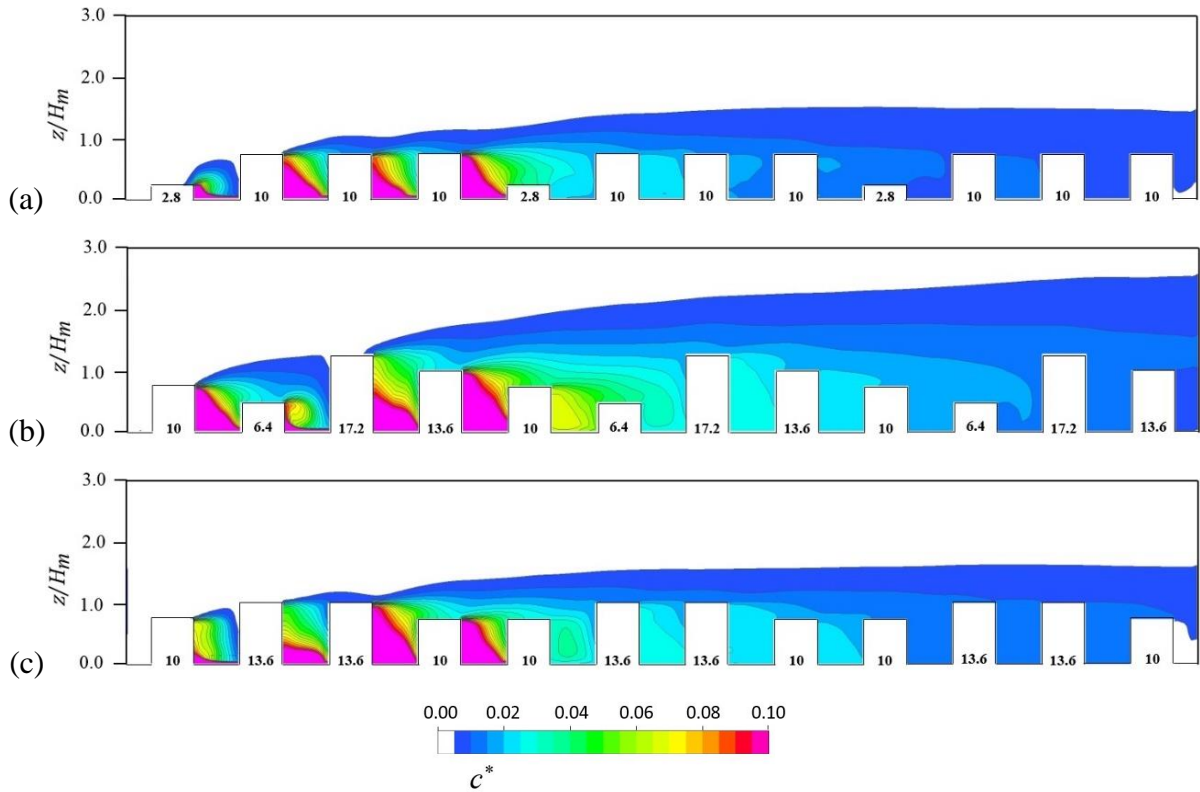


Figure 33. Contours of normalised concentration in the $x - z$ plane located at (a) $y/H_m = -3.5$, (b) $y/H_m = -1.5$ and (c) $y/H_m = 0.5$ for RBAE. The numbers indicate the building height in millimetres

4.4 POLLUTANT FLUXES

This section describes the characteristics of the pollutant mass (scalar) transport for the urban configurations presented in Section 3.1. The analyses are made at different locations in an attempt to better describe the effects on scalar fluxes due to the presence of buildings with different heights and arrangements.

The analysis of scalar flux is quite relevant because they allow researchers to explore the physics behind different morphologies in environmental studies. This may give support for the development of analytical for fluctuations of the pollutant mass fluxes inside and outside the canopy, which are required to create simpler algebraic models such as street network models (GOULART; COCEAL; BELCHER, 2018; HERTWIG et al., 2018). In addition, the major

advantage of large-eddy simulation, compared to RANS approaches, is the possibility to obtain such data explicitly.

The total scalar flux is divided into the turbulent and advective contributions. The spatial average of the vertical scalar fluxes was calculated at the average building height for all simulations as

$$\underbrace{\langle \overline{c w} \rangle}_{\text{Total flux}} = \underbrace{\langle \overline{c} \rangle \langle \overline{w} \rangle}_{\text{Advective flux}} + \underbrace{\langle \overline{c' w'} \rangle}_{\text{Turbulent flux}}$$

where

$$\langle \overline{c w} \rangle = \frac{1}{A} \int_A \overline{c w} \, dA$$

$$\langle \overline{c} \rangle = \frac{1}{A} \int_A \overline{c} \, dA$$

$$\langle \overline{w} \rangle = \frac{1}{A} \int_A \overline{w} \, dA$$

Where $\langle \rangle$ denotes the spatial average, $\overline{}$ represents the time average, c is the concentration, w is the vertical velocity component (in the z -axis direction), w' is the vertical velocity fluctuation, and A is the square area at the average building height, comprising of $L_x \times L_y = 1H_m \times 1H_m$.

The total flux, the turbulent and advective contributions are normalised by the time-averaged scalar flux emitted by the area source calculated based on the pollutant mass flow of the substance leaving the outlet. The averaged scalar fluxes at the source were $6.27 \times 10^{-6} \text{ kg m}^{-2} \text{ s}^{-1}$, $7.37 \times 10^{-6} \text{ kg m}^{-2} \text{ s}^{-1}$ and $7.12 \times 10^{-6} \text{ kg m}^{-2} \text{ s}^{-1}$, for UBSA, RBSA and RBAA, respectively. These suggest that variation of the building height enhances the canopy ventilation compared to a uniform height case, and staggered arrangement of the buildings slightly enhances the canopy ventilation compared to the aligned arrangement.

Figure 34 illustrates the scalar fluxes over a line at $y/H_m = 0.5$ that is a representative pattern for all lines over the array of uniform height buildings. The results indicate that the scalar transfer contains significant turbulent and advective components of the vertical flux. It is important to notice that the total flux reaches its maximum at $x/H_m = 6.0$ and rapidly decreases after the area source. The advective vertical scalar flux is negative at locations where the vertical component of the velocity is also negative and is responsible for enhancing the concentration

within the canopy. These locations are in front of the buildings and between the buildings, while behind the buildings the advective flux is always positive as can be seen in Figure 34c.

On the other hand, the vertical turbulent scalar flux is always positive and it is responsible for reducing the concentration within the canopy. Figure 34b also demonstrates that the turbulent fluxes are important behind the buildings and decrease its importance away the area source. In general, the total flux follows the turbulent flux pattern with slight variations demonstrating that the turbulent contribution plays the major role at $z/H_m = 1.0$.

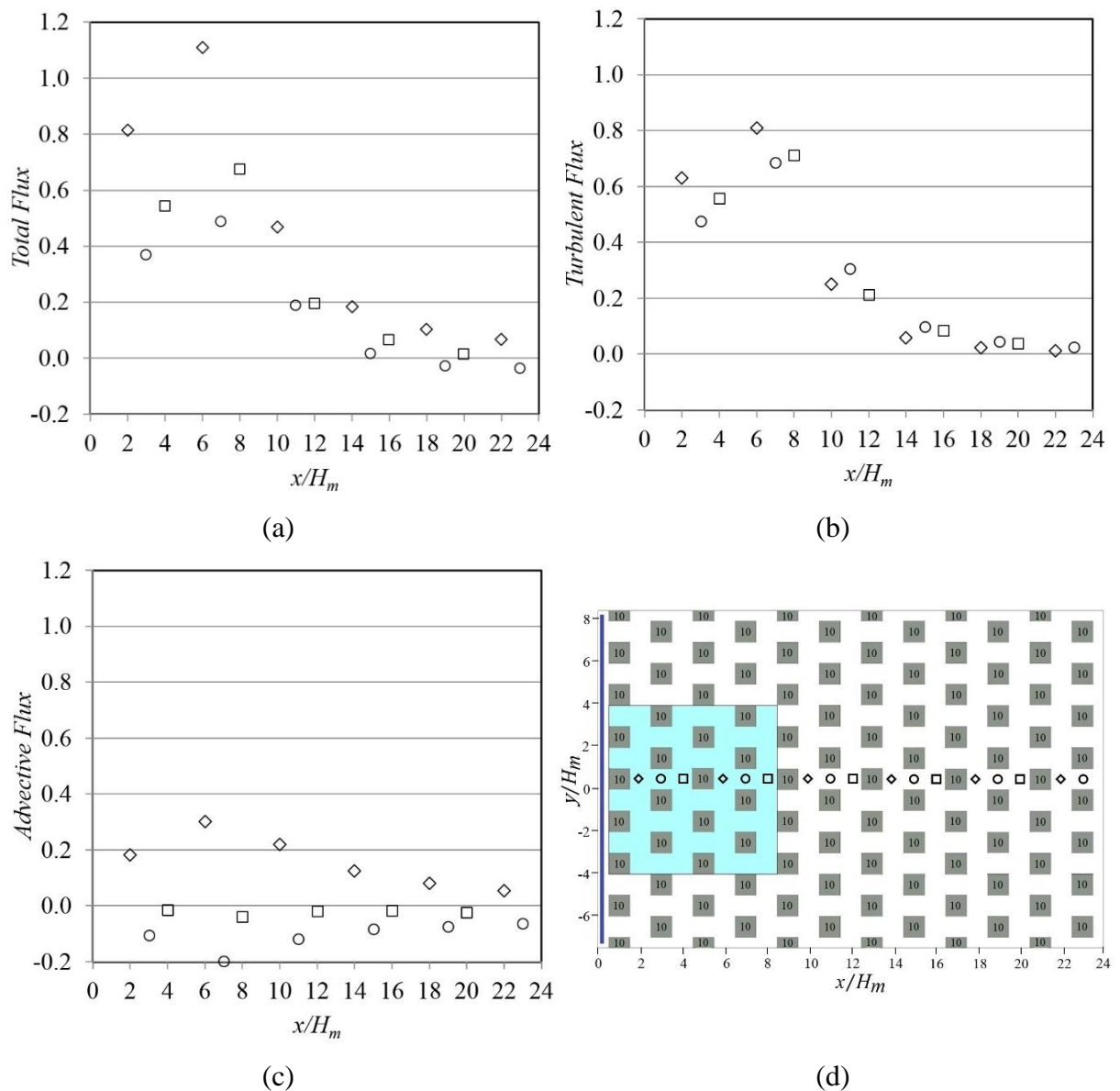


Figure 34. Quantities of normalised (a) total, (b) turbulent and (c) advective vertical scalar fluxes for UBSA configuration. (d) Schematic representation and sampled locations. Symbols indicate the locations behind the building (\diamond), between buildings (\circ) and in front of the building (\square)

In contrast of what is expected for the uniform case, the advective component of the vertical flux becomes increasingly important for the determination of the total vertical scalar transfer at $z/H_m = 1.0$ for the random height configuration. Fuka et al. (2018) supports the idea with their results from an LES simulation in which a tall building was placed within an array with uniform building height. They found that the taller building could significantly enhance or reduce the magnitude of the local scalar vertical flux, due to a significant alteration of the mean velocity field near the tall buildings. Such variations contribute to an increased advective vertical flux bringing “cleaner” air from the upper atmosphere or contributing to a more intense exfiltration of the pollutants from the urban canopy.

Figure 35 presents the group of buildings in the line (a) indicated in Figure 30, when the incoming flow passes over a small building ($0.28H_m$) and an average height building ($1.0H_m$). The vertical scalar flux has similar pattern as the flow over a uniform height array of buildings, since the total flux is dominated by turbulence.

Considerable differences can be pointed out due to the presence of the small building. For example, Figure 35c indicates that the advective contribution is relevant and positive only in front of the average building, while its importance is diminished for the other locations. Figure 35b illustrates that the turbulent flux smoothly increases until it reaches its maximum value at $x/H_m = 6.0$ as observed for the UBSA configuration and, again smoothly decreases its importance with distance from the source.

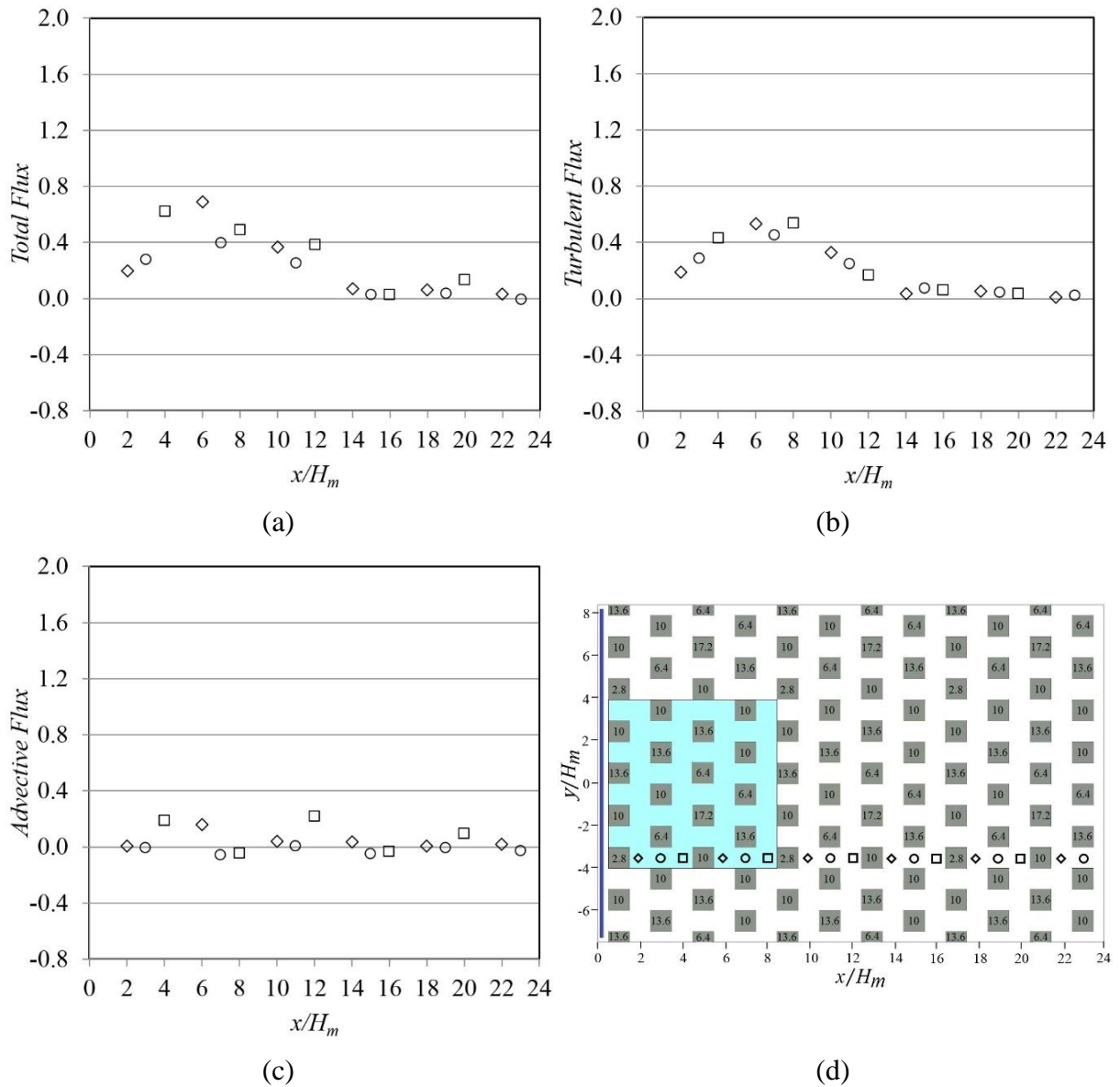


Figure 35. Quantities of normalised (a) total, (b) turbulent and (c) advective vertical fluxes for the RBSA configuration. (d) Schematic representation and sampled locations. Symbols indicate the locations behind the building (\diamond), between buildings (\circ) and in front of the building (\square)

Figure 36 presents the incoming flow passing over a series of buildings with one taller building ($1.72H_m$). The flow is disturbed by its presence and the advective contribution plays an important role on vertical scalar flux. Perhaps not expected, behind the taller building is the location where the total scalar flux attains a maximum value not due to the turbulence generated, but due to the strong positive vertical velocity component (Figure 25c). For the same reason, the advective flux is negative and significant in front of the taller buildings.

In general, Figure 36c demonstrates that the positive advective flux is observed behind the taller building and negative flux occurs through behind the building with average height. However, the contribution of a tall building within the urban canopy is notable. For instance, the positive

flux behind a 17.2mm building ($x/H_m = 6.0$) is about five times greater than the negative flux in front of the same building ($x/H_m = 4.0$) as can be seen in Figure 36a. In addition, the turbulent component behind the tall building provides a weak contribution to total flux at this height (Figure 36b).

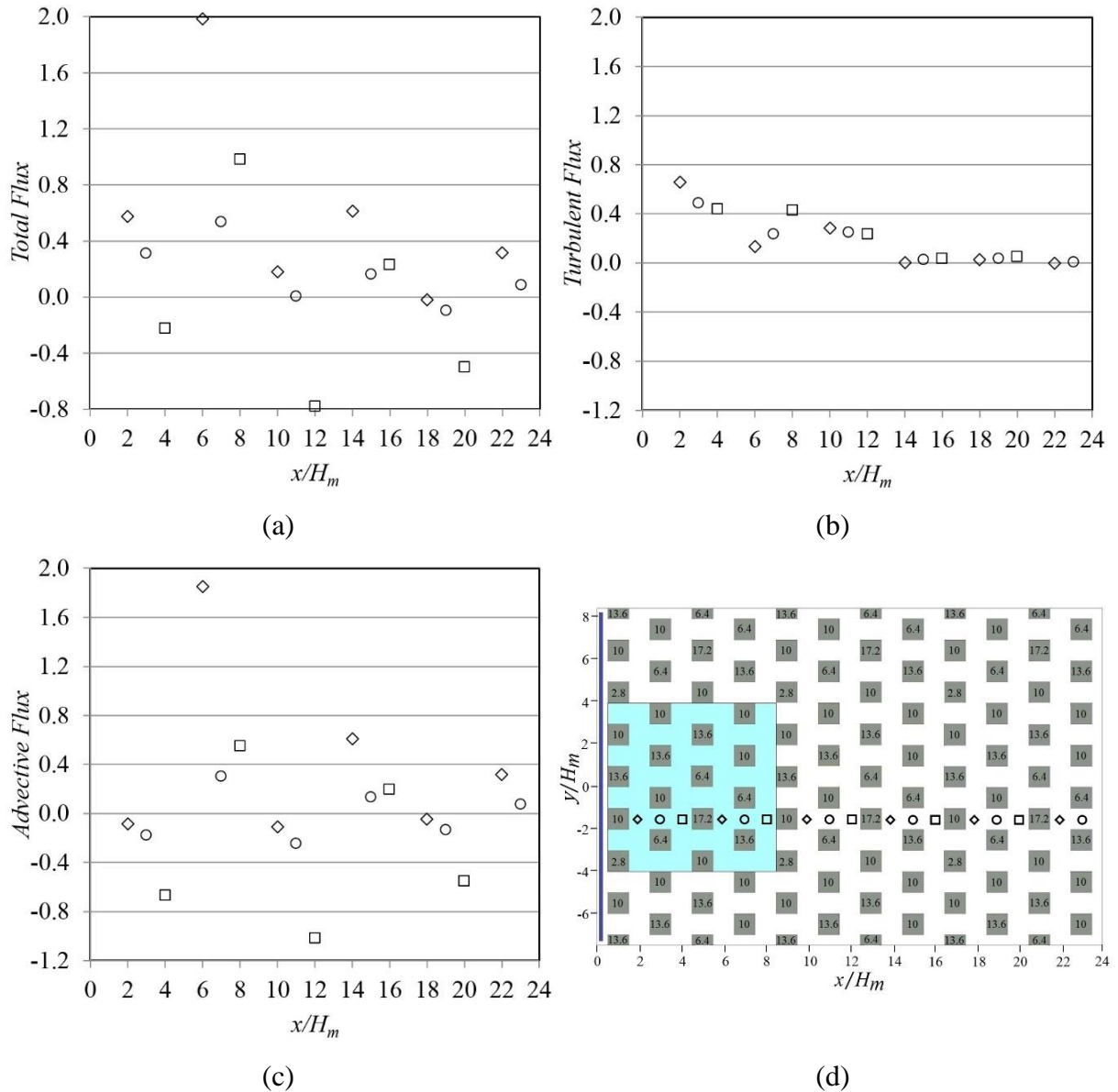


Figure 36. Quantities of normalised (a) total, (b) turbulent and (c) advective vertical fluxes for RBSA configuration. (d) Schematic representation and sampled locations. Symbols indicate the locations behind the building (\diamond), between buildings (\circ) and in front of the building (\square)

Figure 37 presents the group of buildings in the line (a) indicated in Figure 32, when the incoming flow passes over a small building ($0.28H_m$) and an average height building. Figure 37a indicates that the total scalar flux is dominated by the turbulent component. Figure 37c

shows that the advective flux is close to zero, since there is no tall buildings in this line, suggesting that tall buildings of other lines do not influence the flux.

Analysing the aligned array, one can find the same pattern observed in the RBSA configuration, but with a smaller magnitude. Since the aligned array produces more channelled flow than the staggered array, less vertical transport is expected.

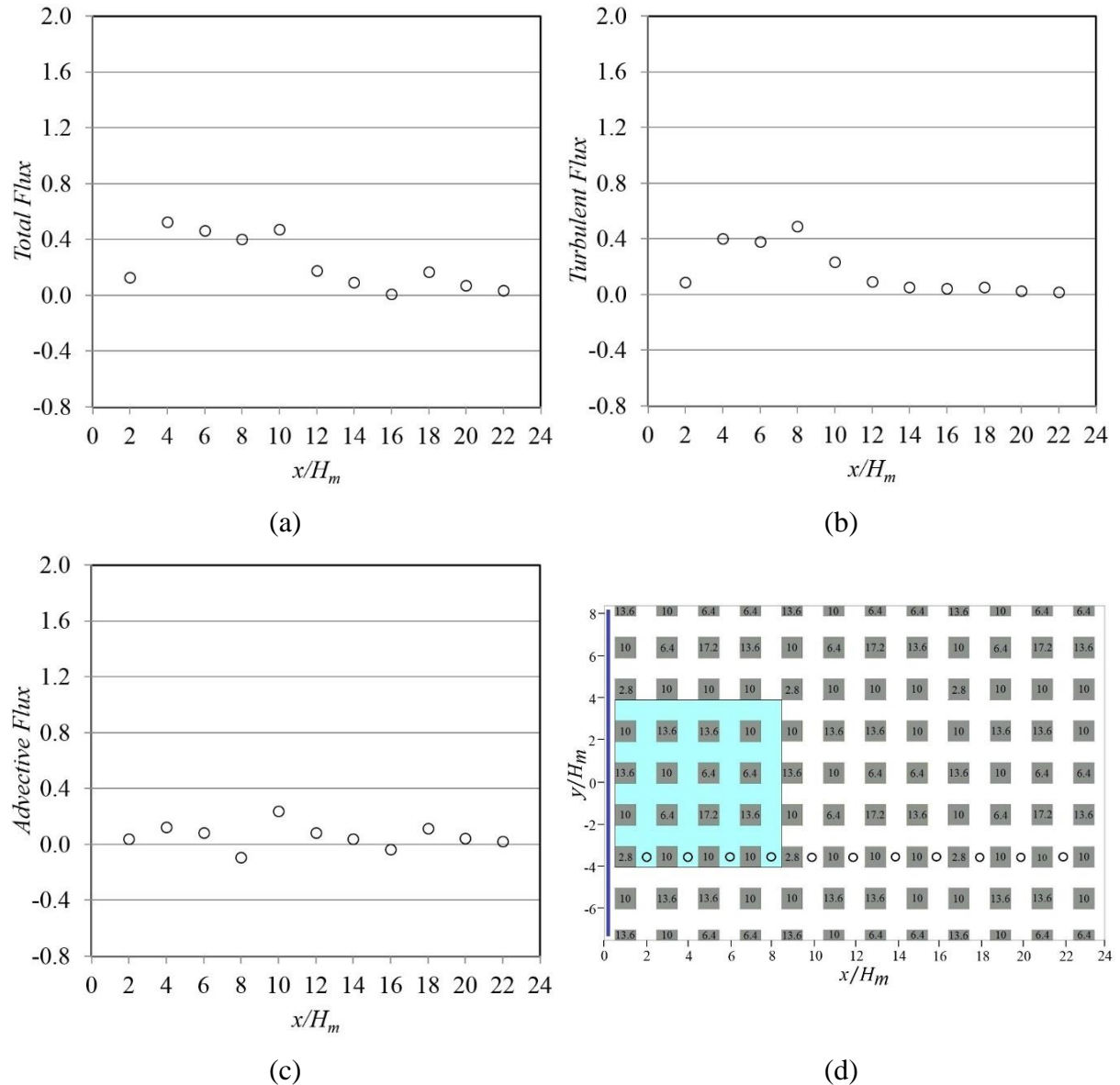


Figure 37. Quantities of normalised (a) total, (b) turbulent and (c) advective vertical fluxes for RBAA configuration. (d) Schematic representation and sampled locations. Symbols indicate the locations between buildings (o)

Figure 38 presents the incoming flow passing over a series of buildings with one taller building ($1.72H_m$) and demonstrates generally similar characteristics as demonstrated for the random staggered arrays at the same line of buildings. Nonetheless, there are two taller buildings along

the sequence of the buildings. It is interesting to note in Figure 38a indicates that the total scalar flux occurs behind the building with the height of $z/H_m = 1.36$ and not behind the tallest building, as expected.

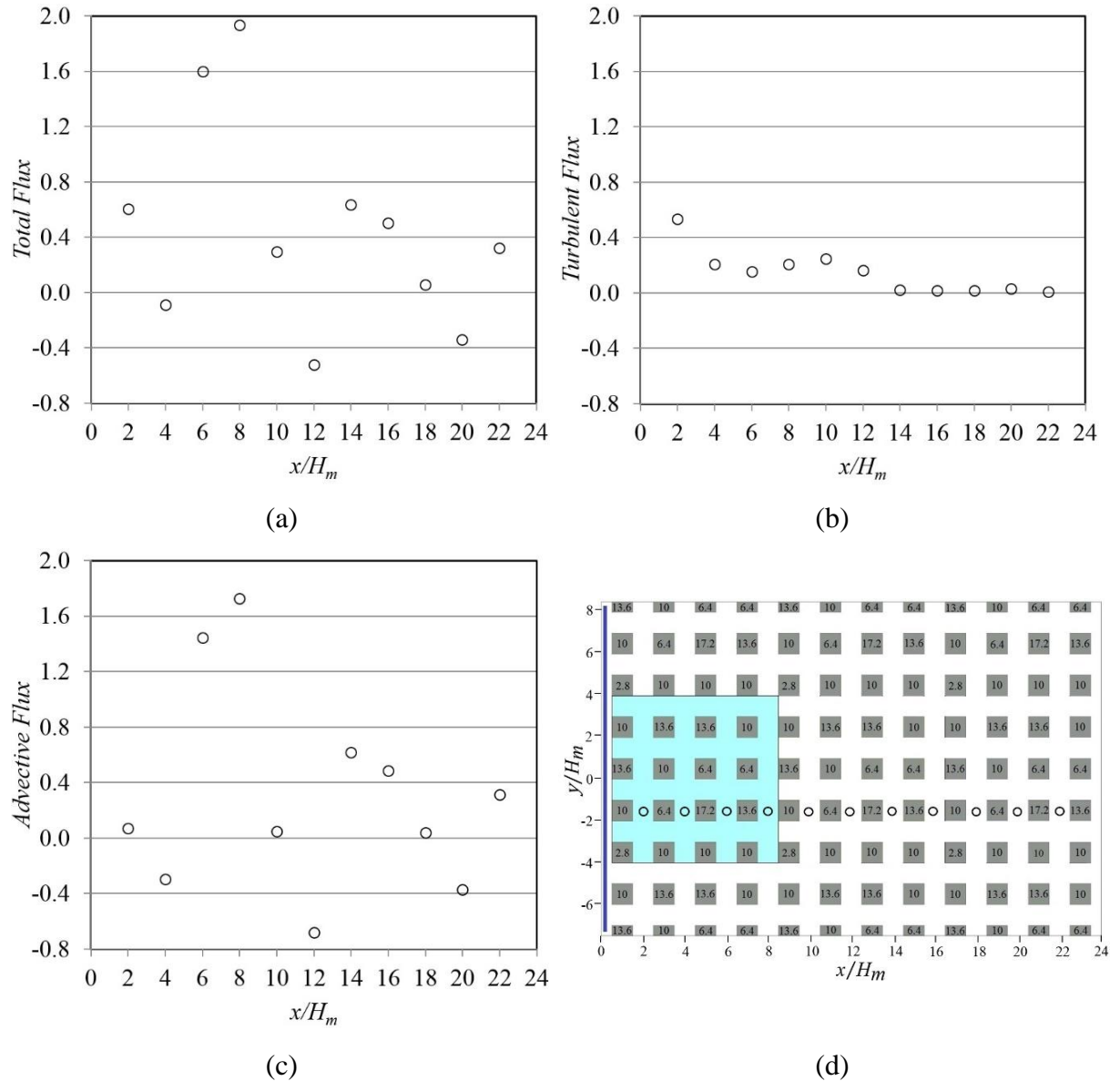


Figure 38. Quantities of normalised (a) total, (b) turbulent and (c) advective vertical fluxes for RBA configuration. (d) Schematic representation and sampled locations. Symbols indicate the locations between buildings (\circ)

Figure 39 demonstrates the pattern along the main street at $y/H_m = -0.5$ for the RBA configuration. The turbulent vertical scalar flux dominates over the advective component and the total pollutant mass flux is usually positive trough all measured extension (Figure 39). Nonetheless, Figure 39b indicates that the turbulent motions are weakened with distance from the source prevailing the advective part. Regarding the advective flux, behind the tallest

buildings is observed negative values ($x/H_m = 4.0$ and 5.0 , $x/H_m = 12.0$ and 13.0), indicating that the strong downwind motions in front of such building extends through its lateral sides. The pattern at other “channelled” streets is similar, although differences are found due to different disposition of the buildings.

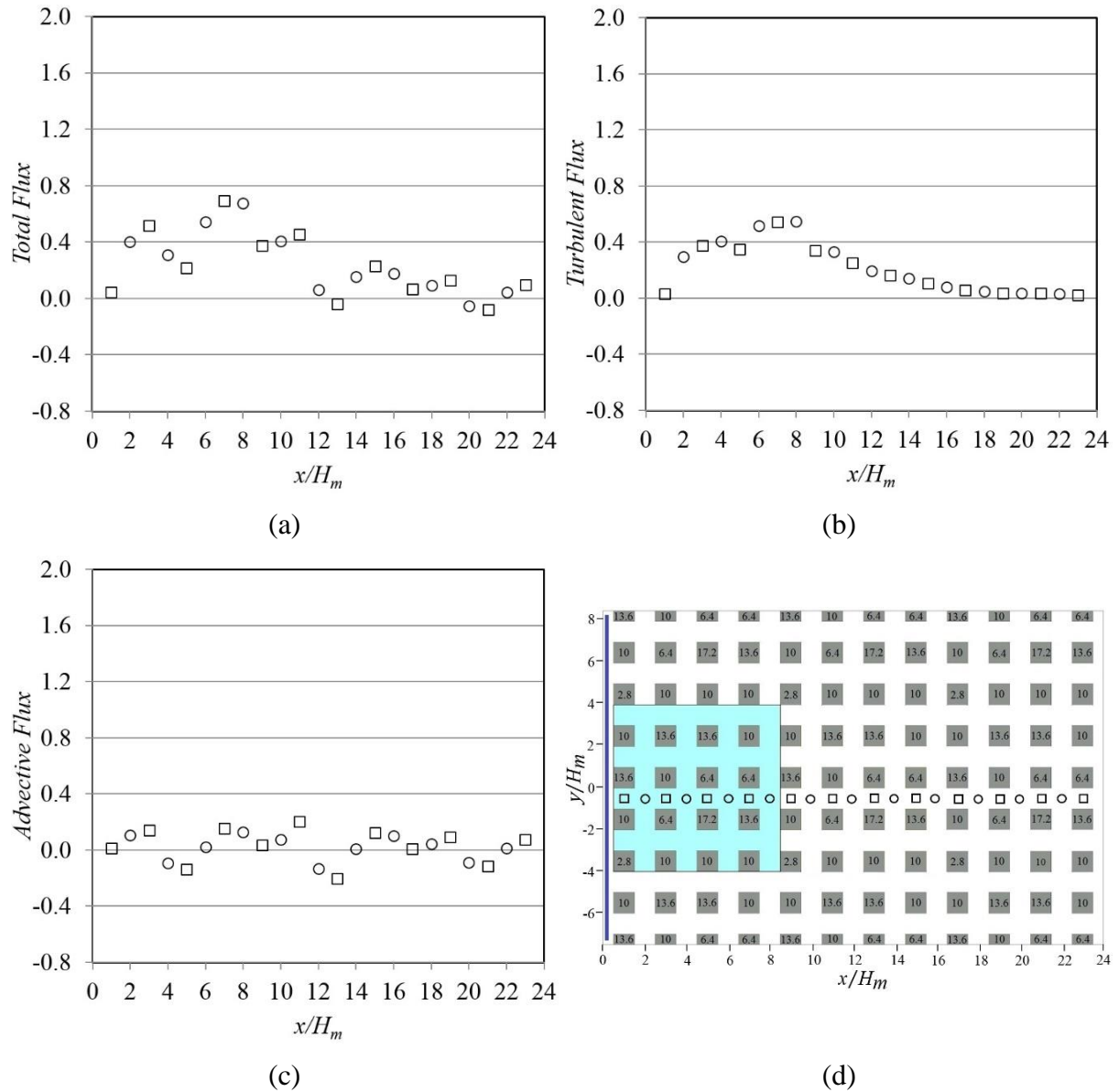


Figure 39. Quantities of normalised (a) total, (b) turbulent and (c) advective vertical fluxes with a plan view of (d) RBAA configuration. Symbols indicate the location between buildings (\circ) and intersections (\square).

The transport mechanisms outlined in the previous analyses illustrate the effects of the building height variation upon the vertical pollutant fluxes around the buildings. These patterns, due building height differences, demonstrate the local effect of the geometry in the flow field and turbulence, but there is also a non-local effect due to the fact that the fluid flow disturbances are advected downstream by the fluid flow, as show in Figure 26.

Figure 40 shows non-dimensional vertical scalar fluxes (total, advective and turbulent) normalised by the scalar flux at the area source on a horizontal plane located at $z/H_m = 1.0$ for all studied domains. Due to the larger concentrations close to the area source, vertical fluxes are larger in this region. It is interesting to note that all three configurations (UBSA, RBSA, and RBAA) exhibit regions with positive and negative local advective vertical scalar fluxes (Figure 40b, Figure 40e and Figure 40h).

For the UBSA configuration, the regions with positive and negative advective vertical flux are clearly marked (Figure 40b). This is due to the flow regime well establishing rise to updraft and downdraft motions. Despite the clear regions with negative advective vertical flux, it has smaller contribution to the total vertical flux at that height (Figure 40a). Figure 40c shows that the turbulent fluxes play the major role above the area source and its importance is reduced downwind.

The negative advective vertical flux becomes more important to the total vertical in the arrays with random building heights, since there are clearly marked patches of negative total vertical flux in Figure 40d and Figure 40g. For RBSA and RBAA configuration, the contribution of the advective vertical flux is due to the presence of the tall buildings (13.6mm and 17.2mm). It is clear that close to the taller buildings, the advective vertical flux is enhanced and close to short buildings, its importance is reduced.

Moreover, there is a contribution from those two mechanisms for the RBSA and RBAA configurations due to the urban arrangement and the presence of tall buildings. Similarly to the UBSA configuration, the turbulent fluxes are important above the area source and reduces its importance further away (Figure 40f and Figure 40i). Therefore, the advective vertical flux presents the largest value in the RBSA configuration.

Although there are patches of locally negative and positive fluxes, it is helpful to investigate the average effect of the urban configuration upon the fluxes in the regions downwind of the source. In this sense, to investigate the effect that an emission in one urban zone would promote in a more distant clean zone (i.e. an urban area without any pollutant emission), the simulation domain was divided into three repeating units, as demonstrated in Figure 41 for RBSA configuration. The regions are in the same positions for UBSA and RBSA configurations.

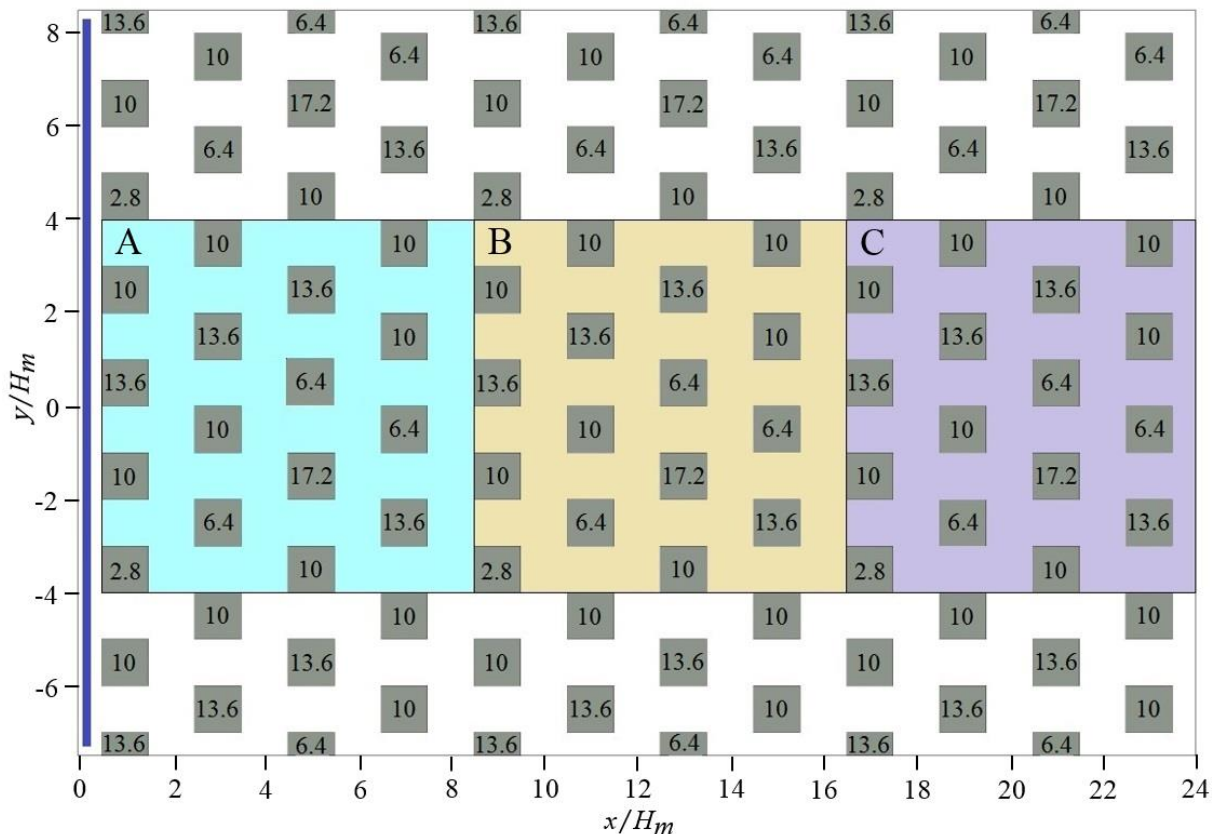


Figure 41. Plan view of the regions marked with the capital letters A, B and C denoting repeating units comprising sixteen blocks ($8H_m \times 8H_m$), where the light blue zone coincides with the area source, for RBSA

Figure 42 presents the spatially averaged vertical profiles of total, advective and turbulent non-dimensional scalar fluxes that were calculated for the three different urban configurations. Vertical scalar fluxes were spatially averaged over each urban zone every $z = 0.2H_m$ from the ground up to $z = 4H_m$ in order to produce a vertical profile.

As a general pattern, the total vertical scalar flux decreases with height above a certain height, which is different depending on the urban zone (A, B or C) and the urban configuration. In zones B and C, the advective fluxes are very small (near to zero) compared to the turbulent fluxes at all heights for all configurations, being a little more important for the aligned configuration. The total flux decreases with height in zone A for all configurations. On the other

hand, the partition between turbulent and advective vertical scalar flux is not similar for all configurations.

The advective vertical scalar flux in urban zone A within the canopy is smaller than the turbulent flux for the RBAA configuration as the unobstructed streets lead to a smaller magnitude of the vertical velocity component. It is important to remember that the tallest building for the random building configurations is $z = 1.72H_m$ and $z = 1.0H_m$ for the uniform building configuration. The advective scalar flux vanishes at a little above $z = 1.0H_m$ for all configurations. Above this height, the vertical scalar flux is dominated by turbulence. For urban zones B and C, the advective flux is negligible with values close to zero along the vertical direction.

In urban zone A, the turbulent vertical scalar flux decreases rapidly with height until about $0.25H_m$ for all configurations (Figure 42a, Figure 42d and Figure 42g). For the RBAA configuration (Figure 42g), it continues to decrease but more slowly, reaching a minimum at $2.5H_m$. The flow field is more structured with less blocking and, therefore, there is less turbulence and the turbulent scalar flux is smaller compared with the staggered configurations. Shen et al. (2017) studied the dispersion of a ground point source over a square array of cubical obstacles. They observed a similar pattern for the fluxes with height for an aligned array of uniform buildings. However, the advective flux dominates the turbulent flux within the urban canopy, while the contrary occurs in RBAA configuration.

For the UBSA configuration (Figure 42a), the turbulent vertical scalar flux continues to decrease until $0.25H_m$ then increases up to $1.0H_m$ before following the trend of dropping to a minimum close to $3.0H_m$. For the RBSA configuration (Figure 42d), the turbulent vertical scalar flux also decreases until $0.25H_m$ and then it is constant with height up to $1.0H_m$, subsequently decreasing slowly with height, reaching a minimum at $3.0H_m$.

For urban zones B (Figure 42b, Figure 42e and Figure 42h) and C (Figure 42c, Figure 42f and Figure 42i), in all configurations, the turbulent flux dominates over the advective flux with the advective scalar flux close to zero. Within the canopy, the total vertical scalar flux increases with height for all simulations. For the staggered cases, it increases linearly (Figure 42b and Figure 42e) and for the aligned case (Figure 42h) the vertical profile increases quickly with height. However, for all simulations, the peak of the vertical scalar flux is above the average building height. Increasing the distance from the source, the total vertical scalar flux is reduced and the maximum value is shifted upwards. Although the local advective vertical scalar flux is

important near the vicinity of the tall buildings, the spatially averaged vertical scalar flux indicates that the turbulent flux is dominant. The local advective vertical scalar flux close to tall buildings is important in setting the local concentration.

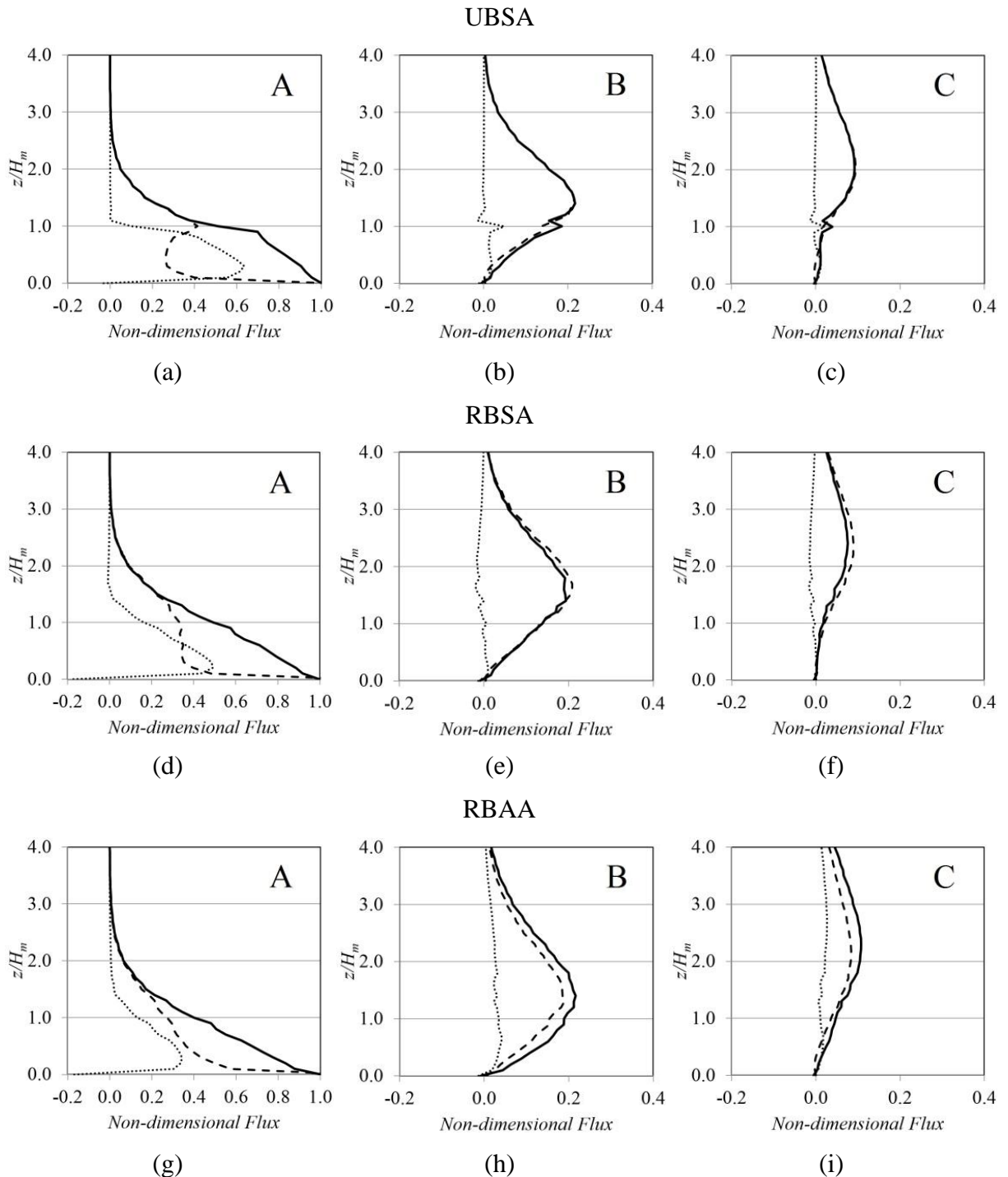


Figure 42. Spatially averaged vertical profiles of non-dimensional vertical scalar flux for the UBSA (a, b, c), RSAA (d, e, f), and RBAA (g, h, i) configurations. Solid lines represent the total scalar flux, broken lines represent the turbulent scalar flux and dotted lines represent the advective scalar flux. Capital letters indicate the urban zones

It is important to note that the majority of street network dispersion models use the spatially averaged turbulent vertical scalar flux to parameterize the transfer velocity Hertwig et al. (2018). However, this study suggests that it is inconsistent to estimate the transfer velocity assuming that the advective flux is negligible in the case of non-uniform building heights and non-aligned arrays.

In addition, total flux for RBAA is determined by the height of the upwind building, so the presence of a taller building provides positive total flux. Therefore, the turbulent and advective vertical fluxes are very important inside the canopy over the area source. However, as the distance from the source increases the turbulent vertical flux dominates and is stronger above the canopy. This means that pollutants emitted in the area source are transported vertically by advection inside the canopy over the area source but are more strongly influenced by the turbulent flux above the canopy further from the source. Compared to the staggered configurations, it can also be seen that the vertical fluxes remain important inside the canopy for longer distances from the source for the RBAA due to the flow channeling effect.

In order to better understand the contribution of different building heights on the on streamwise direction, the spatial average of the horizontal scalar fluxes were also calculated for all simulations as

$$\underbrace{\langle c \bar{u} \rangle}_{\text{Total flux}} = \underbrace{\langle \bar{c} \rangle \langle \bar{u} \rangle}_{\text{Advective flux}} + \underbrace{\langle c' u' \rangle}_{\text{Turbulent flux}}$$

where $\langle \rangle$ denotes spatial averaging, $\bar{\quad}$ represents the time average, c is the concentration, u is the streamwise velocity component (in the x -axis direction) and u' is the vertical velocity fluctuation.

Spatially averaged horizontal total, advective and turbulent scalar fluxes (normalised by the scalar flux at the area source) are presented in Figure 43 for the three urban zones in all configurations (Figure 41). Horizontal scalar fluxes were spatially averaged at the outlet of the urban zones over a line at every $0.2H_m$ from the ground until $4.0H_m$ to produce a vertical profile.

While advective fluxes are the dominant mechanism responsible for horizontal transport, vertical transport results from a complex interaction between turbulent and advective fluxes, especially for the configuration with random building heights. Over the area source (zone A), for the staggered configurations (Figure 43a and Figure 43d) there is an increase of the horizontal scalar flux with height because there is less obstruction to the flow. It reaches its

peak at the canopy top and after that, the horizontal scalar flux decreases with height. In contrast, for the aligned configuration (Figure 43g), there is a decrease in the horizontal scalar flux with height, since there is less channeling of the flow with height. Note that the turbulent horizontal scalar flux is negative for the three cases in the three urban zones.

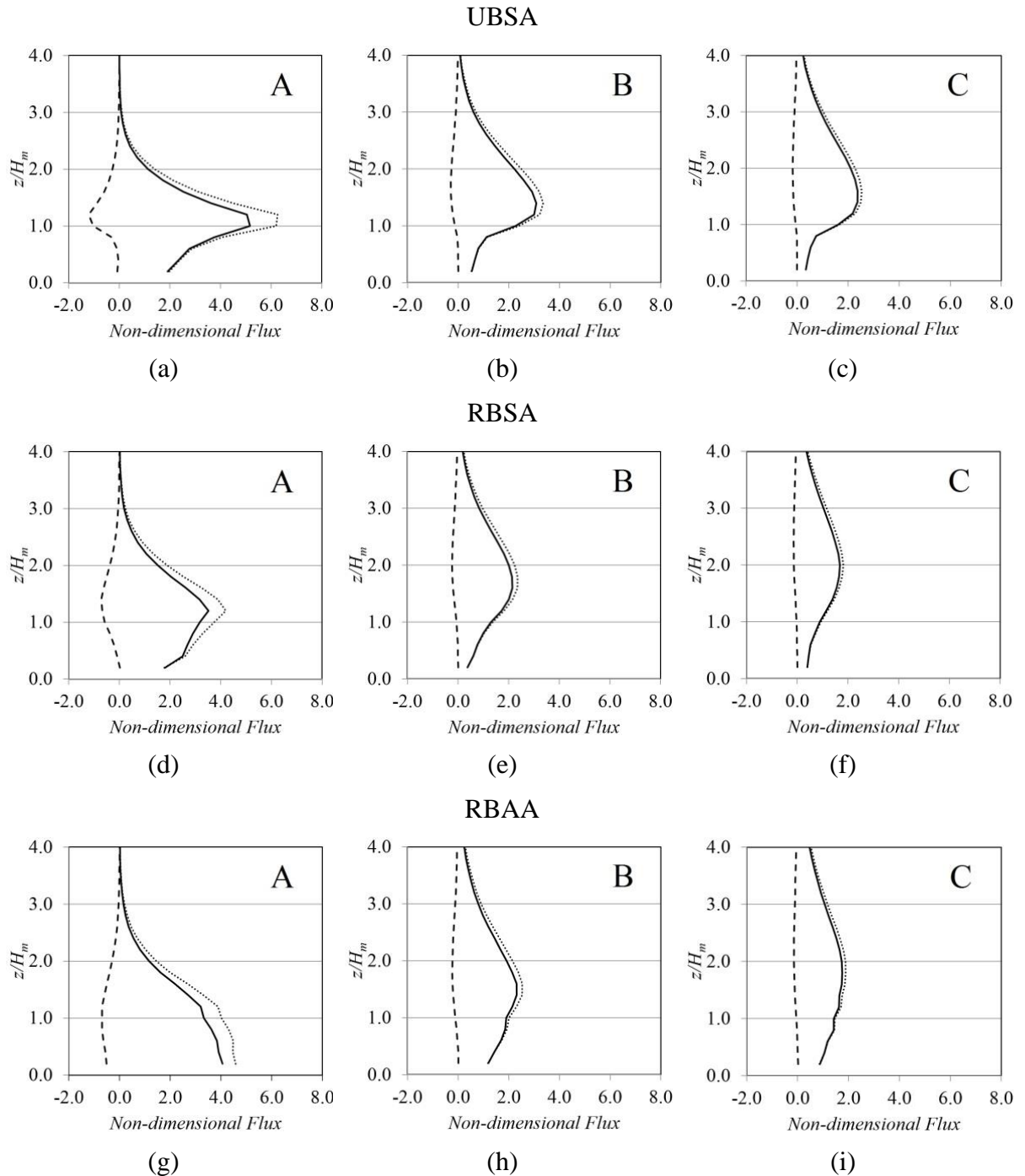


Figure 43. Spatially averaged vertical profile of horizontal scalar flux for UBSA (a, b, c) RBSA (d, e, f) and for RBAA (g, h, i) configurations. Solid lines represent the total scalar flux, broken lines represent the turbulent scalar flux and dotted lines represent the advective scalar flux. Capital letters indicate the urban zones

Figure 44 presents the ratio between vertical and averaged horizontal fluxes leaving zone A. The horizontal fluxes were averaged for two different vertical planes: from the ground to $z/H_m = 1.00$ and to $z/H_m = 1.72$. As discussed previously, the proportion between horizontal fluxes inside the canopy and the vertical flux to the atmosphere above is very important in setting the pollutant concentration in downwind areas, since it will indicate the ratio between the amounts of pollutant transported from the canopy to the atmosphere above and the amount of pollutant transported to the region downwind.

In general, the staggered configurations (RBSA and UBSA) yield a larger ratio between vertical and horizontal fluxes for $z/H_m = 1.0$, which indicates that these configurations have stronger vertical pollutant mass transfers than the aligned configuration. This trend is probably related to the channeling effect caused by the aligned streets in the RBAA configuration to the channeling of the flow.

The configuration RBSA displays a ratio between vertical and horizontal fluxes larger than unity, which indicates that there is more pollutant mass leaving the canopy to the upper atmosphere than mass being transferred further downwind. The configuration UBSA also presents a ratio close to unity, but the value is more than 20% smaller than the value obtained for the RBSA configuration, which may indicate that random building heights play an important role in the process. For $z/H_m = 1.72$, a significant part of the scalar mass is still being transported upwards to the atmosphere in the cases with random building heights

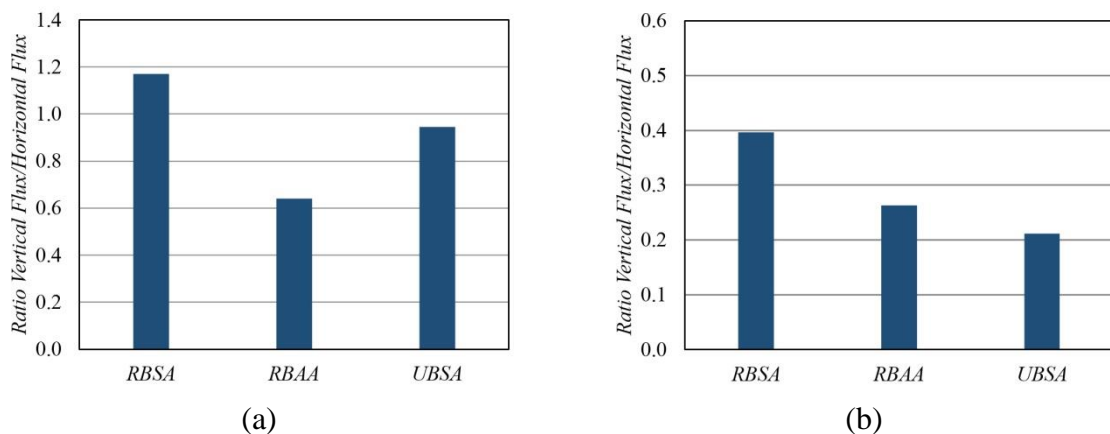


Figure 44. Ratio between vertical and averaged horizontal fluxes leaving zone A, for (a) $z/H_m = 0.0$ to $z/H_m = 1.0$ and (b) $z/H_m = 1.0$ to $z/H_m = 1.72$

5 CONCLUSIONS

This work focused on the large-eddy simulation of the wind flow and pollutant dispersion over three different urban-like configurations, in which the pollutant is emitted by an area source on the ground. The first configuration is a staggered array of random building heights – RBSA, the second is a staggered array of uniform building height – UBSA and the last is an aligned array with random height buildings – RBAA.

The comparison of the results obtained with previous studies that used wind tunnel experiments indicates reasonable agreement with experimental measurements for staggered arrays. The vertical concentration profiles suggest more efficient vertical dispersion within the random array since it provides smaller concentrations near the ground and smoother gradient compared to the uniform array. The lateral concentration profiles demonstrated what resemble a double-peak Gaussian profile near the area source and smaller concentrations for RBSA configuration throughout the domain.

In general, the results obtained in this work demonstrate that the flow within the canopy generated by the random height configuration is significantly more complex than the array with regular buildings. Despite the fact that the studied geometries do not represent real urban situation, some relevant aspects of the flow can be helpfully applied for further investigation of real sites. For example, tall buildings clearly enhance the mean vertical velocities, generating stronger downdraft in front of them and, consequently, transport efficiently the air in that region. The results suggest that the effects related to the vertical velocity fluctuations and, consequently, the turbulent motions are more largely spread downwind above smaller buildings. Instantaneous velocity vectors illustrate updrafts and downdrafts between buildings. These vertical turbulent motions are responsible for the vertical turbulent flux of pollutants leaving/entering the urban canopy. It seems that random height buildings enhance turbulence

intensity and therefore, the turbulent fluxes. The intensity of the effects of the turbulent structures seems to be related to the buildings height variation. The higher the building height, the greater is the layer in which the flow has larger vertical velocity fluctuations.

Regarding the dispersion field, both random building arrays generated similar time-averaged concentration pattern within the canopy, presenting high concentration zones in the wake region and low concentration zones in front of the buildings. The aligned array promotes a lower amount of pollutant within the channels, however great recirculation due the *skimming flow* pattern promotes high concentration zones, especially in the gap between two tall buildings.

In addition, the results demonstrate that the advective vertical scalar flux plays an important role in the local transport of pollutants from/to the array, to an extent that varies according to building height differences and arrangements. In fact, for staggered array cases the advective vertical scalar flux has the same magnitude as the turbulent vertical scalar flux even in the case of uniform building heights. Moreover, the advective vertical scalar flux is negative in some locations depending on the building or upwind buildings height increasing the concentration, while the turbulent vertical scalar flux is always positive at all locations, reducing the concentration within the canopy.

In general, the staggered configurations (RBSA and UBSA) provide a larger ratio between vertical and horizontal fluxes at $z/H_m = 1.0$, which indicates that these configurations yield stronger vertical pollutant mass transfer than the aligned configuration. This trend is probably related to the channeling effect caused by the aligned streets in the RBAA configuration. For non-uniform heights arrays, there are intense down and up drafts in front of and behind the tall buildings. It is important to highlight that although the local advective vertical scalar flux is important in the vicinity of the buildings, the spatially averaged vertical scalar flux indicates that the turbulent flux is dominant when a larger area is considered. Nonetheless, the local advective vertical scalar flux close to tall buildings remains important in determining the local concentration.

Finally, the height variability should be considered as an important parameter regarding pollutant dispersion in urban environments. The influence of both advection and turbulent contributions should be acknowledged. This fact may prove to be a challenge for the existing street network dispersion models, for example, since most of these models consider only the turbulent vertical flux. Therefore, this topic becomes a relevant and a needed to be treated in further research investigations.

5.1 FUTURE WORK RECOMMENDATION

Important insights were gained in the understanding the effects of building height variability upon the pollutant mass transport mechanisms in urban canopies. However, the literature review and the results presented in this dissertation provide some proposals for further investigation, outlined below.

- *Detailed investigation on the influence of building height variability on the dispersion field:* In this work, a large area source was considered covering the ground surface around several buildings. Therefore, the influence of different building height on the dispersion field could not be precisely determined. Numerical simulations of the dispersion of different point sources localised at different locations around the buildings with distinct heights may improve the understanding in this topic.
- *Investigation on the influence of different atmospheric stability conditions on the dispersion field:* It is known that the atmosphere rarely presents neutral stability conditions. So, numerical simulations taking into account unstable and stable conditions are proposed for further investigation.
- *Study of dispersion behavior using different Schmidt number:* In this work, the Schmidt number was calculated based on the substance (naphthalene, in case) released in the wind tunnel experiment. This number is based on the diffusivity of this specific material. So, further studies on the effects of different substances (and consequently different Schmidt number), should be conducted to compare the dispersion patterns with the present work.

REFERENCES

AI, Z. T.; MAK, C. M. Large-eddy Simulation of flow and dispersion around an isolated building: Analysis of influencing factors. **Computers and Fluids**, v. 118, p. 89–100, 2015.

AI, Z. T.; MAK, C. M. CFD simulation of flow in a long street canyon under a perpendicular wind direction: Evaluation of three computational settings. **Building and Environment**, v. 114, p. 293–306, 2017.

ANSYS. **ANSYS FLUENT Theory Guide**. USA: Ansys Inc., 2011.

ARISTODEMOU, E. et al. How tall buildings affect turbulent air flows and dispersion of pollution within a neighbourhood. **Environmental Pollution**, v. 233, p. 782–796, 2018.

BELCHER, S. E. Mixing and transport in urban areas. **Philosophical Transactions of the Royal Society A: Mathematical, Physical and Engineering Sciences**, v. 363, n. 1837, p. 2947–2968, 2005.

BLOCKEN, B. et al. Application of computational fluid dynamics in building performance simulation for the outdoor environment: an overview. **Journal of Building Performance Simulation**, v. 4, n. 2, p. 157–184, 2011.

BOPPANA, V. B. L.; XIE, Z. T.; CASTRO, I. P. Large-eddy simulation of dispersion from surface sources in arrays of obstacles. **Boundary-Layer Meteorology**, v. 135, n. 3, p. 433–454, 2010.

BRANFORD, S. et al. Dispersion of a Point-Source Release of a Passive Scalar Through an Urban-Like Array for Different Wind Directions. **Boundary-Layer Meteorology**, v. 139, n. 3, p. 367–394, 2011.

CAI, X. M.; BARLOW, J. F.; BELCHER, S. E. Dispersion and transfer of passive scalars in and above street canyons-Large-eddy simulations. **Atmospheric Environment**, v. 42, n. 23, p. 5885–5895, 2008.

- CARPENTIERI, M. et al. Mean and turbulent mass flux measurements in an idealised street network. **Environmental Pollution**, v. 234, p. 356–367, 2018.
- CARPENTIERI, M.; HAYDEN, P.; ROBINS, A. G. Wind tunnel measurements of pollutant turbulent fluxes in urban intersections. **Atmospheric Environment**, v. 46, p. 669–674, 2012.
- CARPENTIERI, M.; ROBINS, A. G.; BALDI, S. Three-dimensional mapping of air flow at an urban canyon intersection. **Boundary-Layer Meteorology**, v. 133, n. 2, p. 277–296, 2009.
- CASTRO, I. P. et al. Measurements and Computations of Flow in an Urban Street System. **Boundary-Layer Meteorology**, v. 162, n. 2, p. 207–230, 2017.
- CASTRO, I. P.; ROBINS, A. G. The flow around a surface-mounted cube in uniform and turbulent streams. **Journal of Fluid Mechanics**, v. 79, n. 2, p. 307–335, 1977.
- CHEN, L. et al. The impacts of building height variations and building packing densities on flow adjustment and city breathability in idealized urban models. **Building and Environment**, v. 118, p. 344–361, 2017.
- CHEN, Q.; SREBRIC, J. A procedure for verification, validation, and reporting of indoor environment CFD analyses. **HVAC and R Research**, v. 8, n. 2, p. 201–216, 2002.
- CHENG, H.; CASTRO, I. A. N. P. Near wall flow over urban-like roughness. v. 104, n. November 2001, p. 229–259, 2002a.
- CHENG, H.; CASTRO, I. P. Near wall flow over urban-like roughness. **Boundary-Layer Meteorology**, v. 104, p. 229–259, 2002b.
- CHENG, H.; CASTRO, I. P. Near-wall flow development after a step change in surface roughness. **Boundary-Layer Meteorology**, v. 105, n. August 2001, p. 411–432, 2002c.
- CHENG, W. C.; PORTÉ-AGEL, F. Large-eddy simulation of flow and scalar dispersion in rural-to-urban transition regions. **International Journal of Heat and Fluid Flow**, v. 60, p. 47–60, 2016.
- COCEAL, O. et al. Mean flow and turbulence statistics over groups of urban-like cubical obstacles. **Boundary-Layer Meteorology**, v. 121, n. 3, p. 491–519, 2006.
- COCEAL, O. et al. Structure of turbulent flow over regular arrays of cubical roughness. **Journal of Fluid Mechanics**, v. 589, p. 375–409, 2007.
- COCEAL, O. et al. Flow structure and near-field dispersion in arrays of building-like obstacles. **Journal of Wind Engineering and Industrial Aerodynamics**, v. 125, p. 52–68, 2014.

- DAVIDSON, M. J. et al. Plume dispersion through large groups of obstacles - a field investigation. **Atmospheric Environment**, v. 29, n. 22, p. 3245–3256, 1995.
- DAVIDSON, M. J. et al. Wind tunnel simulations of plume dispersion through groups of obstacles. **Atmospheric Environment**, v. 30, n. 22, p. 3715–3731, 1996.
- DEARDORFF, J. W. A numerical study of three-dimensional turbulent channel flow at large Reynolds numbers. **Journal of Fluid Mechanics**, v. 41, n. 2, p. 453–480, 1970.
- DI BERNARDINO, A. et al. Pollutant fluxes in two-dimensional street canyons. **Urban Climate**, v. 24, n. January, p. 80–93, 2018.
- FUKA, V. et al. Scalar Fluxes Near a Tall Building in an Aligned Array of Rectangular Buildings. **Boundary-Layer Meteorology**, v. 167, n. 1, p. 53–76, 2018.
- GARBERO, V.; SALIZZONI, P.; SOULHAC, L. Experimental Study of Pollutant Dispersion Within a Network of Streets. **Boundary-Layer Meteorology**, v. 136, n. 3, p. 457–487, 2010.
- GOULART, E. V. et al. Spatial and Temporal Variability of the Concentration Field from Localized Releases in a Regular Building Array. **Boundary-Layer Meteorology**, v. 159, n. 2, p. 241–257, 2016.
- GOULART, E. V.; COCEAL, O.; BELCHER, S. E. Dispersion of a Passive Scalar Within and Above an Urban Street Network. **Boundary-Layer Meteorology**, v. 166, n. 3, p. 351–366, 2018.
- HERTWIG, D. et al. Evaluation of fast atmospheric dispersion models in a regular street network. **Environmental Fluid Mechanics**, v. 18, n. 4, p. 1007–1044, 2018.
- HUANG, J. et al. Impacts of air pollution wave on years of life lost: A crucial way to communicate the health risks of air pollution to the public. **Environment International**, v. 113, n. November 2017, p. 42–49, 2018.
- KAMPA, M.; CASTANAS, E. Human health effects of air pollution. **Environmental Pollution**, v. 151, p. 362–367, 2007.
- KUBILAY, A. et al. The pollutant removal capacity of urban street canyons as quantified by the pollutant exchange velocity. **Urban Climate**, v. 21, p. 136–153, 2017.
- LATEB, M. et al. On the use of numerical modelling for near-field pollutant dispersion in urban environments - A review. **Environmental Pollution**, v. 208, p. 271–283, 2016.
- LEONARD, A. Turbulent Diffusion in Environmental Pollution, Proceedings of a Symposium

held at Charlottesville. **Advances in Geophysics**, v. 18, p. 237–248, 1975.

LI, X. X. et al. Recent progress in CFD modelling of wind field and pollutant transport in street canyons. **Atmospheric Environment**, v. 40, n. 29, p. 5640–5658, 2006.

LILLY, D. K. On the application of the eddy viscosity concept in the inertial sub-range of turbulence. **National Center for Atmospheric Research**, 1966.

LILLY, D. K. The representation of small-scale turbulence in numerical simulation experiments. **Proceedings of IBM Science and Computer Symposium on Environmental Science**, 1967.

LIN, M. et al. Quantitative ventilation assessments of idealized urban canopy layers with various urban layouts and the same building packing density. **Building and Environment**, v. 79, p. 152–167, 2014.

LIU, C. H.; LEUNG, D. Y. C.; BARTH, M. C. On the prediction of air and pollutant exchange rates in street canyons of different aspect ratios using large-eddy simulation. **Atmospheric Environment**, v. 39, n. 9, p. 1567–1574, 2005.

MACDONALD, R. W.; GRIFFITHS, R. F.; HALL, D. J. An improved method for the estimation of surface roughness of obstacle arrays. **Atmospheric Environment**, v. 32, n. 11, p. 1857–1864, 1998.

MAVROIDIS, I.; GRIFFITHS, R. F.; HALL, D. J. Field and wind tunnel investigations of plume dispersion around single surface obstacles. **Atmospheric Environment**, v. 37, n. 21, p. 2903–2918, 2003.

MEI, S. J. et al. Wind driven natural ventilation in the idealized building block arrays with multiple urban morphologies and unique package building density. **Energy and Buildings**, v. 155, p. 324–338, 2017.

MICHIOKA, T.; TAKIMOTO, H.; SATO, A. Large-Eddy Simulation of Pollutant Removal from a Three-Dimensional Street Canyon. **Boundary-Layer Meteorology**, v. 150, n. 2, p. 259–275, 2014.

MOUKALLED, F.; MANGANI, L.; DARWISH, M. **The Finite Volume Method in Computational Fluid Dynamics**. [s.l: s.n.]. v. 113

MURAKAMI, S. Comparison of Various Turbulence Models. **Journal of Wind Engineering and Industrial Aerodynamics**, v. 47, p. 21–36, 1993.

NAKAYAMA, H.; TAKEMI, T.; NAGAI, H. LES analysis of the aerodynamic surface properties for turbulent flows over building arrays with various geometries. **Journal of Applied Meteorology and Climatology**, v. 50, n. 8, p. 1692–1712, 2011.

NEOPHYTOU, M. K. A.; MARKIDES, C. N.; FOKAIDES, P. A. An experimental study of the flow through and over two dimensional rectangular roughness elements: Deductions for urban boundary layer parameterizations and exchange processes. **Physics of Fluids**, v. 26, n. 8, 2014.

NOSEK, Š. et al. Ventilation Processes in a Three-Dimensional Street Canyon. **Boundary-Layer Meteorology**, v. 159, n. 2, p. 259–284, 2016.

NOSEK, Š. et al. Impact of roof height non-uniformity on pollutant transport between a street canyon and intersections. **Environmental Pollution**, v. 227, p. 125–138, 2017.

NOSEK, Š. et al. Street-canyon pollution with respect to urban-array complexity: The role of lateral and mean pollution fluxes. **Building and Environment**, v. 138, n. April, p. 221–234, 2018.

OKE, T. R. Street design and urban canopy layer climate. **Energy and Buildings**, v. 11, n. 1–3, p. 103–113, 1988.

PASCHEKE, F.; BARLOW, J. F.; ROBINS, A. Wind-tunnel modelling of dispersion from a scalar area source in urban-like roughness. **Boundary-Layer Meteorology**, v. 126, n. 1, p. 103–124, 2008.

PHILIPS, D. A.; ROSSI, R.; IACCARINO, G. Large-eddy simulation of passive scalar dispersion in an urban-like canopy. **Journal of Fluid Mechanics**, v. 723, n. 2013, p. 404–428, 2013.

POPE, S. B. **Turbulent Flows**. Cambridge, UK: Cambridge University Press, 2000.

REYNOLDS, O. On the dynamical theory of incompressible viscous fluids and the determination of the criterion. **Philosophical Transactions of the Royal Society A**, v. 186, p. 123–164, 1985.

ROBINS, A. G.; CASTRO, I. P. A wind tunnel investigation of plume dispersion in the vicinity of a surface mounted Cube-I. The flow field. **Atmospheric Environment (1967)**, v. 11, n. 4, p. 291–297, 1977a.

ROBINS, A. G.; CASTRO, I. P. A wind tunnel investigation of plume dispersion in the vicinity

of a surface mounted cube 2 - The concentratio filed. **Atmospheric Environment**, v. 11, p. 299–311, 1977b.

ROGALLO, R. S.; MOIN, P. Numerical simulation of turbulent flows. **Annual Review of Fluid Mechanics**, v. 16, n. 1, p. 99–137, 1984.

SAGAUT, P. **Large Eddy Simulation for Incompressible Flows An Introduction**. 3. ed. Berlin Heidelberg: Springer, 2006.

SALIZZONI, P.; SOULHAC, L.; MEJEAN, P. Street canyon ventilation and atmospheric turbulence. **Atmospheric Environment**, v. 43, n. 32, p. 5056–5067, 2009.

SANCHEZ, B. et al. Modelling NOX concentrations through CFD-RANS in an urban hot-spot using high resolution traffic emissions and meteorology from a mesoscale model. **Atmospheric Environment**, v. 163, n. X, p. 155–165, 2017.

SANTIAGO, J. L. et al. Evaluation of a CFD-based approach to estimate pollutant distribution within a real urban canopy by means of passive samplers. **Science of the Total Environment**, v. 576, p. 46–58, 2017.

SANTOS, J. M. et al. Numerical simulation of flow and dispersion around an isolated cubical building: The effect of the atmospheric stratification. **Atmospheric Environment**, v. 43, n. 34, p. 5484–5492, 2009.

SHEN, J. et al. An investigation on the effect of street morphology to ambient air quality using six real-world cases. **Atmospheric Environment**, v. 164, p. 85–101, 2017.

SHEN, Z.; CUI, G.; ZHANG, Z. Turbulent dispersion of pollutants in urban-type canopies under stable stratification conditions. **Atmospheric Environment**, v. 156, p. 1–14, 2017.

SMAGORINSKY, J. General circulation experiments with the primitive equations. Part I: The basic experiment. **Monthly Weather Review**, v. 91, n. 3, p. 99–164, 1963.

TOMINAGA, Y.; STATHOPOULOS, T. Numerical simulation of dispersion around an isolated cubic building: Model evaluation of RANS and LES. **Building and Environment**, v. 45, n. 10, p. 2231–2239, 2010.

TOMINAGA, Y.; STATHOPOULOS, T. CFD simulation of near-field pollutant dispersion in the urban environment: A review of current modeling techniques. **Atmospheric Environment**, v. 79, p. 716–730, 2013.

TOPARLAR, Y. et al. A review on the CFD analysis of urban microclimate. **Renewable and**

Sustainable Energy Reviews, v. 80, p. 1613–1640, 2017.

VARDOULAKIS, S. et al. Modelling air quality in street canyons: A review. **Atmospheric Environment**, v. 37, n. 2, p. 155–182, 2003.

VARDOULAKIS, S. et al. Numerical Model Inter-comparison for Wind Flow and Turbulence Around Single-Block Buildings. **Environmental Modeling and Assessment**, v. 16, n. 2, p. 169–181, 2011.

VERSTEEG, H. K. .; MALALASEKERA, W. . **An Introduction to Computational Fluid Dynamics**. [s.l: s.n.]. v. M

XIE, Z.; CASTRO, I. P. LES and RANS for turbulent flow over arrays of wall-mounted obstacles. **Flow, Turbulence and Combustion**, v. 76, n. 3, p. 291–312, 2006.

XIE, Z. T.; COCEAL, O.; CASTRO, I. P. Large-Eddy simulation of flows over random urban-like obstacles. **Boundary-Layer Meteorology**, v. 129, n. 1, p. 1–23, 2008.

YOSHIDA, T.; TAKEMI, T.; HORIGUCHI, M. Large-Eddy-Simulation Study of the Effects of Building-Height Variability on Turbulent Flows over an Actual Urban Area. **Boundary-Layer Meteorology**, v. 168, n. 1, p. 127–153, 2018.

YUAN, C.; NG, E.; NORFORD, L. K. Improving air quality in high-density cities by understanding the relationship between air pollutant dispersion and urban morphologies. **Building and Environment**, v. 71, n. 2, p. 245–258, 2014.

ZAKI, S. A. et al. Aerodynamic Parameters of Urban Building Arrays with Random Geometries. **Boundary-Layer Meteorology**, v. 138, n. 1, p. 99–120, 2011.

ZHIYIN, Y. Large-eddy simulation: Past, present and the future. **Chinese Journal of Aeronautics**, v. 28, n. 1, p. 11–24, 2015.